Optics Design of a novel Beam Delivery System for CLIC : the case of two Interaction Regions. First experiments for the validation of the ultra-low betay* nanometer beam size at ATF2

Vera Cilento

Thèse de doctorat

NNT: 2021UPASP115

université PARIS-SACLAY

Optics Design of a novel Beam Delivery System for CLIC: the case of two Interaction Regions. First experiments for the validation of the ultra-low β_y^* nanometer beam size at ATF2.

Conception optique d'un nouveau système de distribution de faisceau pour CLIC: le cas de deux régions d'interaction. Premières expériences pour la validation de la taille de faisceau ultra-faible β_y^* nanométrique à ATF2.

Thèse de doctorat de l'Université Paris-Saclay

École doctorale n° 576, Particules hadrons énergie et noyau: instrumentation, image, cosmos et simulation (PHENIICS)
Spécialité de doctorat: Physique des accélérateurs
Unité de recherche: Université Paris-Saclay, CNRS, IJCLab, 91405, Orsay, France.
Référent: Faculté des sciences d'Orsay.

Thèse présentée et soutenue à Paris-Saclay, le 15 novembre 2021, par

Vera CILENTO

Composition du jury:

Philip BURROWS Professeur, Oxford University	Président
Karsten BUESSER Ingénieur de recherche, Deutsches Elektronen-Synchrotron	Rapporteur & Examinateur
Steinar STAPNES Professeur, University of Oslo	Rapporteur & Examinateur
Sebastien BOUSSON Ingénieur de recherche, Université Paris-Saclay	Examinateur
Benito GIMENO Professeur, University of Valencia	Examinateur
Shigeru KURODA Professeur, Sokendai University	Examinateur

Direction de la thèse:

Angeles FAUS-GOLFE Ingénieure de recherche, Université Paris-Saclay	Directrice de thèse
Rogelio TOMAS-GARCIA Ingénieure de recherche, Conseil Européen pour la Recherche Nucléaire	Co-encadrant de thèse

université PARIS-SACLAY

ÉCOLE DOCTORALE
Particules, hadrons, énergie et noyau : instrumentation, imagerie, cosmos et simulation (PHENIICS)

Titre: Conception optique d'un nouveau système de distribution de faisceau pour CLIC: le cas de deux régions d'interaction. Premières expériences pour la validation de la taille de faisceau ultra-faible β_y^* nanométrique à ATF2.

Mots clés: Collisionneurs linéaires, Collisionneur Linéaire Compact (CLIC), dynamique des faisceaux, système de focalisation finale, luminosité

Résumé: Le collisionneur linéaire compact (CLIC) pourrait produire des collisions e^+e^- dans deux détecteurs simultanément, éventuellement à une fréquence de train de paquets dans le LINAC deux fois supérieure à la valeur nominale de référence. Dans ce manuscrit, une nouvelle conception de système de diffusion à double faisceau (BDS) est présentée afin de desservir deux régions d'interaction (IR1 et IR2), incluant des conceptions optiques et l'évaluation des performances de luminosité avec le rayonnement synchrotron (SR) et les effets de solénoïde pour les deux étages d'énergie de CLIC à 380 GeV et 3 TeV. IR2 présente un angle de croisement plus grand que la ligne de base actuelle. Les performances de luminosité du nouveau schéma de CLIC ont été évaluées en comparant les différentes conceptions de BDS avec et sans les effets de champ du solénoïde du détecteur. Il faut souligner que l'impact du solénoïde du détecteur sur la luminosité n'avait pas été évalué pour la ligne de base de CLIC actuelle, ce qui équivaut à une perte d'environ 4% équivalent à la même valeur de l'ancienne conception de la ligne de base. À 380 GeV, les 2 IR de la nouvelle conception à double BDS présentent les mêmes luminosités que la ligne de base actuelle. Cependant, à 3 TeV, les performances de luminosité sont réduites de 2% par rapport à la conception de base pour l'IR1 et de 33% pour l'IR2. La conception double CLIC BDS fournit des luminosités adéquates aux deux détecteurs. Elle s'avère être un candidat viable pour les futurs projets de collisionneur linéaire. L'une des principales demandes des futurs collisionneurs linéaires est d'atteindre une taille de faisceau vertical nanométrique au point d'interaction (IP).

L'Accelerator Test Facility 2 (ATF2) est un développement à échelle réduite du système de mise au point final (FFS) pour tester le nouveau schéma de correction de la chromaticité locale requis pour les conceptions du collisionneur linéaire international (ILC) et du collisionneur linéaire compact (CLIC). Après plusieurs années d'exploitation, la mesure de $\sigma_y^* = 41 \pm 3$ nm a été effectué à ATF2 avec l'optique nominale β_y^* en 2016. Ce travail de thèse présente l'étude expérimentale des réglages réalisée avec l'ultra –low β_y^* pendant l'opération en mars 2019. Cette optique dispose d'un niveau de chromaticité comparable à celle de CLIC et nous nous attendons à ce σ_y^* soit inférieur à 40 nm.

université PARIS-SACLAY

ÉCOLE DOCTORALE
Particules, hadrons, énergie et noyau : instrumentation, imagerie, cosmos et simulation (PHENIICS)

Title: Optics Design of a novel Beam Delivery System for CLIC: the case of two Interaction Regions. First experiments for the validation of the ultra-low β_y^* nanometer beam size at ATF2.

Keywords: Linear Collider, The Compact Linear Collider (CLIC), Beam Dynamics, Beam Optics, Luminosity

Abstract: The Compact Linear Collider (CLIC) could provide e^+e^- collisions in two detectors simultaneously at a bunch train frequency in the linac twice the baseline design value. In this thesis, a novel dual Beam Delivery System (BDS) design is presented in order to serve two Interaction Regions (IR1 and IR2) including optics designs and the evaluation of luminosity performance with synchrotron radiation (SR) and solenoid effects for both energy stages of CLIC, 380 GeV and 3 TeV. IR2 features a larger crossing angle than the current baseline. The luminosity performance of the novel CLIC scheme was evaluated by comparing the different BDS designs with and without the detector solenoid field effects. It has to be highlighted that the impact of the detector solenoid on luminosity had not been evaluated for the current CLIC baseline, which amounts to a loss of about 4% that corresponds to the same value of the old baseline design. At 380 GeV the 2 IRs of the novel dual BDS design feature same luminosities than the current baseline. However at 3 TeV the luminosity performance is reduced by 2% from the baseline design for the IR1 and by 33% for the IR2. The dual CLIC BDS design provides adequate luminosities to two detectors and proves to be a viable candidate for future linear collider projects.

One of the main requests for future linear colliders is to achieve a nanometer vertical beam size at the Interaction Point (IP). Accelerator Test Facility 2 (ATF2) represents a scale down implementation of the Final Focus System (FFS) to test the novel local chromaticity correction scheme that is implemented in the International Linear Collider (ILC) and the Compact Linear Collider (CLIC) designs. After several years of operations and commissioning, σ_y^* of 41 $\pm$ 3 nm was measured at ATF2 with the nominal β_y^* optics in 2016. This thesis reports the experimental tuning study done with the ultra-low β_y^* during March 2019 beam operation. This optics has a level of chromaticity comparable with CLIC one and it is expected to reduce σ_y^* below 40 nm.

A mio padre, sempre nel cuore...

Résumé en français

Un collisionneur linéaire à leptons (LC) est considéré comme l'un des candidats potentiels pour poursuivre les recherches en physique des particules de haute précision après la découverte du boson de Higgs au Large Hadrons Collisionneur (LHC) au CERN et les études approfondies dans son amélioration de la luminosité auprès du HL-LHC.

Deux machines ont été proposées pour le scénario de la physique d'un accélérateur de collisionneur linéaire: le collisionneur international linéaire (ILC), avec une énergie maximale comprise entre 250 GeV et 1 TeV, et le collisionneur linéaire compact (CLIC), avec des énergies jusqu'à 3 TeV. Les deux projets ont en commun la structure d'un collisionneur linéaire, qui consiste en deux longues machines linéaires accélérant les particules à une haute énergie et assurant les collisions. De plus, les systèmes très complexes des détecteurs associés à ces accélérateurs sont développés pour obtenir une très grande précision. Plus d'un millier de scientifiques à travers le monde sont impliqués dans le développement de ces nouveaux accélérateurs et détecteurs.

Le travail de cette thèse porte sur le système de distribution de faisceau (BDS) des futurs collisionneurs linéaires, en particulier le CLIC. Le BDS a comme fonction de transporter des faisceaux de positrons et d'électrons de la sortie des LINACs jusqu'à la région d'interaction (IR) en effectuant les actions requises répondre aux objectifs de luminosité de CLIC: $1.5 \times 10^{34}\,\mathrm{cm}^{-2}\mathrm{s}^{-1}$ pour le CLIC 380 GeV et $5.9 \times 10^{34}\,\mathrm{cm}^{-2}\mathrm{s}^{-1}$ pour le CLIC 3 TeV. Le transport du faisceau et l'optique de focalisation dans ce système sont un véritable défi et entrainent de nombreuses solutions non triviales.

La conception de base actuelle de CLIC inclut un seul détecteur et un seul BDS. Les conceptions de base pour CLIC à 380 GeV et à 3 TeV ont été optimisées y compris en implantant le quadrupôle final (QD0) en dehors du détecteur. La distance entre QD0 et le point d'interaction (IP) a été augmentée à L*= 6 m. La version précédente avec L*= 4.3 m pour CLIC 380 GeV et L*= 3.5 m pour CLIC 3 TeV comporte un anti-solénoïde pour annuler le champ magnétique à l'intérieur de QD0 alors que L*= 6 m n'en comporte pas.

Les conceptions de double BDS ont déjà été effectuées en considérant pour le prochain collisionneur linéaire (NLC), pour lesquelles les performances de luminosité pour les deux détecteurs étaient dans les limites de 30% jusqu'à l'énergie de 1.3 TeV. Dans ce manuscrit, nous présentons une nouvelle conception avec un déséquilibre de la luminosité comparable allant jusqu'à une énergie de 3 TeV. L'ILC, quant à lui, a un simple IP

et deux détecteurs qui peuvent mesurer les données à différents moments en suivant une disposition en pushpull. Un plan préliminaire du double BDS a été proposé pour l'ILC également, permettant deux régions d'interactions distinctes avec des angles de croisement de respectivement 2 mrad et 20 mrad.

L'objectif de ce travail de thèse est de concevoir et d'optimiser un nouveau plan du système de double BDS, réalisable en termes de luminosité, afin d'utiliser deux détecteurs et de rendre le CLIC plus compétitif vis-à-vis des futurs projets de collisionneurs circulaires.

Les performances en termes de luminosité du nouveau schéma de CLIC ont été évaluées en comparant les différentes conceptions des BDS avec et sans les effets de champs des solénoïdes. IR2 comporte un plus grand angle de croisement que la ligne de base actuelle. Il doit être souligné que l'impact du solénoïde du détecteur sur la luminosité n'a pas été évalué pour la conception actuelle de CLIC, ce qui équivaut à une perte d'environ 4%. Cela correspond à la valeur de l'ancienne conception. A 380 GeV, la nouvelle conception du double BDS offre les mêmes luminosités qu'actuellement. Cependant, à 3 TeV, la performance au niveau de la luminosité est réduite de 2% par rapport à la conception pour IR1 et de 33% pour IR2. Le système du double BDS pour CLIC offre les luminosités adéquates pour les deux détecteurs et montre qu'il s'agit d'un candidat viable pour les projets de futurs collisionneurs linéaires.

Un autre objectif pour les futurs collisionneurs linéaires est d'atteindre des luminosités plus élevées, ce qui est l'un des ingrédients clés pour obtenir une taille nanométrique du faisceau dans le plan vertical au point de collision (IP). L'installation d'essai des accélérateurs 2 (ATF2) représente une version réduite du concept du système de mise au point finale (FFS) pour tester le nouveau schéma de correction de chromaticité local qui est utilisé dans les conceptions de CLIC et de l'ILC. Après des années de mise en service, un σ_y^* égal à 41 ± 3 nm a été mesuré avec l'optique nominale β_y^* en 2016. Afin de tester la faisabilité du schéma de correction local du FFS avec une valeur de la chromaticité environ 5 fois plus élevée, comme pour CLIC, l'étude de l'optique ultra-low β_y^* a été proposée et étudiée à ATF2, où la valeur de β_y^* est réduite à 25 μm.

Ce travail de thèse présente les premières expériences des réglages effectuées avec l'ultra-low β_y^* pendant le fonctionnement du faisceau en mars 2019. L'optique devrait permettre de réduire σ_y^* inférieur 40 nm en utilisant également la paire d'octupôles ajoutée à ATF2 en 2016.

Acknowledgements

Firstly, I would like to thank and I would like to express my special gratitude to my supervisors Dr. Angeles Faus-Golfe and Dr. Rogelio Tomás for giving me the opportunity to continue working in the accelerator physics branch and in one of the biggest laboratories for scientific research in the world, the CERN. Their unique way of supervision encouraged me to pursue my ideas, to trust my abilities and motivated me to a continuous effort to always obtain new aims on accelerator research studies.

A special acknowledgement goes to all the CLIC and ATF2 collaborators. I would especially like to thank the KEK staff for the help during the machine operation and my CERN colleagues who not only taught me a lot but also shared with me so many experiences. Thanks to Andrii, Fabien, Pierre and Renjun.

I would also like to say thank you to all my friends that were always there to support me in all my decisions. Many thanks to Maria Letizia, Laura, Emanuela and Lorenzo.

Most importantly I would like to express my deep thankfulness to my mother, my sister, my husband Francesco and all my beautiful family for their endless support, infinite encouragement and for believing in me all this time.

Contents

CHAPTER 1

Introduction to the BDS for the Future Linear Colliders

A new era of discovery in particle physics has opened in November 2009 with the start-up of the Large Hadron Collider (LHC) at CERN, the European Organization for Nuclear Research, in Geneva, Switzerland. The LHC, a circular proton-proton synchrotron, operates at the highest energies any particle accelerator has ever achieved [1]. In July 2012, scientists at the LHC announced the discovery of the Higgs boson [2, 3], the last missing elementary particle predicted by the Standard Model (SM). In October 2013, P. Higgs and F. Englert were awarded with the Nobel prize in Physics in recognition of their work on the Higgs mechanism.

The Higgs, discovered at the LHC, is a unique particle that raises profound questions about the fundamental laws of nature: the Higgs properties study is in itself a powerful experimental tool to look for answers and this could be possible with an electron-positron (e^- e^+) collider considered as Higgs factory. Furthermore, the Higgs boson pair-production study is the key to understand the fabric of the universe and this could be possible with a collider with significantly higher energies than Higgs factory. As stated in the key points of the 2020 Update of the European Strategy for Particle Physics [4]:

"An electron-positron Higgs factory is the highest-priority next collider. For the longer term, the European particle physics community has the ambition to operate a proton-proton collider at the highest achievable energy. Accomplishing these compelling goals will require innovation and cutting-edge technology: the particle physics community should ramp up its R&D effort focused on advanced accelerator technologies, in particular that for high-field superconducting magnets, including high-temperature superconductors; Europe, together with its international partners, should investigate the technical and financial feasibility of a future hadron collider at CERN with a centre-of-mass energy of at least 100 TeV and with an electron-positron Higgs and electroweak factory as a possible first stage. Such a feasibility study of the colliders and related infrastructure should be established as a global endeavour and be completed on the timescale

of the next Strategy update. The timely realisation of the electron-positron International Linear Collider (ILC) in Japan would be compatible with this strategy and, in that case, the European particle physics community would wish to collaborate".

In this context, a **Higgs factory** is planned to be the next large accelerator after LHC and after further study in its luminosity upgrade, HL-LHC [5]. Instead of protons, electrons and their antiparticles, positrons, will be colliding with each other at very high energies.

There are two ways to explore the subatomic world, the first is to go to higher energy to discover new particles and measure their properties, the second is to increase the precision of the measurements to detect rare processes and make detailed studies. The LHC allows the exploration of the electroweak symmetry breaking mechanism and other physical phenomena at the TeV scale, like the CP violation problem, the quark gluon plasma at the search of new physics beyond the Standard Model (BSM) such as supersymmetry (SUSY) among others. The discoveries made in these fields will make the Higgs factories a precise tool to further understand the nature of such processes having access to very precise studies. The advantage of a Higgs factory with respect to the LHC is the cleanliness of the events where two elementary particles with known kinematics and spin (in case of polarized beam) define the initial state. The resulting precision of the measurements is achievable because of the high resolution possible in the detector due to a clean experimental environment, ability to scan systematically in c.o.m. energy and possibility of high degree of polarization. The confirmation of the SM [6] has been achieved through a combination of analyses from LEP, SLC, HERA, B-factories, Tevatron and the LHC. In this model the Higgs mechanism is responsible for the electroweak symmetry breaking and the masses of other particles. A Higgs factory can be used to conclude if the boson found at LHC has the properties predicted by the SM or if it is part of an extended Higgs sector as in SUSY [7, 8]. An other aspect is that a Higgs factory can study the presence of composite structure of the Higgs particle and can measure precisely the electroweak coupling of the top quark by directly measuring the top quark mass.

Two accelerators design concepts are possible as **Higgs factories**: the **linear** and the **circular** colliders. In a simplistic approach the choice of linear rather than circular e^+e^- colliders to study the particle physics at the TeV energy regime is driven by the amount of radiated energy when a charged particle traverses bending magnetic fields, called Synchrotron Radiation (SR). The radiated power emitted during transverse acceleration of relativistic charged particles is given by:

$$P_s = \frac{e^2 c}{6\pi\varepsilon_0} \frac{E^4}{(m_0 c^2)^4 \rho_r^2} \tag{1.1}$$

where e is the electron charge, ε_0 is the electric permittivity of vacuum, c the speed of light, E is the particle energy, m_0 is the rest mass and ρ_r is the bending radius of the particle trajectory.

Given these facts, one can limit the SR of e^+e^- circular collider by increasing the machine radius as shown in Eq. 1.1. On the contrary, the energy loss due to SR is negligible in

e^+e^- linear colliders allowing them to reach multi-TeV center-of-mass energy in a more efficient way.

Figure 1.1 shows the reachable luminosity per facility considering the E_{CM}, the centre of mass (c.o.m.) energy of the collider, as a figure of merit: **at low energies circular colliders trump** but there is a reduction at high energy due to SR; **at high energies linear colliders excel** but when we go through lower energies the luminosity per beam power is roughly constant [9].

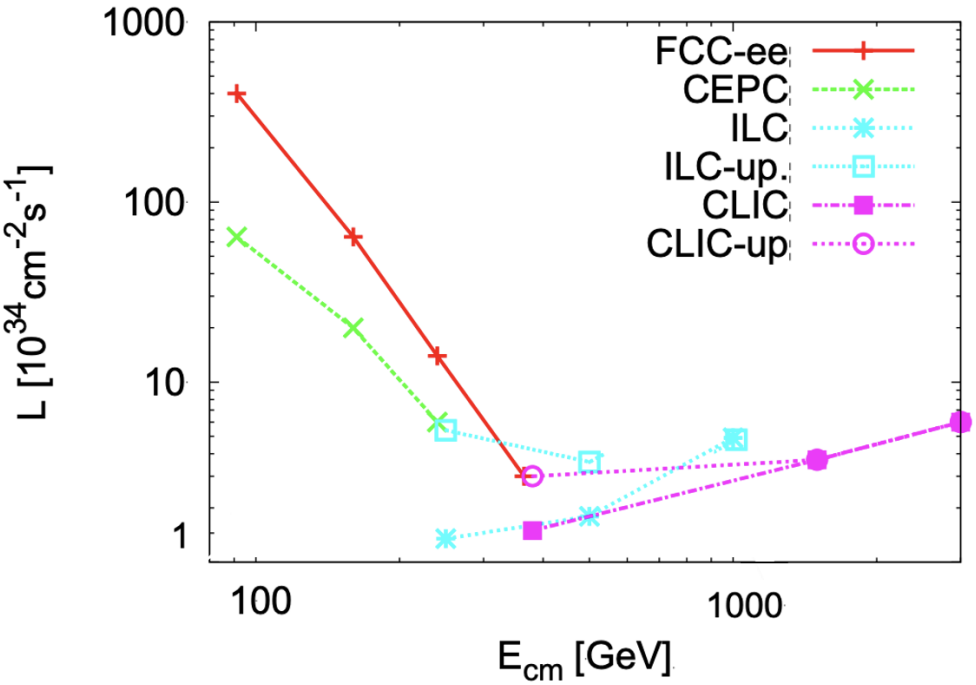

Figure 1.1: Reachable luminosity per facility considering the c.o.m. energy as figure of merit (Figure taken from [9]).

Different **e^+e^- linear and circular Higgs factories** are currently under design study [10]. For the **e^+e^- circular colliders** projects, the Future Circular Collider for e^+e^- collisions (FCC-ee) envisages a 80-100 km tunnel in the Geneva area with a centre-of-mass energy from 90 to 400 GeV [11]. The FCC-ee would be the first step towards the long-term goal of a 100 TeV proton-proton collider (FCC-hh) [12]. Another circular e^+e^- project under study is the Circular electron positron Collider (CepC) in China that envisage a 100 km tunnel with a centre-of-mass energy from 90 to 240 GeV [13].

For the **linear e^+e^- colliders** two projects are under study: the International Linear Collider (ILC) [14] and the Compact Linear Collider (CLIC) [15, 16]. This PhD will be focused on the linear proposal and more in particular on the Beam Delivery System of CLIC.

1.1 Linear collider concepts and beam dynamic issues

The accelerator sequence of a linear collider (half of it) is shown in Figure 1.2. The basic layout consists of the following subsystems:

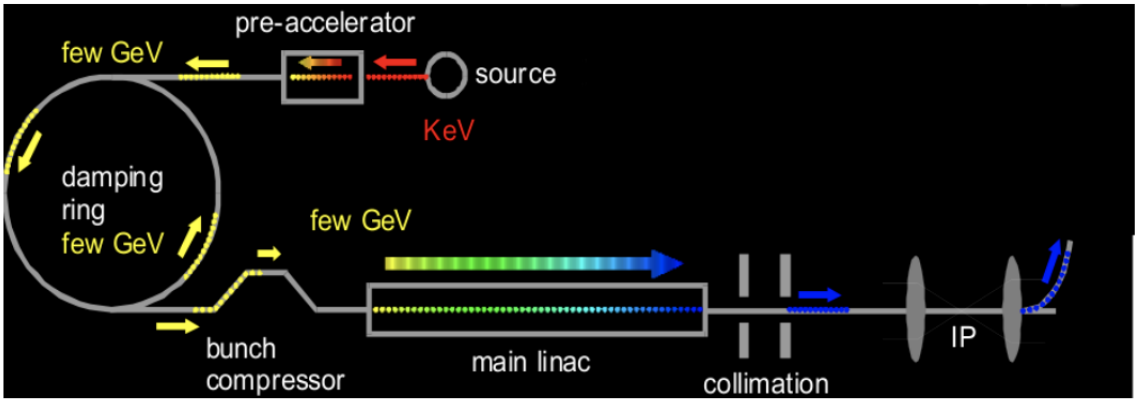

Figure 1.2: Conventional half linear collider layout [17].

- **Source**: produces the beam of particles, generates the particle bunches, provides initial acceleration and polarizes the beam if required. The electrons are usually generated by a laser illuminating a strained photocathode in a DC gun (see Figure 1.3 as example for the CLIC case). The positrons are created using an electron beam colliding with a target to form a photon beam. The photon beam then hits another target where the electron-positron pairs are generated. Positrons are then separated from the electrons, bunched and pre-accelerated.

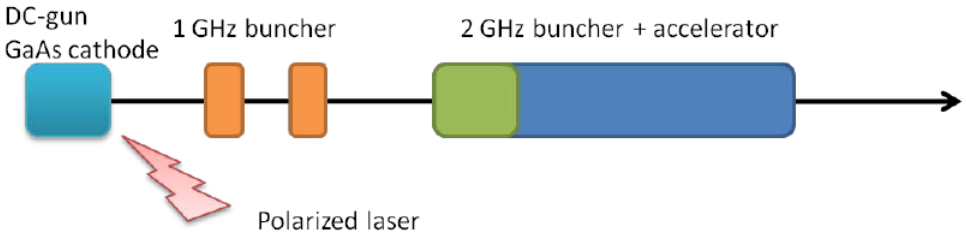

Figure 1.3: Schematic of the CLIC polarized electron source and bunching system (Figure taken from [15]).

- **Damping Ring (DR)**: accepts e^+e^- beams with large transverse emittance, which are then damped by a few orders of magnitude in order to fulfill the tight requirements of beam sizes. The transverse emittance damping occurs because of the SR being emitted by the beam in the arcs and in the damping wigglers located in the

straight sections of the ring. The straight sections also accommodate the accelerating cavities that compensate for the radiated energy, the injection and extraction sections and other sections used to adjust the beam phase and the ring circumference (see Figure 1.4 as example for ILC case).

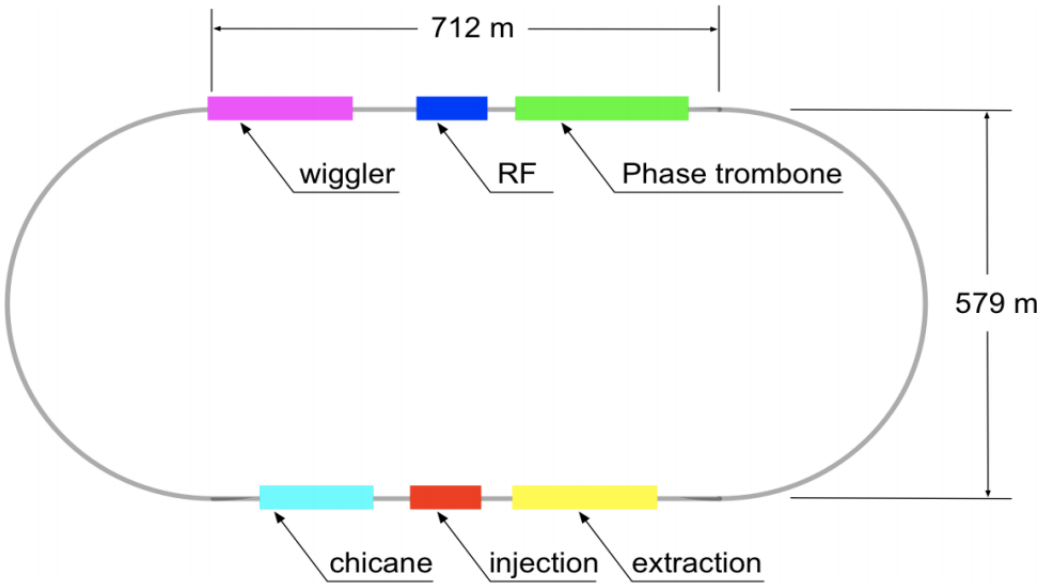

Figure 1.4: Schematic of the ILC DR layout (Figure taken from [14]).

- **Ring to Main Linac Transport (RTML)**: connects the DRs and the Main Linacs (MLs). It matches bunch length and energy from the values given by the DRs to the values required by the MLs. It includes sections for longitudinal bunch compression, acceleration, spin rotation and collimation (see Figure 1.5 as example for CLIC case).

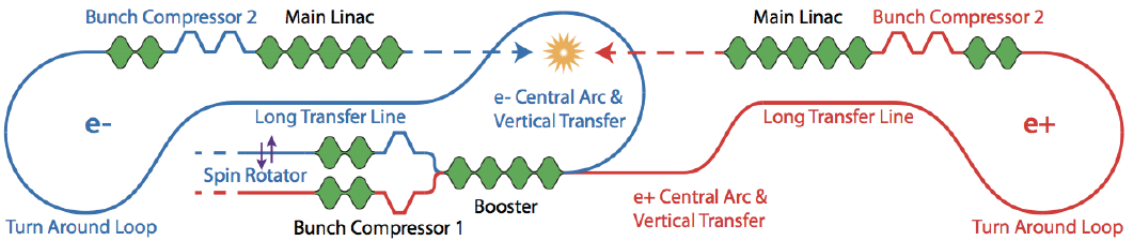

Figure 1.5: Schematic of the CLIC RTML (Figure taken from [16]).

- **Main Linac (ML)**: accelerates the beam to the collision energy. It consists of many successive arrays of coupled Radio-Frequency (RF) cavities used for beam acceleration, interleaved by quadrupoles used to center the beam on axis. A very

high accelerating gradient is required in order to keep the linac length short. In the case of the ILC the cavities are Super Conducting (SC) (see Figure 1.6) providing an average gradient of 31.5 MV/m [14]. For CLIC the accelerating structures are Normal Conducting (NC) (see Figure 1.6) and a high gradient of 100 MV/m [16] is achieved by extracting the power from the drive beams. In the case of the ILC main beams and CLIC drive beams the RF energy is produced in klystrons.

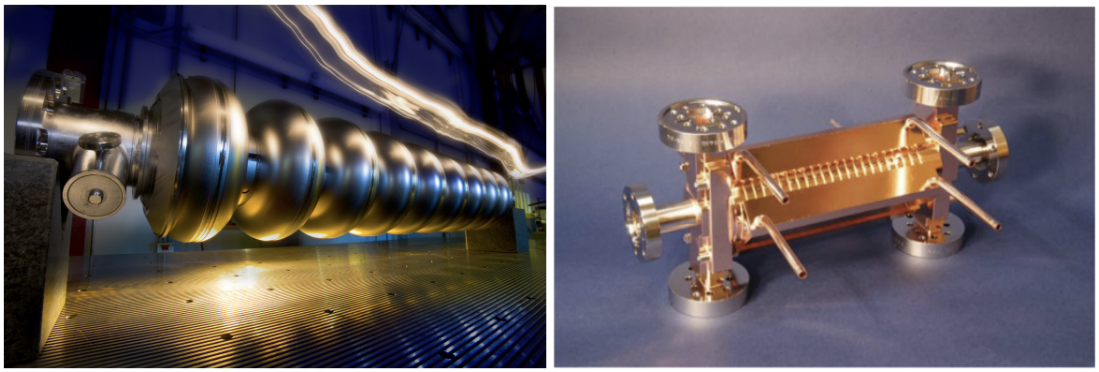

Figure 1.6: ILC SC RF cavity (left) and CLIC NC RF cavity (right) (Figures taken from [14, 15]).

- **Beam Delivery System (BDS)**: transports the beam from the ML to the Interaction Point (IP) and prepares the beams for collisions. The BDS is one of the most complex system in a linear collider and it is made of different subsystems: the Diagnostic Section (DS), the collimation section and the Final Focus System (FFS). The BDS measures the parameters of the linac beam and matches it into the FFS. Using the collimators the BDS protects the beamline and detector against mis-steered beams from the MLs and removes any large amplitude or off-energy particles (beam halo). It also measures and monitors the key physics parameters such as energy and polarisation. The FFS provides the beam size demagnification typically by a factor of several hundreds to fulfill the luminosity requirements. A more detailed description of this subsystem is given in Section 2.1.

1.1.1 Luminosity concept and its evaluation

The luminosity $\mathscr{L}$ in a linear collider can be expressed, assuming that the two colliding bunches have the same transverse spot sizes, same charge and the two beams collide head-on, as:

$$\mathscr{L} = \frac{f_{rep} n_b N_p^2}{4\pi\sigma_x^*\sigma_y^*} H_D \tag{1.2}$$

where σ_x^* and σ_y^* are the transverse rms spot sizes at the IP, N_p is the number of particles in a bunch (charge of the bunch), n_b is number of bunches per train, f_{rep} is the repetition frequency of the trains and H_D is the luminosity enhancement factor caused by the focusing of the particles due to electromagnetic forces of the opposite bunch. H_D is in the order of 1.5-2 for CLIC at 3 TeV. The beam current is represented by the term $N_b n_b f_{rep}$ and is limited by the power consumption of the collider and its transfer efficiency into beam power. The luminosity is usually expressed in $\mathrm{cm}^{-2}\,\mathrm{s}^{-1}$. In some cases can be useful to rewrite the luminosity equation in terms of beam power (P_{beam}):

$$\mathscr{L} = \frac{P_{beam} N_p}{4\pi\sigma_x^*\sigma_y^* E_{cm}} H_D \tag{1.3}$$

The luminosity is therefore enhanced by minimizing the factor $\sigma_x^*\sigma_y^*$. However, beam-beam effects set a lower limit to the achievable horizontal beam sizes [18].

The electric charge interaction between bunches when the two bunches cross one another at the IP produces focusing for opposite charges and defocusing when bunches are of the same charge. This is called **pinch effect**. The change of trajectory leads to a loss of energy of the particles, called **beamstrahlung** [19]. In an $\mathrm{e}^+\,\mathrm{e}^-$ collider, the beams focus each other and so the pinch effect reduces the effective beam size and therefore increases the luminosity. The magnitude of the pinch effect is described by the disruption parameter $D_{x,y}$:

$$D_{x,y} = \frac{2N_p r_e \sigma_z}{\gamma\sigma_{x,y}^*(\sigma_x^* + \sigma_y^*)} \tag{1.4}$$

where σ_z is the longitudinal beam size and r_e is the electron radius. When the beams focus each other they emit radiation called beamstrahlung. Due to this effect, particles lose energy and therefore collide with less than the initial energy. The beamstrahlung impact on the luminosity spectrum is described by the parameter Υ defined as [19]:

$$\Upsilon = \frac{2}{3}\frac{\hbar\omega_c}{E} \tag{1.5}$$

where $\hbar$ is the Planck constant, ω_c is the critical frequency characterizing the synchrotron light spectrum. The factor $\hbar\omega_c$ is called the critical energy. The average value of the beamstrahlung parameter could be estimated as:

$$\langle\Upsilon\rangle = \frac{5}{6}\frac{N_p r_e}{\alpha\sigma_z(\sigma_x^* + \sigma_y^*)} \tag{1.6}$$

where α is the fine structure constant. The number of photons emitted per beam particles N_γ depends on the bunch charge and transverse dimensions:

$$N_\gamma \propto \langle\Upsilon\rangle\frac{\sigma_z}{\gamma} \propto \frac{N_p}{(\sigma_x^* + \sigma_y^*)} \tag{1.7}$$

and the average energy of each photon is proportional to:

$$E_\gamma \propto \langle \Upsilon \rangle \frac{1}{\gamma} \propto \frac{N_p}{(\sigma_x^* + \sigma_y^*)\sigma_z} \tag{1.8}$$

In order to reduce the beamstrahlung while delivering maximum luminosity, the FFS aims to provide beams at the collision point with transverse sizes that maximize the sum $(\sigma_x^* + \sigma_y^*)$ and minimize the product $(\sigma_x^* \sigma_y^*)$. This can be achieved by using **flat beams** $(\sigma_x^* \gg \sigma_y^*)$. Under this condition one can approximate $(\sigma_x^* + \sigma_y^*) \approx \sigma_x^*$ and therefore the number of beamstrahlung photons emitted is proportional to the term N_p/σ_x^*. Therefore, because of the beamstrahlung emission, there will be pairs of particles that will collide at energies different from the nominal c.o.m. energy.

In order to evaluate this effect, we define the **peak luminosity** $\mathscr{L}_{peak}$ (or $\mathscr{L}_{\%}$) and the **total luminosity** $\mathscr{L}_{TOT}$. The total luminosity takes into account the luminosity delivered by all the collisions, even if they collide at different energy from the nominal. Peak luminosity only takes into account the luminosity delivered by those collisions produced above the 99% of the nominal energy (denoted as $\mathscr{L}_{peak}$). For a beamstrahlung free collision $\mathscr{L}_{TOT} = \mathscr{L}_{peak}$ while for collisions taking into account beamstrahlung emission $\mathscr{L}_{TOT} > \mathscr{L}_{peak}$ and a long tail spectra of collisions out of the nominal energy appears.

Beam-beam effects are crucial for the design the linear colliders, especially for the FFS. The beamstrahlung is one of the major limitations for the luminosity and also affects the performance of the experiments by producing backgrounds [20].

Since the Twiss function β has their minimum at the IP and increase with the distance, to consider the beam size constant along the whole collision length in some cases is not a good approximation. In the FFS, a low-β region, the β-function varies with the longitudinal distance s as:

$$\beta(s) = \beta^* \left[1 + \left(\frac{s}{\beta^*} \right)^2 \right] \tag{1.9}$$

and there the beam size increases like:

$$\sigma(s) = \sigma^* \sqrt{1 + \left(\frac{s}{\beta^*} \right)^2} \tag{1.10}$$

Because of the shape of the β-function this effect is called the **hourglass effect**. This is specially important when the β values are comparable to the bunch length σ_z and not all the particles collide at the minimum of the transverse beam size and therefore a luminosity reduction is observed. Taking into account the variation of the beam size/β-functions (Eqs. 1.9 and 1.10) in the overlapping integral we have to re-evaluate the expression for the luminosity. Assuming a symmetric collider with $\sigma_y^* \ll \sigma_x^*$ we obtain a reduction with respect to the nominal luminosity $\mathscr{L}_0$ [21]:

$$\frac{\mathscr{L}}{\mathscr{L}_0} = \frac{\beta_y^*}{\sqrt{\pi}\sigma_z} \mathrm{e}^{\frac{\beta_y^{*2}(1+\Theta^2)}{2\sigma_z^2}} K_0 \left(\frac{\beta_y^{*2}(1+\Theta^2)}{2\sigma_z^2} \right) \tag{1.11}$$

where K_0 is the Bessel function and Θ is the Piwinski angle defined afterwards. This effect gives the optimal value of the vertical β-function at the IP that maximizes luminosity which is usually $\beta_y^* \approx \sigma_z$.

Another important design parameter is the **crossing angle at IP** (θ_c). In fact, a horizontal crossing angle between the beams at the IP is introduced in the linear colliders BDS to cleanly extract the spent beam and to allow the IR quadrupoles to fit into the available space (see Figure 1.7). This crossing scheme produces a luminosity loss with respect to the head on collision according to,

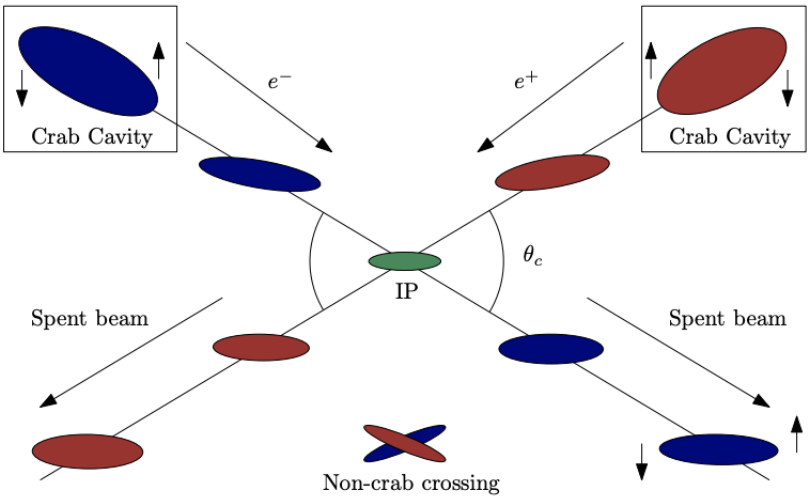

Figure 1.7: Crossing angle scheme and Crab Cavities location (Figure taken from [22]).

$$\mathscr{L} \approx \mathscr{L}_{headon} \frac{1}{\sqrt{1+\Theta^2}} \tag{1.12}$$

where Θ is the Piwinski angle, given by,

$$\Theta = \frac{\sigma_z \tan(\theta_c/2)}{\sigma_x} \tag{1.13}$$

where σ_z the bunch length and σ_x the horizontal beam size [18]. Since, this luminosity reduction might be significant, some way to compensate this effect while keeping the crossing angle is required. This task is performed by crab cavities. They apply a transverse kick in such a way that the head and the tail of the bunch are kicked in opposite directions resulting into a global rotation of the bunch. The sign of the tilt is such that the two bunches are in line during collision. The final result is that, in the bunch reference system, they interact with zero crossing angle and the luminosity loss due to the crossing angle is recovered [18].

One of the main roles of the FFS is to demagnify the beam such that it reaches a small size at the IP. In an ideal case the **IP beam size** depends only on the $\beta_{x,y}^*$ and

$\varepsilon^*_{x,y}$ values. In practice, the beam dynamic's imperfections (e.g. non-zero dispersion, chromaticity, stability, etc.) make the actual IP beam size larger. Assuming a Gaussian particle distribution of the beam in all six-dimensions, the expected **beam size** $\sigma_{x,y}$ from the Twiss parameters is given by:

$$\sigma_{x,y}(s) = \sqrt{\varepsilon_{x,y}\beta_{x,y}(s) + \sigma_\varepsilon^2 \eta_{x,y}^2(s)} \tag{1.14}$$

where $\varepsilon_{x,y}$ are the emittances that contain 1σ of the Gaussian particle distribution of the beam and σ_ε is the relative energy spread of the beam. Anyway different beam size definitions may be of interest depending on the purpose of the study, in this sense the core of the beam is of special interest when referring to linear colliders, since it is the part of the beam that largely contributes to the luminosity. This is defined as the variance of a Gaussian distribution, **core beam size** σ_{core}, obtained from the Gaussian distribution fitted to the histogram of a bunch of particles. The beam size error is the given error by the fit. Another definition is the **rms beam size** σ_{rms} defined as the root mean square of the particle distribution. It is evaluated as:

$$\sigma_{rms} = \sqrt{\int_{-\infty}^{\infty} (u-\bar{u})^2 \rho \, dv} \tag{1.15}$$

where u stands for x, x', y, y' and ρ is the particle density distribution.

The σ_{core} is the smallest value of the two beam size definitions because it almost neglects the tails of the bunch, while σ_{rms} is the largest beam size because it takes into account the tails of the bunch. The two beam size are usually sorted as:

$$\sigma_{core} \leq \sigma_{rms} \tag{1.16}$$

the equalities are satisfied when the beam can be represented by a Gaussian distribution, that occurs if the beam size expected from the Twiss parameters equals the σ_{rms} [18].

1.1.2 Chromaticity and its correction

A quadrupole magnet focuses particles at different longitudinal positions according to their momentum, as it is shown in Figure 1.8. This effect is referred to **chromaticity** and it is crucial in the FFS optics design. To quantitatively estimate this effect on the IP beam sizes we could consider a quadrupole characterized by its normalized gradient K_0. Particles with a relative momentum deviation $\delta_p = \frac{p-p_0}{p_0}$ will see a quadrupole of normalized gradient:

$$K = \frac{e}{p}\frac{\partial B_x}{\partial y} = \frac{e}{p_0(1+\delta_p)}\frac{\partial B_x}{\partial y} \approx K_0(1-\delta_p) \tag{1.17}$$

The integrated normalized gradient k of a quadrupole is defined by $k = Kl_q$ with l_q the length of the quadrupole. If l_q satisfies the condition $l_q \ll (Kl_q)^{-1}$ it is a good approximation to treat the quadrupole magnet as a thin lens of zero length while keeping finite its

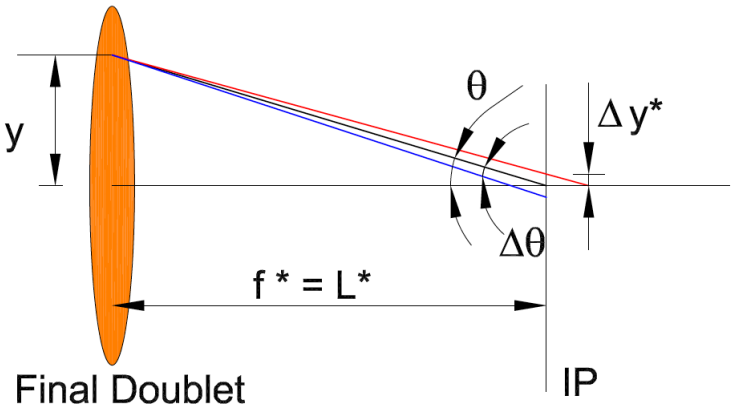

Figure 1.8: Scheme of the chromatic aberration induced by the FD. The red, blue and black lines show the trajectory of particles arriving at the FD with the same y coordinate but with larger, smaller and equal momentum respectively than the reference one (Figure taken from [23]).

k. The horizontal and vertical kicks $\Delta x', \Delta y'$ received by an off-momentum particle into a focusing thin lens quadrupole are given respectively by:

$$\Delta x' = -kx = -k_0(1-\delta_p)x = -k_0 x + k_0 x\delta_p \tag{1.18}$$

$$\Delta y' = +ky = +k_0(1-\delta_p)y = +k_0 y + k_0 y\delta_p \tag{1.19}$$

In the case of the FD, it is possible to approximate a unique thin lens of focal length (f^*) as:

$$f^* = \frac{1}{K_0 l_q} \tag{1.20}$$

which coincides with L^* that is defined as the length of the last drift.

The vertical displacement y is typically of the order of millimetres and L^* is of the order of meters, the IP angle

$$\theta \approx \frac{y}{f^*} = \frac{y}{L^*} \tag{1.21}$$

as Figure 1.8 shows. Therefore the displacement at the IP can be expressed as

$$y^* \approx L^* \Delta\theta. \tag{1.22}$$

Identifying the terms proportional to δ_p in Eq. (1.18) and Eq. (1.19) as sources of $\Delta\theta$, it can be obtained that:

$$\Delta y^* \approx L^* k_0 y \delta_p, \tag{1.23}$$

considering that $k_0 = 1/L^*$, Eq. (1.23) becomes:

$$\Delta y^* \approx L^* \theta \delta_p \tag{1.24}$$

To estimate the impact of this aberration on the rms vertical beam size it is assumed that there is no correlation between the energy and the angle, in this case the Eq. (1.24) becomes:

$$\Delta y^*_{rms} \approx L^* \theta_{yrms} \sigma_\varepsilon \tag{1.25}$$

where θ_{yrms} is the rms angle or equivalently the divergence of the beam at the IP and σ_ε is the energy spread. The relative vertical beam size increase at the IP is related to the ideal design IP vertical beam size σ^*_y as:

$$\frac{\Delta y^*_{rms}}{\sigma^*_y} \approx L^* \frac{\theta_{yrms}}{\sigma^*_y} \sigma_\varepsilon \tag{1.26}$$

Considering $\eta^*_{x,y} = 0$ therefore Eq.(1.26) could be expressed as:

$$\frac{\Delta y^*_{rms}}{\sigma^*_y} \approx \frac{L^*}{\beta^*_y} \sigma_\varepsilon \approx \xi_y \sigma_\varepsilon \tag{1.27}$$

where L^*/β^*_y is the leading term of the **natural vertical chromaticity** ξ_y introduced by the FD, which in a FFS it is the most important source of chromaticity for the vertical plane. Similar expressions could be found for the horizontal plane.

A more general definition of the natural chromaticity is given by:

$$\left(\frac{\sigma^*}{\sigma^*_0}\right)^2 = 1 + \xi^2 \sigma^2_\varepsilon + O\left(\sigma^4_\varepsilon\right) \tag{1.28}$$

where the natural chromaticity ξ is identified as the coefficient of the quadratic term in the approximation. In order to avoid this detrimental effect due to the energy spread, the chromaticity needs to be corrected and this is done by sextupole magnets added in a non-zero dispersion region and near quadrupoles.

In the case of the **FFS** different schemes have been developed for the chromaticity correction of the linear collider: the **traditional chromaticity correction scheme**, referred as traditional scheme, and the **local chromaticity correction scheme**.

The traditional chromaticity correction scheme, experimentally validated at FFTB [24], consists in two dedicated sections for the horizontal and vertical chromaticity correction, called CCX and CCY respectively. The sextupoles are introduced in pairs in high horizontal dispersion η_x and high β values and separated by a π phase advance, allowing a minus identity transformation matrix between them (-*I*) for the cancellation of the second order geometrical aberrations introduced by these sextupoles. The chromaticity is fully compensated in CCX and CCY and thus the dispersion is zeroed downstream of the FD. The non-zero dispersion regions are introduced by the bending magnets, in both chromaticity correction sections as illustrated in Figure 1.9. In order to be applicable to

multi-TeV scale e^+e^- colliders, the traditional scheme must have long and weak bending magnets in order to minimize the SR emitted which can significantly degrade the luminosity. Therefore, the traditional FFS scheme optimized and proposed for CLIC 3 TeV is 1503 meters [25, 26], see Figure 1.10.

Furthermore, in order to increase the energy acceptance of the FFS, in [27] has been proposed to add extra sextupoles all along the chromatic correction sections. This allows to relax the main sextupoles and to increase the energy acceptance. This scheme was studied in [22] for CLIC 3 TeV.

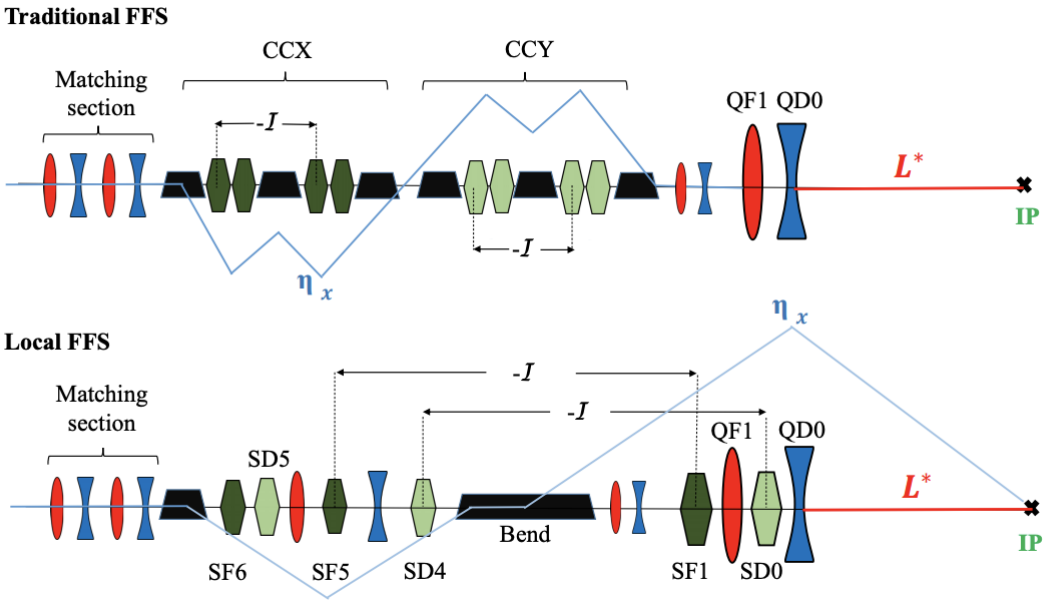

Figure 1.9: Simplified layout of the Traditional FFS scheme (top) versus the Local chromaticity correction scheme (bottom). The blue lines represents the horizontal dispersion η_x along the system. The sextupoles are represented by green hexagons (Figure taken from [28]).

The Local chromaticity correction scheme uses interleaved pairs of sextupole magnets in the FD region in order to locally and simultaneously correct horizontal and vertical chromaticity. Upstream bending magnets generate dispersion throughout the FFS which is then zeroed at the IP. Sextupoles placed in FD region generate second order dispersion. However, it can be compensated simultaneously with horizontal and vertical chromaticity provided that half of the total horizontal chromaticity of the whole FFS is generated upstream. Geometrical aberrations are cancelled by separating the sextupoles with a *-I* matrix transformation. Two more sextupoles (SF6 and SD5 shown in Figure 1.9) are used to correct higher order aberrations. This scheme requires fewer bending dipoles, making the FFS more compact than the traditional scheme with a total length of about 450 meters, see Figure 1.10. It also shows larger momentum bandwidth, which represents the

luminosity loss due to the possible energy mismatch coming from the linac, thanks to the locality of the correction [29]. This new scheme, is considered as baseline for CLIC and ILC FFS and it has been tested at ATF2 [30].

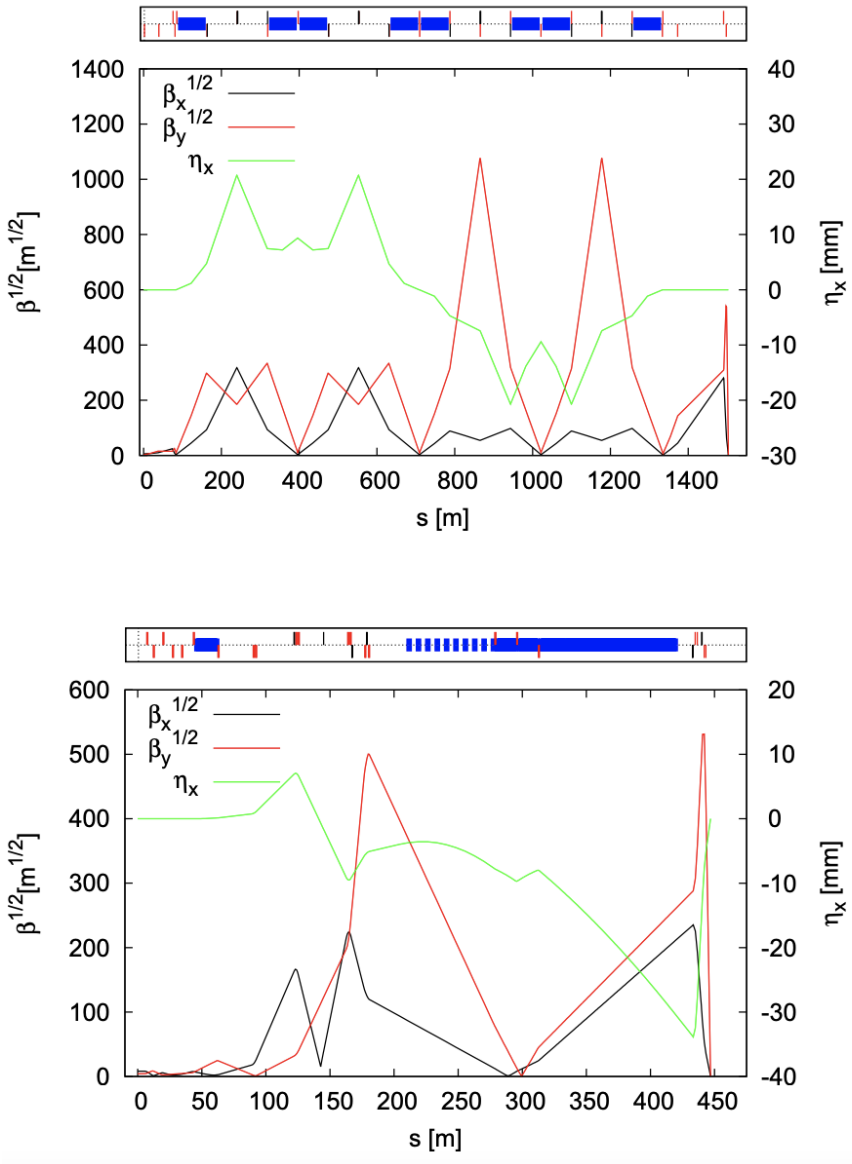

Figure 1.10: Optics of the CLIC 3 TeV traditional correction scheme (top) and local correction scheme (bottom) FFS showing horizontal and vertical β-functions and dispersion function (Figure taken from [22]).

1.1.3 SR effects for Linear Colliders

SR is one of effects that can dilute the beam size and the luminosity in a collider, specially at high energies. There are two cases where the SR emission is important in a linear collider: **radiation in bending magnets** and **radiation in quadrupoles**, known as the **Oide effect** [31].
To mitigate the luminosity loss due to the SR emitted in the bending magnets in the BDS and following Eq. 1.1, the bending radius ρ_r needs to be as large as possible, which determines the length of the the BDS.
This effect will be crucial in the dual BDS optics design of the CLIC 3 TeV case.

In the quadrupoles, the SR emission, mainly the ones conforming the FD of a linear collider [31] sets a fundamental limit in the minimum spot size at the IP and the final luminosity. The minimum spot size is determined by the emittance of the beam at the entrance of the FFS and the FD parameters, the β^* at the IP. The minimum spot size is given by the expression:

$$\sigma_y^{*2} = \beta_y^* \varepsilon_y + \frac{110}{3\sqrt{6\pi}} r_e \lambda_e \gamma^5 F(\sqrt{K} l_q, \sqrt{K} L^*) \left(\frac{\varepsilon_y}{\beta_x^*}\right)^{5/2} \tag{1.29}$$

where the function $\mathrm{F}(\sqrt{K} l_q, \sqrt{K} L^*)$ is defined by:

$$F(\sqrt{K} l_q, \sqrt{K} L^*) = \int_0^{\sqrt{K} l_q} \left| \sin\phi + \sqrt{K} L^* \cos\phi \right|^3 \left[\int_0^{\phi} \left(\sin\phi' + \sqrt{K} L^* \cos\phi' \right)^2 d\phi' \right]^2 d\phi . \tag{1.30}$$

λ_e is the Compton wavelength. This limit must be taken into account carefully since the nominal spot size is usually very close to the minimum and sometimes, mainly for high energy cases, an optimization of the quadrupole length is needed to keep this limit below the nominal beam size.

1.2 The Future Linear Colliders: the ILC and the CLIC projects

Two e^+e^- linear colliders have been proposed as future machines for the Higgs factory: the **International Linear Collider (ILC)** and the **Compact Linear Collider (CLIC)**. In the following a detailed description of the two proposals is given.

1.2.1 The ILC project

The ILC is based on 1.3 GHz SC RF accelerating cavities with gradient of 31.5 MV/m each. The same cavities are being used by the European XFEL facility at DESY [32]. The

ILC is designed to achieve center-of-mass energy range between 250 GeV and 500 GeV in the first four years of operation. The machine could be upgraded to a center-of-mass of 1 TeV [14, 33]. The total footprint of the ILC complex is ≈ 21 km long. The ILC BDS, in particular, is 2.2 km long and brings the beam into collision with a crossing angle of 14 mrad at a single IP which can be occupied by two detectors in a so-called "push-pull" configuration [14].

The main beam parameters are summarized in Table 1.1 while the schematic layout is shown in Figure 1.11.

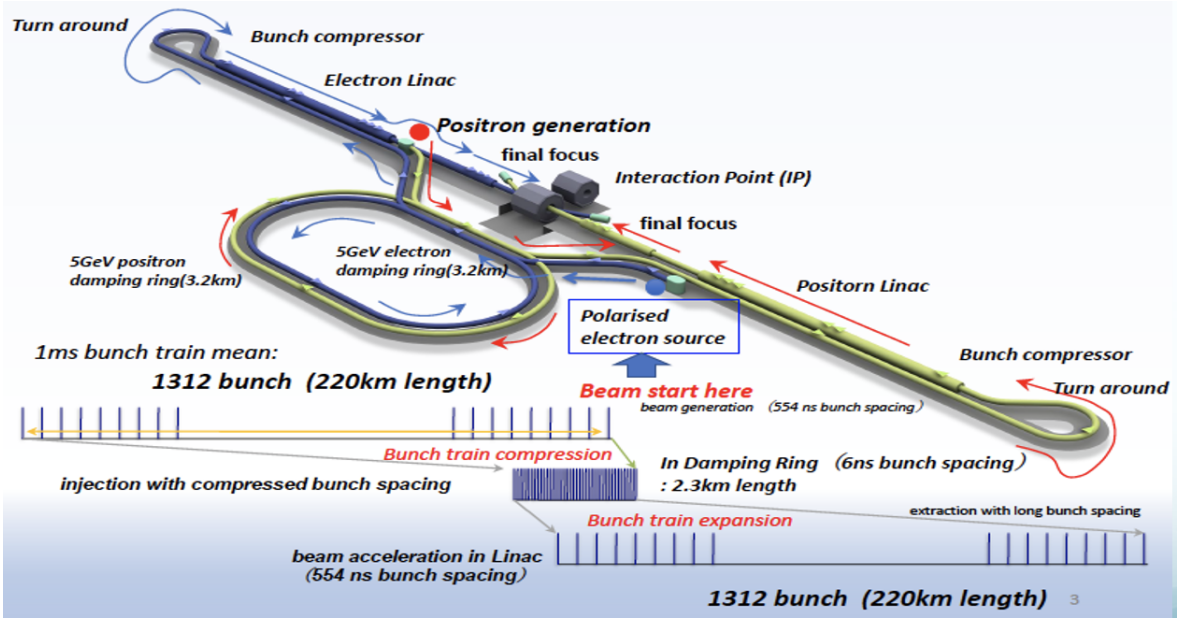

Figure 1.11: Schematic overview of the ILC 250 GeV layout with the IR placed in the middle of the site [33].

The main subsystems of ILC are:

- **Electron and Positron source**: The electron source design is based on the SLC polarized electron source, which has demonstrated that the bunch charge, polarisation and cathode lifetime parameters are feasible. The long bunch trains of the ILC do require a newly developed laser system and powerful pre accelerator structures, for which preliminary designs are available. The design calls for a Ti:sapphire laser impinging on a photocathode based on a strained GaAs/GaAsP superlattice structure, which will produce electron bunches with an expected polarisation of 85%, sufficient for 80% beam polarization at the interaction point, as demonstrated at SLAC.

  One of the most challenging systems for any e^+e^- collider is the positron production, see Figure 1.12. In the case of ILC is even more challenging because we need a e^+ yield production of 1.5 (2×10^{10} e^-). The most efficient obtained has been SLC

Table 1.1: Parameters for the ILC energy stages.

ILC	**Stage 1**	**Stage 2**	**Stage 3**
Centre of mass energy $\sqrt{s}$ [GeV]	250	500	1000
Repetition rate f_{rep} [Hz]	5	5	4
Number of bunches n_b	1312	1312	2450
Bunch separation [ns]	554	554	366
Pulse length [ms]	200	200	200
Main tunnel length [km]	20.5	31	40
Bunch length σ_z [mm]	0.3	0.3	0.225
Number of particles per bunch N [10^{10}]	2	2	1.737
IP beam size σ_x [μm]	0.515	0.474	0.335
IP beam size σ_y [nm]	7.66	5.86	2.66
Normalised emittance at the IP ε_x [μm]	5.0	10	10
Normalised emittance at the IP ε_y [nm]	35	35	30
Estimated power consumption P_{wall} [MW]	111	173	300
Luminosity $\mathscr{L}_{TOT}$ [10^{34} cm^{-2}s^{-1}]	1.35	1.79	5.11

with a yield factor of 1. Two concepts for positron production are considered in ILC. The baseline solution employs SC helical undulators at the end of the electron main linac, producing polarised photons that are converted to positrons in a rotating target, with a 30% longitudinal polarisation. This positron-production scheme requires an operational electron linac delivering a beam close to its nominal energy of 125 GeV, which is a complication for commissioning and operation.

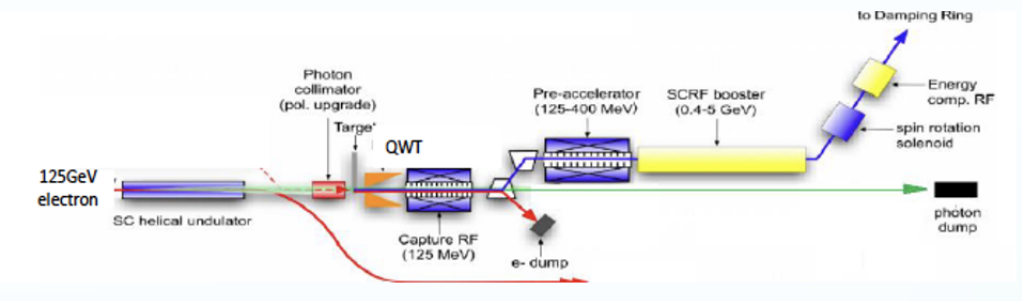

Figure 1.12: Overall ILC Layout of the Positron Source SC helical undulators, located at the end of the electron ML [14].

- **Damping rings**: The ILC includes two oval DRs of 3.2 km circumference, sharing a common tunnel in the central accelerator complex. The DRs reduce the horizontal and vertical emittance of the beams by almost six orders of magnitude within a time span of only 100 ms, to provide the low emittance beams required at the IP. Both DRs operate at an energy of 5 GeV. The DRs' main objectives are: to accept electron and positron beams at large emittance and produce the low-emittance

beams required for high-luminosity production; to dampen the incoming beam jitter to provide highly stable beams; to delay bunches from the source and allow feed-forward systems to compensate for pulse-to-pulse variations in parameters such as the bunch charge [33].

- **Ring to Main Linac (RTML)**: The RTML system is responsible for transporting and matching the beam from the DR to the entrance of the ML. Its main objectives are: transport of the beams from the DRs at the center of the accelerator complex to the upstream ends of the MLs; collimation of the beam halo generated in the DRs; rotation of the spin polarisation vector from the vertical to the desired angle at the IP (typically, in longitudinal direction). The RTML consists of two arms for the positrons and the electrons. Each arm comprises a DR extraction line transferring the beams from the DR extraction into the ML tunnel, a long low emittance transfer line (LTL), the turnaround section at the upstream end of each accelerator arm, and a spin rotation and DS. The long transport line is the largest, most costly part of the RTML. The main challenge is to transport the low emittance beam at 5 GeV with minimal emittance increase, and in a cost-effective manner, considering that its total length is about 14 km for the 250 GeV machine. In order to preserve the polarisation of the particles generated in the sources, their spins are rotated into a vertical direction (perpendicular to the DR plane) before injection into the DRs. A set of two rotators employing superconducting solenoids allows to rotate the spin into any direction required [33].

- **Bunch compressors and Main Linac**: The heart of the ILC are the two MLs, which accelerate the beams from 5 to 125 GeV. The linac tunnel has two parts separated by a shield wall. One side houses the beamline with the accelerating cryomodules as well as the RTML beamline hanging on the ceiling. The other side contains power supplies, control electronics, and the modulators and klystrons of the High-Level RF system. The concrete shield wall has a thickness of 1.5 m. The shield wall allows access to the electronics, klystrons and modulators during operation of the klystrons with cold cryomodules, protecting personnel from X-ray radiation emanating from the cavities caused by dark currents. Access during beam operation, which would require a wall thickness of 3.5 m, is not possible. The first part of the ML is a two-stage bunch compressor system each consisting of an accelerating section followed by a wiggler. The first stage operates at 5 GeV, with no net acceleration, the second stage accelerates the beam to 15 GeV. The bunch compressors reduce the bunch length from 6 to 0.3 mm. After the bunch compressors, the ML continues for about 6 km with a long section consisting entirely of cryomodules, bringing the beam to 125 GeV [33].

- **Beam Delivery System (BDS)**: The ILC BDS is designed such that it can be upgraded to a maximum beam energy of 500 GeV; components such as the beam dumps, that are not cost drivers for the overall project but would be cumbersome to

replace later, are dimensioned for the maximum beam energy from the beginning. In other places, such as the energy collimation dogleg, those components necessary for 125 GeV beam operation are installed and space for a later upgrade is reserved. Overall, the BDS is 2254 m long from the end of the main linac (or the undulator and target bypass insert of the positron source on the electron side, respectively) to the IP. The BDS starts with a DS, where emittance, energy and polarisation are measured and any coupling between the vertical and horizontal planes is corrected by a set of skew quadrupoles. The DS is followed by a collimation system, which first removes beam halo particles (betatron collimation). Then, off-momentum particles are removed. In this energy collimation section, sufficient dispersion must be generated by bending the beam in a dogleg, while avoiding excessive SR generation in dispersive regions that leads to an increase of the horizontal emittance. The final part of the BDS is the FFS that demagnifies the beam to the required spot size of 516×7.7 nm by means of a final quadrupole doublet. Even the relatively small energy spread of $\approx 0.1\%$ leads to a significant spread of the focal length of the doublet and requires a correction to achieve the desired beam size, which is realised by a local chromaticity correction scheme. To bring the beams to collision with the necessary nanometre accuracy requires a continuous compensation of drift and vibration effects. Along the ILC, the pulse length and bunch separation (727 μs and 554 ns, respectively) are large enough to allow corrections between pulses as well as within a bunch train (intratrain feedback). Beam-beam offsets of a fraction of the beam size lead to a measurable deflection of the outgoing beams,and these measurements are used to feed fast stripline kickers that stabilize the beam. Finally, the 3.9 GHz crab cavities close to the interaction point are incorporated that rotate the bunches to compensate for the 14 mrad beam crossing angle [33].

- **Machine Detector Interface (MDI)**: The ILC is configured to have two detectors that share one IP, with one detector in data taking position at any time, in a so–called "push–pull" operation. Both detectors are mounted on movable platforms that allow an exchange of the detectors within approximately 24 hours. In the push–pull scheme, the innermost final focus quadrupole "QD0", a slim, SC magnet package combined with a sextupole for local chromaticity correction, is installed within the detectors. The other part of the FD ("QF1") is located outside the detector on a bridge, and does not move with the detector. Since the TDR, the free space L* between interaction point and the QD0 edge has been harmonised to a common value of L* = 4.1 m, which facilitates the design of a FFS optics that delivers optimal and equal performance to both detectors. The detectors are located in an underground cavern [33].

1.2.2 The CLIC project

The Compact Linear Collider (CLIC) is the CERN linear collider project that aims to collide e^+ e^- beams with center of mass up to 3 TeV delivering a total luminosity $\mathscr{L}_{TOT}$ of

$5.9\times10^{34}\,\mathrm{cm}^{-2}\mathrm{s}^{-1}$ and a peak luminosity $\mathscr{L}_{1\%}$, coming from the collisions with energy larger than 99% of the maximum energy, of $2\times10^{34}\,\mathrm{cm}^{-2}\mathrm{s}^{-1}$. The high beam energy is achieved by an innovative two-beam acceleration design, using accelerating cavitites made of copper, delivering an accelerating gradient of 100 MV/m [34]. The CLIC accelerating scheme allows to increase the beam energy from 9 GeV, coming from the DRs, to 1.5 TeV in a single pass. Beam power is extracted from the drive beam and converted to RF power in special RF devices called PETS (Power Extraction and Transfer Structures) and it is then transported to the accelerating structures in the Main Beam. The high current drive beam is obtained by recombining the bunches coming from the drive beam accelerator. This recombination is done in the delay loop and the combiner rings CR1 and CR2 [35].

The optimised staging scenario foresees three main c.o.m. energy stages at 380 GeV, 1.5 TeV and 3 TeV for a full CLIC programme (see Table 1.2). The Conceptual Design Report (CDR) [15] published in 2012, projected collisions at 500 GeV c.o.m energy for the first energy stage. Recent studies for CLIC have converged towards a staged approach offering a more suitable physics programme for the post-LHC era. The first stage is proposed to be at 380 GeV [36]. At this energy, precision Higgs physics will be one of the main focuses of the CLIC programme with particular emphasis on the Higgsstrahlung process which dominates Higgs production at this energy. More details about physics potential at CLIC 380 GeV can be found in [37]. The implementation scenario CLIC energy stages is shown in Figures 1.13 and 1.14.

Table 1.2: Parameters for the CLIC energy stages.

CLIC	**Stage 1**	**Stage 2**	**Stage 3**
Centre of mass energy $\sqrt{s}$ [GeV]	380	1500	3000
Repetition rate f_{rep} [Hz]	50	50	50
Number of bunches n_b	352	312	312
Bunch separation [ns]	0.5	0.5	0.5
Pulse length [ns]	244	244	244
Accelerating gradient G [MV/m]	72	72/100	72/100
Main tunnel length [km]	11.4	29.0	50.1
Bunch length σ_z [μm]	70	44	44
Number of particles per bunch N [10^9]	5.2	3.7	3.7
IP beam size σ_x/σ_y [nm]	149/2.9	60/1.5	40/1
Normalised emittance (end of linac) $\varepsilon_x/\varepsilon_y$ [nm]	900/20	660/20	660/20
Estimated power consumption P_{wall} [MW]	168	364	589
Peak Luminosity $\mathscr{L}_{1\%}$ [$10^{34}\,\mathrm{cm}^{-2}\mathrm{s}^{-1}$]	0.9	1.4	2
Luminosity $\mathscr{L}_{TOT}$ [$10^{34}\,\mathrm{cm}^{-2}\mathrm{s}^{-1}$]	1.5	3.7	5.9

The first energy stage requires four decelerator structures in order to increase each beam energy to 190 GeV while an additional 21 decelerator are needed for the final energy

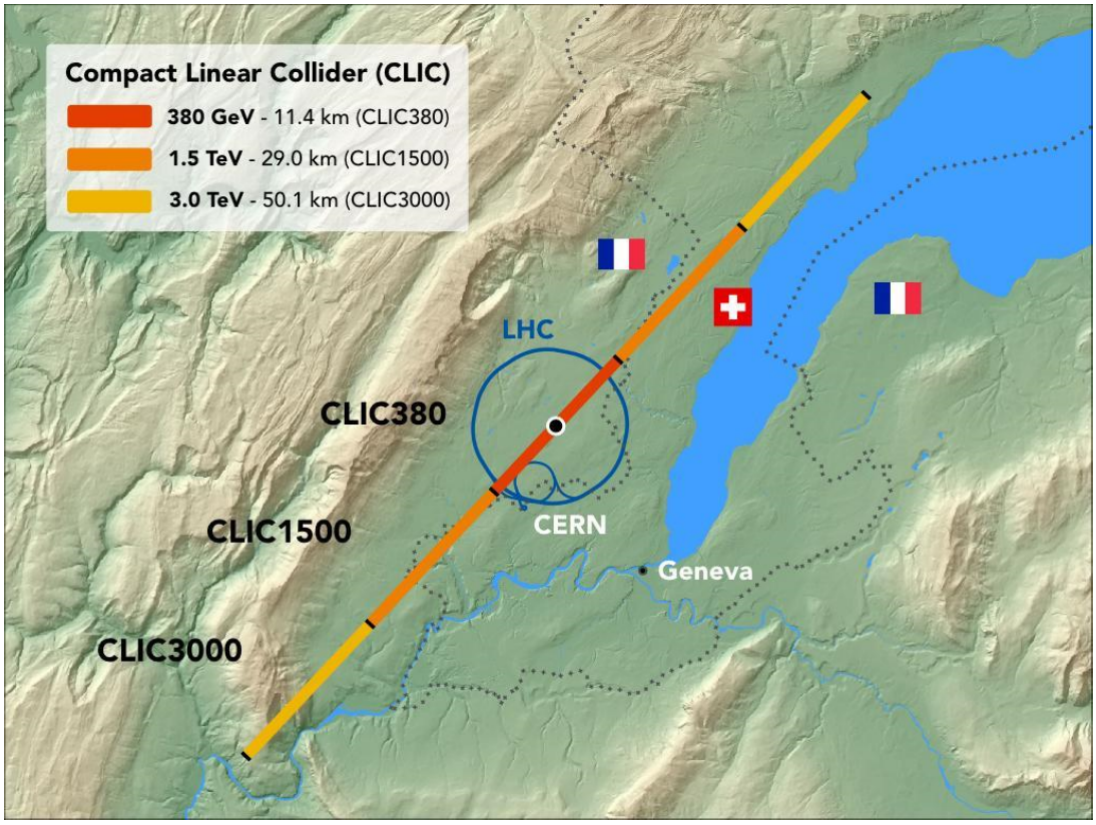

Figure 1.13: The CLIC Main Linac footprints near CERN, showing the three implementation stages (Figure taken from [16]).

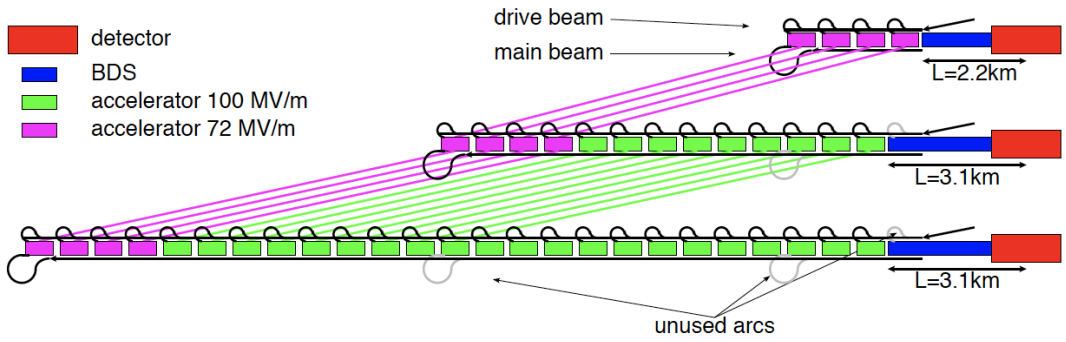

Figure 1.14: CLIC potential energy staging concepts for 380 GeV, 1.5 TeV and 3 TeV c.o.m. In this solution, the modules at the beginning of the previous main linac are moved to the new beginning during the upgrade (Figure taken from [16]).

stage. The CLIC 380 GeV uses a single drive-beam generation complex to feed both linacs while two are needed for CLIC 3 TeV as illustrated in Figures 1.15 and 1.16.

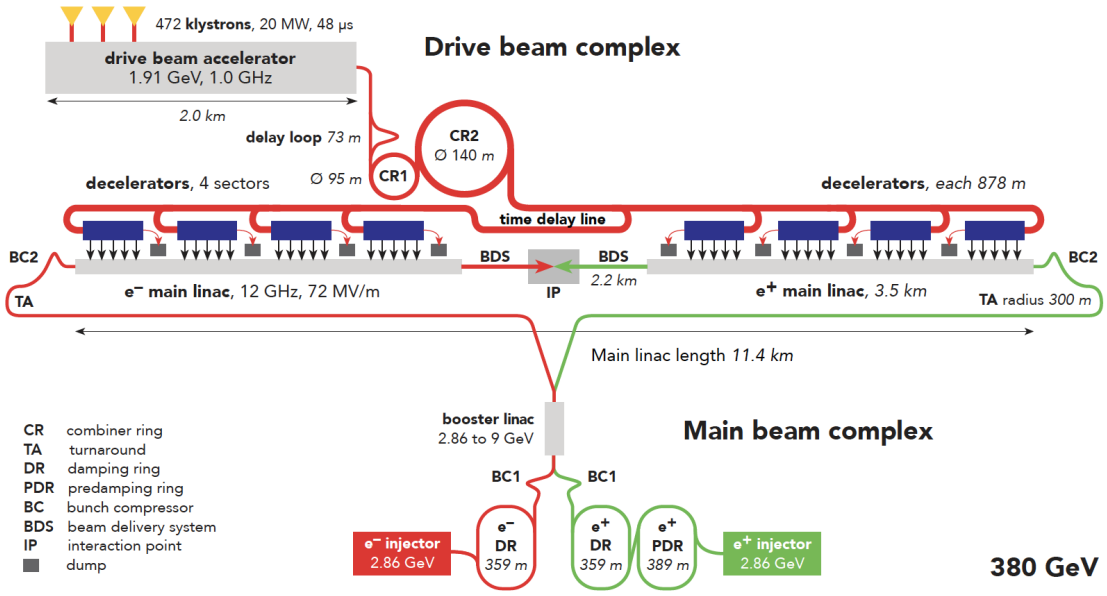

Figure 1.15: General scheme of the CLIC 380 GeV machine (Figure taken from [16]).

The main subsystems of CLIC are:

- **Main Beam Injectors**: The CLIC Main-Beam Injectors (MBIs) consist of a polarized electron source and a conventional un-polarized positron source (see Figure 1.17. Both particle species are pre-accelerated up to 200 MeV in individual linacs before they are injected into a common injector linac which increases their energy up to 2.86 GeV. The CLIC polarized electron source uses a DC-photo injector followed by a 2 GHz bunching and accelerating system. The spin-polarized electrons are generated using a polarized laser impinging on a strained GaAs cathode. The CLIC positron source consists of a 5 GeV electron beam impinging on a tungsten hybrid target (one thin crystal target plus one thick amorphous target) taking advantage of photon enhancement via the channelling process. The positrons are captured after the target with an adiabatic matching device and a 2 GHz capture linac accelerating the positrons up to 200 MeV. Particles coming from the source are pre-accelerated and transported towards the DR [16].

- **Damping Ring**: The DRs are a fundamental part of the CLIC injector complex and are required to damp the large emittance of the injector linac beams, particularly for positrons, in all three dimensions to obtain the desired luminosity. The normalized transverse emittance of the incoming beam is to be reduced to 500 nm and 5 nm

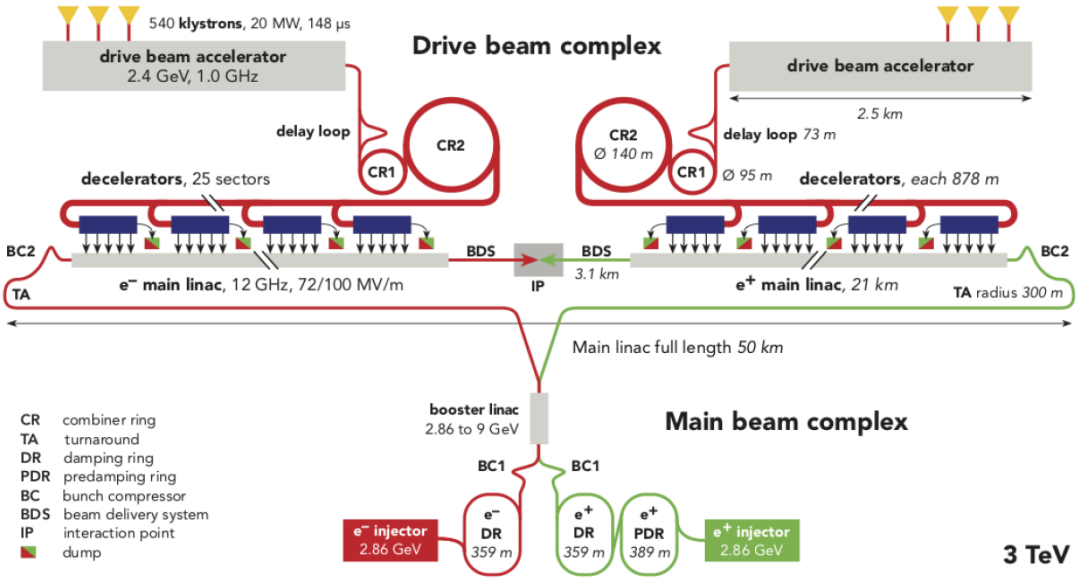

Figure 1.16: General scheme of the CLIC 3 TeV machine (Figure taken from [16]).

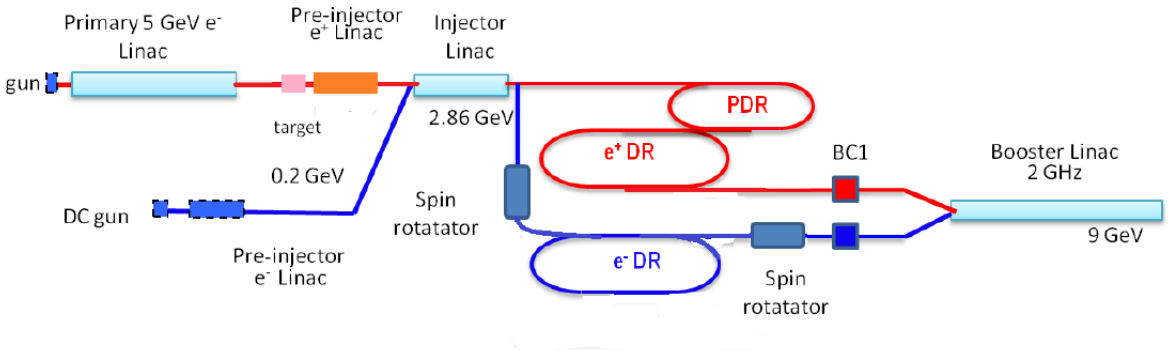

Figure 1.17: Schematic layout of the CLIC Main-Beam Injector complex (Figure taken from [16]).

in horizontal and vertical directions respectively at an energy of 2.86 GeV, corresponding to geometric emittances of around 90 pm rad and 0.9 pm rad. This is done in a few hundreds of milliseconds using the SR caused by SC wigglers [38]. A schematic view of the DR complex with the e^- and e^+ DR and the positron PreDR (PDR in red) is shown in Figure 1.17. In the original design, four rings were foreseen, a PDR and a main DR for each particle species. The PDRs were found to be necessary due to the large input emittance coming from the positron source, necessitating dynamic and momentum acceptances incompatible with the design of

a high-focusing ultra-low emittance main DR. In addition, the storing time of 20 ms corresponding to the high repetition collider rate of 50 Hz is not long enough to allow the large injected emittances to damp to the required output value. However, in the case of the electrons, a combination of a high-brightness source and a careful emittance preservation in the injector linac could allow for a transverse input normalised emittance value of around 10 μm, which is lower in the horizontal but higher in the vertical plane, with respect to the actual performance of the PDR [16].

- **Ring to Main Linac (RTML)**: this section transports the electron and the positron beams from their respective DR, at ground level, to the MLs start points, underground, see Figure 1.5. While transporting the beam and matching the geometric layout of the beam lines, the RTML must accomplish three tasks: preserve the ultra-low beam transverse emittances from the damping rings, increase the beam energy from 2.86 GeV to 9 GeV, and compress the bunch length from 1.8 mm to $\approx$ 70 μm. The total lengths of the two RTMLs are slightly different, as the two lines have to accommodate different beam line layouts and guarantee the correct arrival time of the beams at the IP.

- **Main Linac**: The two Main Linacs (MLs), one for positrons and one for electrons, accelerate the beams from an initial energy of 9 GeV to the final value of 190 GeV using normal conducting accelerating structures with an RF frequency of 12 GHz and a gradient of 72 MV/m. A key design goal is the preservation of the ultra-low transverse emittances during beam transport. This goal is achieved by a combination of careful lattice design, precise pre-alignment of the beam line components, stabilisation of the beam-guiding quadrupoles against vibrations and use of beam-based correction methods [16].

- **Beam Delivery System (BDS)**: The current baseline design for CLIC BDS foresees an L* of 6 metres with final quadrupoles mounted outside the detector volume directly on the tunnel floor. The Final Focus lattice with L* = 6 m has been lengthened by a factor 6/4.3 compared with the previous $\sqrt{s}$ = 500 GeV design. The length of the entire BDS is $\approx$ 1950 m and the FFS length is 770 m for the CLIC 3 TeV case. The crossing angle for the CLIC 3 TeV BDS is 20 mrad and the required crossing angle for the CLIC 380 GeV BDS is 16.5 mrad for the L* = 6 m BDS (see Figure 1.18). The FFS dipoles, quadrupoles and sextupoles have been optimized to match the desired beam parameters at the IP while locally correcting the chromaticity generated by the FD. A pair of octupoles has been introduced in the lattice to correct the remaining 3rd order chromatic and geometric aberrations.

- **Machine Detector Interface (MDI)**: Since the CDR [15], the final quadrupole QD0 has been moved from inside the detector (with L* = 3.5 m at 3 TeV or L* = 4.3 m at 380 GeV) to the tunnel floor outside the detector (using L* = 6 m for both 380 GeV and 3 TeV designs). The angular acceptance of the detector in the forward

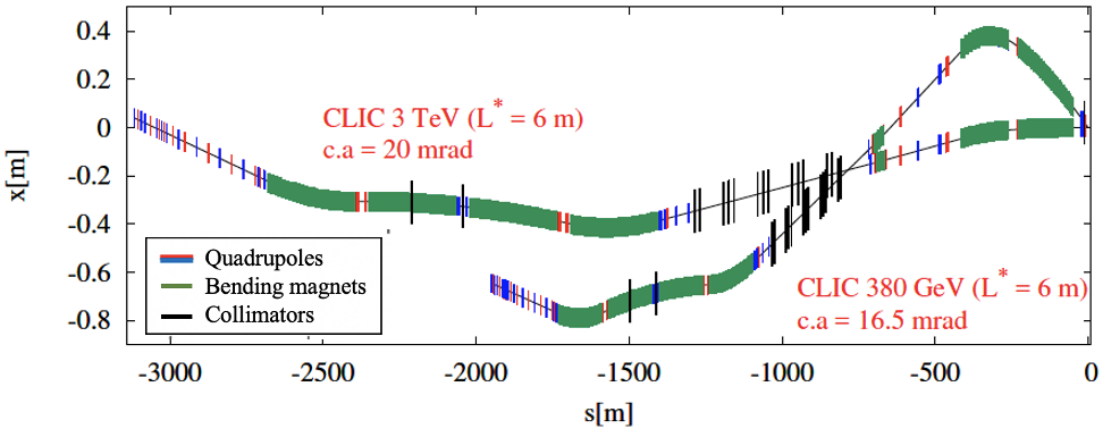

Figure 1.18: Schematic of CLIC BDS for 380 GeV and 3 TeV cases. Dipoles, quadrupoles and collimators are shown in green, red/blue and black, respectively. C.a. is the crossing angle.

region becomes significantly larger and a number of technical systems become simpler. The peak luminosity decreases only marginally. More detail on CLIC MDI in Chapter 3.

1.3 Linear Collider Test Facilities

In order to demonstrate some of the LC concepts as the two beams acceleration concept in the case of CLIC and the local chromaticity correction scheme two test facilities have been constructed: CTF3 at CERN and ATF2 at KEK.

1.3.1 CTF3

The aim of the CLIC Test Facility CTF3 (see Figure 1.19), built at CERN by the CLIC International Collaboration, was to prove the main feasibility issues of the Two-Beam acceleration technology. CTF3 consisted of a 150 MeV electron linac followed by a 42 m long Delay Loop (DL) and a 84 m Combiner Ring (CR). The beam current from the linac was first doubled in the loop and then multiplied by a further factor of four in the ring, by interleaving bunches in transverse RF deflectors. The beam was then sent into the CLIC experimental area (CLEX) where it was decelerated to extract from it RF power at 12 GHz. Such power was used to accelerate a probe beam, delivered by a 200 MeV injector (Concept d'Accèlèrateur Linéaire pour Faisceaux d'Electrons Sondes, CALIFES) located in the same area.

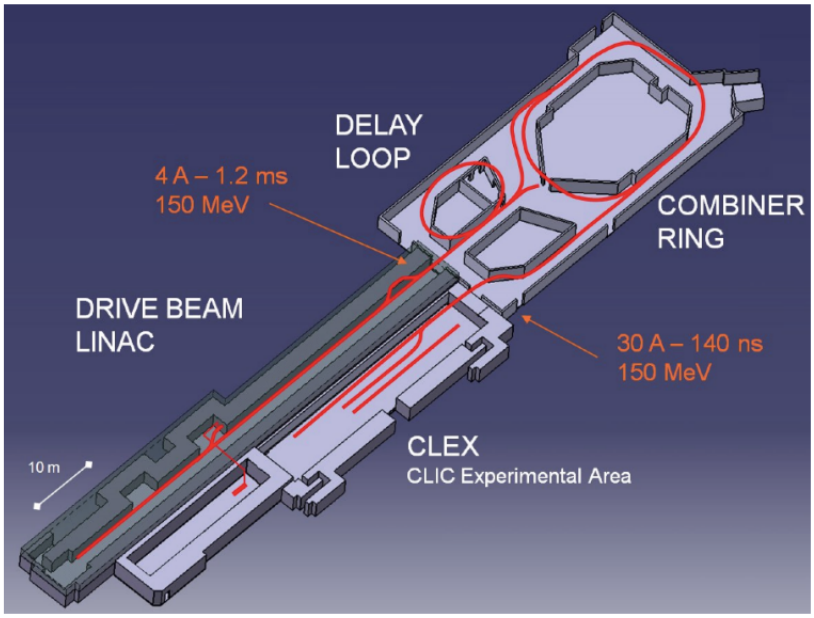

Figure 1.19: Schematic CTF3 layout (Figure taken from [16]).

The main issues explored in CTF3 can be divided in two main areas: Drive-Beam generation and RF power production and Two-Beam acceleration. The Drive-Beam generation is an efficient generation of a high-current electron beam with the proper time structure to generate 12 GHz RF power. In order to achieve this, CLIC relies on a novel technique: fully-loaded acceleration in normal conducting travelling wave structures followed by beam current and bunch frequency multiplication in a series of delay lines and rings by injection with RF deflectors. CTF3 used such method to produce a 28 A electron beam with 12 GHz bunch repetition frequency. The Drive Beam was then sent to the experimental area, CLEX. Concerning the RF power production and Two-Beam acceleration, in CLIC the needed 12 GHz RF power is obtained by decelerating the high current Drive Beam in special resonant structures called PETS (Power Extraction and Transfer Structures). The power is then transferred to high gradient accelerating structures, operated at about 100 MV/m. In the CTF3 experimental area (CLEX), the Drive Beam is decelerated in a string of PETS in the Test Beam Line, (TBL). The Drive Beam can alternatively be sent to another beam line (Two Beam Test Stand, TBTS, renamed later to Test Beam Module, TBM) where one or more PETS powered one or more structures, further accelerating a 200 MeV electron beam provided by CALIFES.

CTF3 was installed and commissioned in stages starting from 2003. The beam parameters have been scaled with respect to the CLIC design [39]. The beam commissioning of the DL was completed in 2006. The CR and the connecting transfer line were installed and put into operation in 2007, while the transfer line to CLEX was installed in 2008. In 2009 this last beam line and the CLEX beam lines, including the CALIFES injector, were

commissioned. During the autumn of 2009, recombination with the DL and CR together was achieved, yielding up to 28 A of beam current. In 2010 the nominal power production from the PETS was obtained, and the first Two-Beam test was performed, reaching a measured gradient of 100 MV/m. In 2011 a gradient of 145 MV/m was reached and the PETS On-off mechanism was successfully tested. At the end of 2014 the TBTS was replaced by the Two-Beam Module, TBM, a 2 m long fully representative unit of the CLIC Main Linac. In 2015 the Drive Beam was decelerated by 50% of its initial energy in the TBL. Drive Beam stability and the overall performances of the facility were continually improved after the initial commissioning, until the final run in 2016. CTF3 successfully completed its experimental program in December 2016 as planned, and stopped operation [16].

Nowadays, this facility has been converted in CLEAR (the CERN Linear Electron Accelerator for Research). The latter cover X-band studies for linear accelerators and also novel concepts as plasma and THz acceleration.

1.3.2 ATF2

The Accelerator Test Facility (ATF) [40] is an accelerator at the High Energy Accelerator Research Organisation (KEK) in Tsukuba, Japan. The ATF is designed as an R&D platform for future linear colliders. The beam operation started in 1997 and the original goal of the facility was to achieve the extremely low vertical beam or emittance required for linear accelerators. The design emittance was achieved in 2001 [41, 42]. The ATF accelerator facility is composed of a photocathode giving electrons to a linac accelerating the particles to 1.3 GeV followed by a DR (see Figure 1.20).

In 2008 the facility was upgraded to the ATF2 project [44]. The existing machine was extended with a 100 m beam delivery system consisting of an extraction line and FFS line, see Figure 1.21. It is a scaled down implementation of the linear collider BDS, which serves for demonstrating the feasibility of FFS for ILC [30] and CLIC. The goals of the ATF2 project can be summarized in:

- **Goal 1**: Optics design validation of the FFS local chromaticity correction scheme and achievement of a vertical beam size at the IP of 37 nm [45] and to establish a beam tuning method for linear collider FFS [46, 47],
- **Goal 2**: Nanometer beam stabilization including hardware and beam handling technologies development [44].

More detail on the beamline description can be found in Section 5.1. The chromaticity of the ATF2 beam line is designed to be comparable to the ILC FFS with a resulting design IP vertical beam size of 37 nm (see Table 1.3). In 2016, the vertical beam size was focused to about 41 nm at the bunch population of 0.7×10^9 at the IP using a reduced aberration optics referred to as $10\beta_x^* \times 1\beta_y^*$ because of the 10 times larger than design β_x^* [28]. In Figure 1.22 the history of all the beam intensity measured at ATF2 from June 2016 to

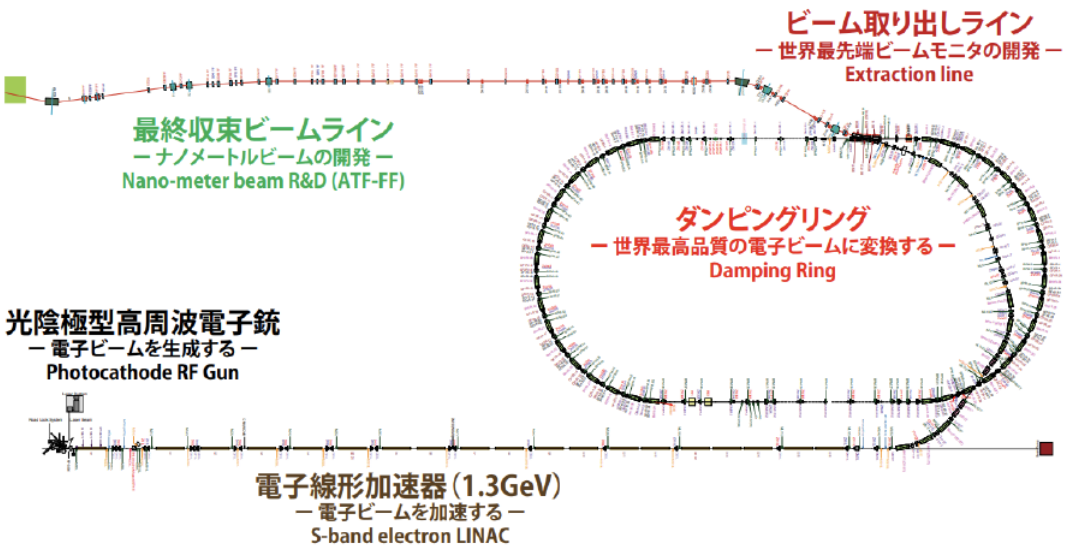

Figure 1.20: Schematic layout of the Accelerator Test Facility [28].

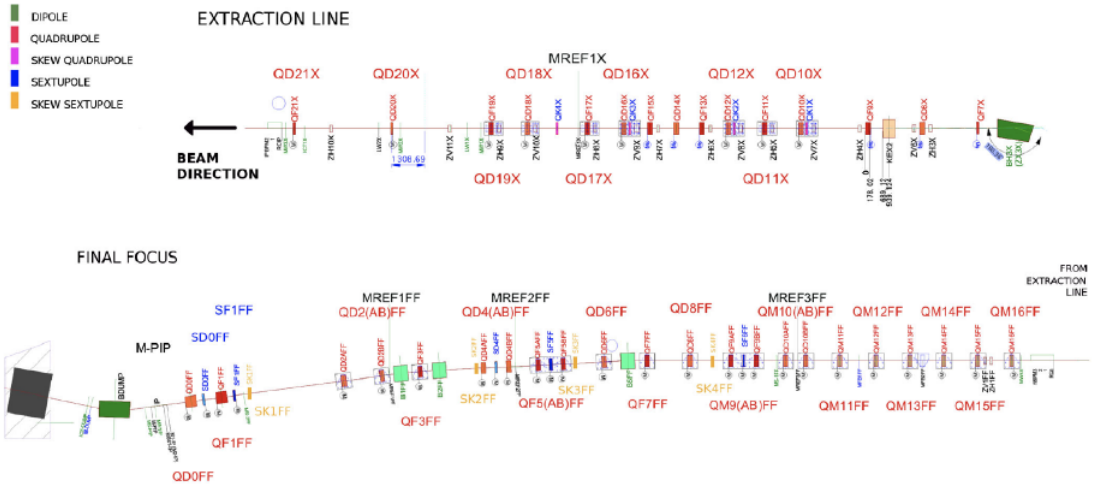

Figure 1.21: Scheme of the ATF2. The beam line on the left represents the extraction beam line (EXT). The beam line on the right represents the FFS as the continuation of the EXT line (Figure taken from [43]).

April 2019 is shown, while in Figure 1.23 the history of all the vertical IP beam size measured at ATF2 from 2012 to 2020 is shown.

CLIC FFS tuning feasibility study is also being carried out at ATF2. The aim is to demonstrate the small beam tuning feasibility at the CLIC chromaticity level, expected to

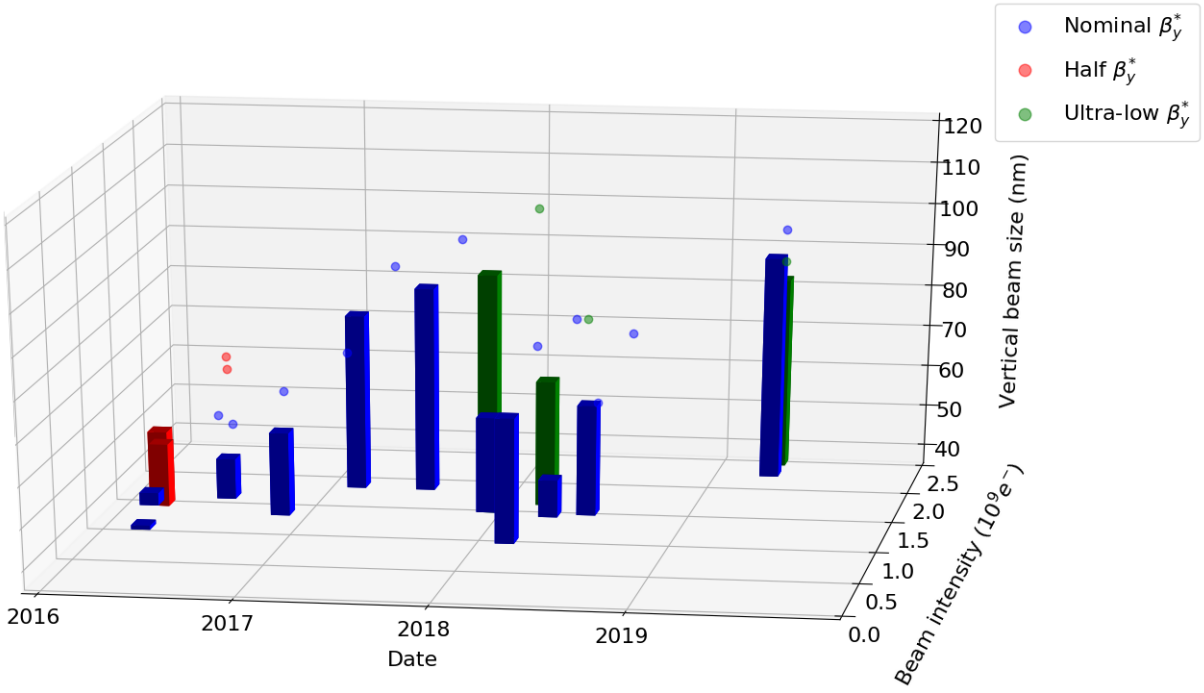

Figure 1.22: History of the measured beam intensity at ATF2 from June 2016 to April 2019.

be 5 times larger than ILC. The chromaticity approximately scales as $\xi_y \approx \frac{L^*}{\beta_y^*}$ and therefore β_y^* is decreased by a factor 4 in order to bring the chromaticity close CLIC as shown in Table 1.3. The ideal optics used for CLIC study is referred as ultra-low β_y^* optics or $1\beta_x^* \times 0.25\beta_y^*$ optics. The design beam size achievable with the ultra-low β_y^* optics is limited to 29 nm due mainly to amplified higher order aberrations and magnetic imperfections such as multipolar errors. However the beam size can be reduced in design to 20 nm if a pair of octupoles is introduce in the FFS [28]. This pair of octupoles have been designed at CERN and installed in ATF2 beamline in 2017 [49]. Optics optimization, tuning simulations and experimental results on the ultra-low β_y^* optics study at ATF2 using octupoles are detailed in Chapter 5.

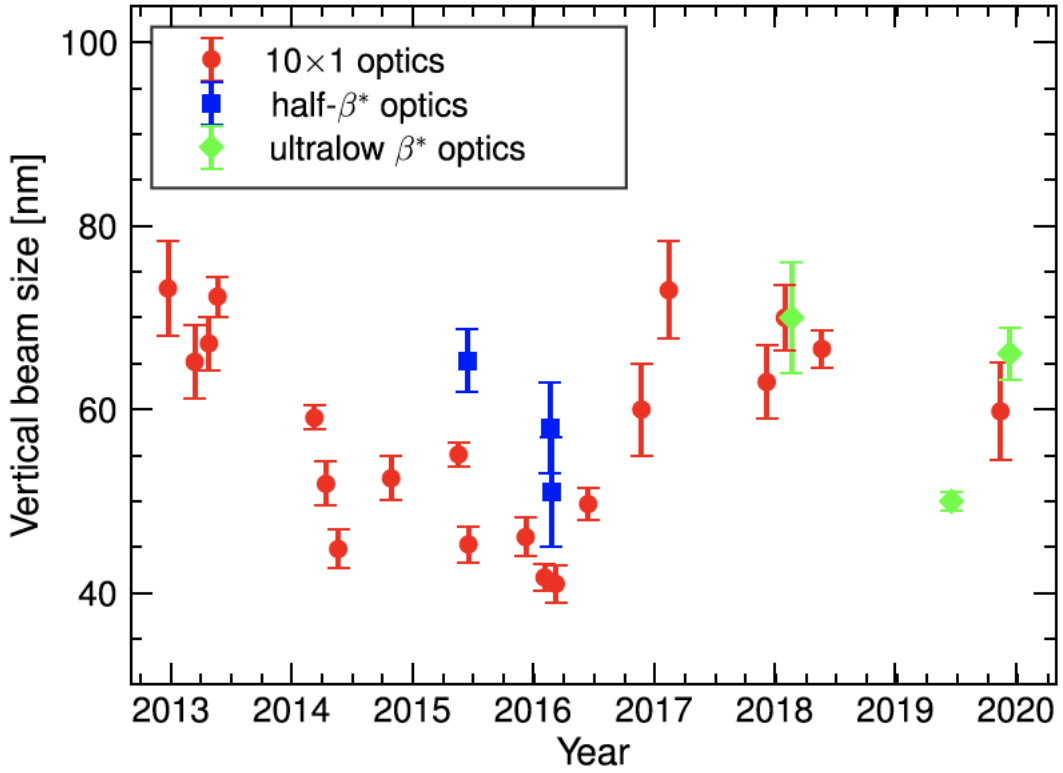

Figure 1.23: History of the measured σ_y^* obtained in every operation period at ATF2 from 2012 to 2020 (Figure taken from [48]).

Table 1.3: Beam and optics parameters for ILC, CLIC, ATF2 FFS.

	ILC	**CLIC**	**ATF2 nominal β_y^*** ($10\beta_x^*$ x $1\beta_y^*$)	**ATF2 half β_y^*** ($10\beta_x^*$ x $0.5\beta_y^*$)	**ATF2 ultra-low β_y^*** ($25\beta_x^*$ x $0.25\beta_y^*$)
E [GeV]	250	380	1.3	1.3	1.3
L^* [m]	4.1	6	1	1	1
$\varepsilon_{y,design}$ [pm]	0.08	0.003	12	12	12
β_x^* [mm]	11	8	40	80	100
β_y^* [mm]	0.41	0.1	0.1	0.05	0.025
σ_x^*[μm]	0.47	0.149	8.9	8.9	12.6
σ_y^*[nm]	5.9	2.9	37	26[a]	20[a]
$\sigma_{y,meas.}^*$ [nm]	-	-	41±3	58±5	64±3
$\xi_y \approx L^*/\beta_y^*$	10000	50000	10000	20000	40000

[a] Optimized with octupoles.

CHAPTER 2

Optics Design of the Novel CLIC Dual BDS for two IRs at 380 GeV and 3 TeV

CLIC current baseline design includes only one IR and one BDS. In [20, 28] the baseline designs for both CLIC 380 GeV and 3 TeV have been optimized including moving the final quadrupole (QD0) outside the detector in order to increase the distance between QD0 and the IP, L*, to 6 m. The L*= 6 m design is considered as the starting point for the development of the model for the novel dual CLIC BDS.

In this chapter at first the main subsystems of the previous and the current designs of the CLIC BDS with one IR are described for both energy stages of CLIC. Secondly, the development of the model to construct the optics design of the novel CLIC dual BDS for two IRs is described for both energy stages of CLIC.

2.1 The current CLIC BDS with one IR

The current CLIC BDS has evolved from the CDR, in particular the L* parameter has been varied in order to alleviate engineering and stabilization issues hence increasing L* and moving QD0 from the detector to the tunnel was proposed as a fallback solution. To do that, a collection of FF systems with L* values between 3.5 m and 8 m have been studied for CLIC. The shortest L* that would have make possible to have QD0 outside from the detector was 6 m. This option also met the CLIC requirements with a tight margin of 5% for imperfections [15, 50]. In fact, in the CDR configuration foresaw a L*= 3.5 m for CLIC 3 TeV and L*= 4.3 m for CLIC 380 GeV, while the BDS current baseline foresees an L* of 6 metres, for both CLIC energy stages, with final quadrupoles mounted outside the detector volume [16], directly on the tunnel floor. The length of the entire BDS is $\approx$ 1950 m for CLIC 380 GeV and is $\approx$ 3120 m for CLIC 3 TeV. In order to allow the energy upgrade inside the CLIC tunnel, the end of the 380 GeV and 3 TeV BDS beamlines have been matched such that the axis along which the ML is located is

unchanged by the upgrade. The crossing angle (c.a) for the CLIC 3 TeV BDS is 20 mrad for both the CDR baseline design and the current one, while the required crossing angle for the CLIC 380 GeV BDS changed from 18.3 mrad in CDR BDS to 16.5 mrad for the L*= 6 m BDS. Figure 2.1 shows the CLIC BDS layouts, while Table 2.1 summarizes the design parameters of CLIC designs, for both energies options and both L* options for the CDR and the current designs.

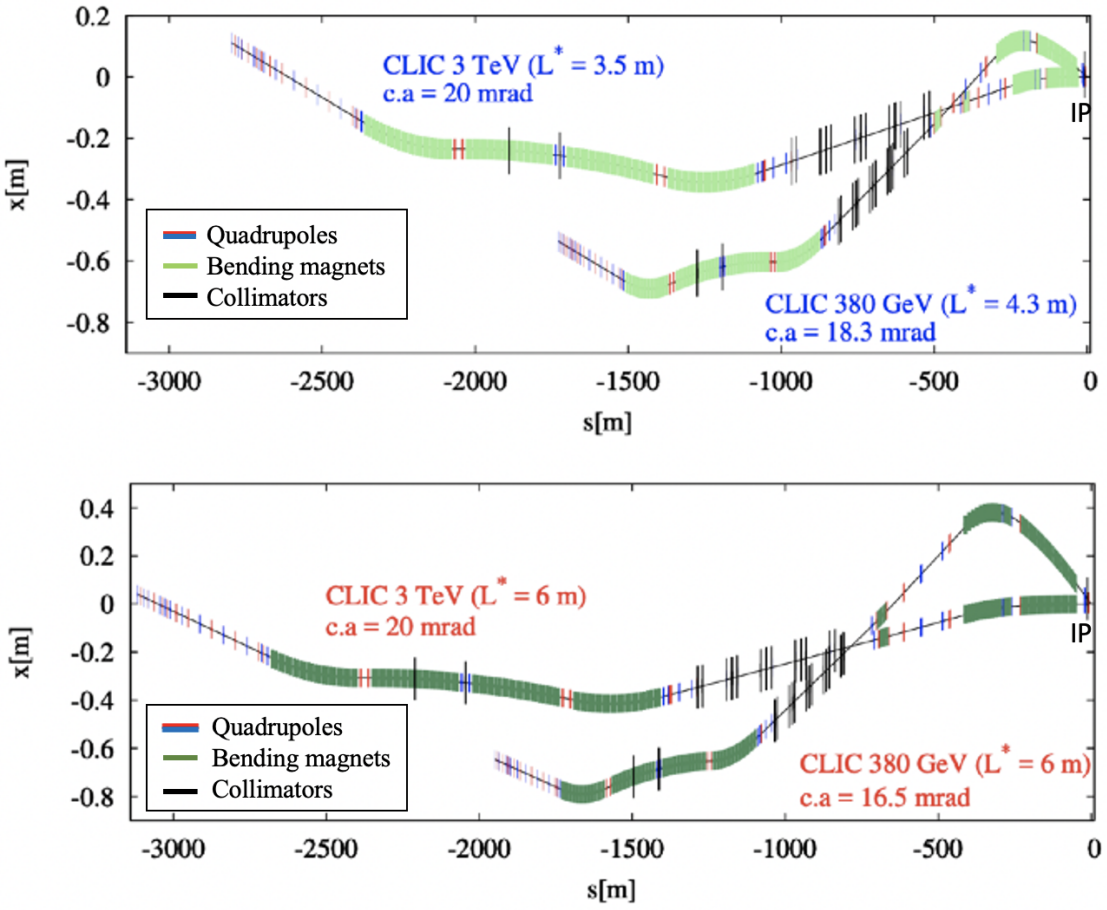

Figure 2.1: BDS Layout of CLIC designs. Top: CDR with L*= 4.3 m for CLIC 380 GeV and L*= 3.5 m for CLIC 3 TeV. Bottom: Current with L*= 6 m for both energy cases.

The BDS transports the e^+ and e^- beams from the exit of the linacs to the IP by performing the critical functions required to meet the CLIC luminosity goals (σ_x= 40 nm and σ_y= 1 nm) [51] and bringing them into collision. In addition, the BDS performs several critical functions. Firstly, it measure the linac beam and match it into the FFS. Secondly, it protect the beamline and detector against mis-steered beams from the MLs. Thirdly, it remove any large amplitude or off-energy particles (beam-halo) from the linac to minimize background in the detectors. Fourthly, it measure and monitor the key physics parameters such as energy and polarization.

Table 2.1: CLIC BDS design parameters for the CDR with L*= 4.3 and 3.5 m and for the current with L*= 6 m for both energy stages.

CLIC	**380 GeV**		**3 TeV**	
	CDR	**Current**	**CDR**	**Current**
L* [m]	4.3	6	3.5	6
BDS length [m]	1728	1949	2795	3117
Norm. emittance $\gamma\varepsilon_x$ [nm]	950	950	660	660
Norm. emittance $\gamma\varepsilon_y$ [nm]	30	30	20	20
Beta function (IP) β_x^* [mm]	8	8	7	7
Beta function (IP) β_y^* [mm]	0.1	0.1	0.068	0.12
IP beam size σ_x^*[nm]	144	144	40	40
IP beam size σ_y^*[nm]	2.9	2.9	0.7	0.9
Bunch length $\sigma_z[\mu\text{m}]$	70	70	44	44
rms energy spread $\delta_p[\%]$	0.3	0.3	0.3	0.3
Bunch population N_e [10^9]	5.2	5.2	3.72	3.72
Number of bunches n_b	352	352	312	312
Repetition rate f_{rep} [Hz]	50	50	50	50
Crossing Angle [mrad]	18.3	16.5	20	20
Luminosity $\mathscr{L}_{TOT}$ [$10^{34}\,\text{cm}^{-2}\text{s}^{-1}$]	1.5	1.5	5.9	5.9

The second and the third functions are accomplished by the collimators. Therefore, the first collimator needs to survive the impact of any mis-steered CLIC bunch train. This condition requires large beam sizes at the first collimator, and drives the length of the system. The BDS provides sufficient instrumentation, diagnostics and feedback systems to achieve these goals. The optical functions and layout of the entire BDS is shown in Figure 2.2 for CLIC 380 GeV case and in Figure 2.3 for CLIC 3 TeV case. The baseline current layout foresees a single collision point with a 16.5 mrad crossing angle for CLIC 380 GeV and 20 mrad crossing angle for CLIC 3 TeV [15]. This BDS structure is the starting point for the construction of the novel dual BDS layout for two IRs.

2.1.1 The Diagnostics Section

The initial part of the BDS, from the end of the ML to the start of the collimation system, is where the properties of the beam are measured and corrected before it enters the collimation and FFS. The optics and the layout of the DS is shown in Figure 2.4 for the CLIC 380 GeV case and in Figure 2.5 for the CLIC 3 TeV case. Starting at the exit of the ML, the system includes a skew correction section, emittance diagnostic section and beta matching section. The skew correction section contains 4 orthonormal skew quadrupoles which provide complete and independent control of the 4 betatron coupling parameters. This layout allows correction of any arbitrary linearized coupled beam.

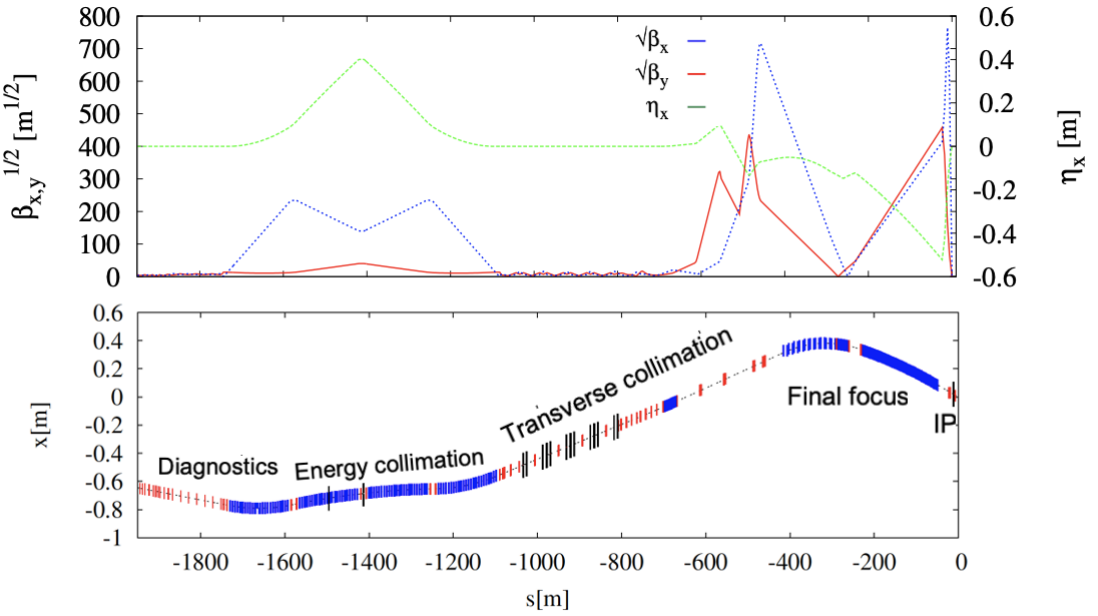

Figure 2.2: Optics (top) and layout (bottom) of the CLIC 380 GeV current BDS with L*= 6 m.

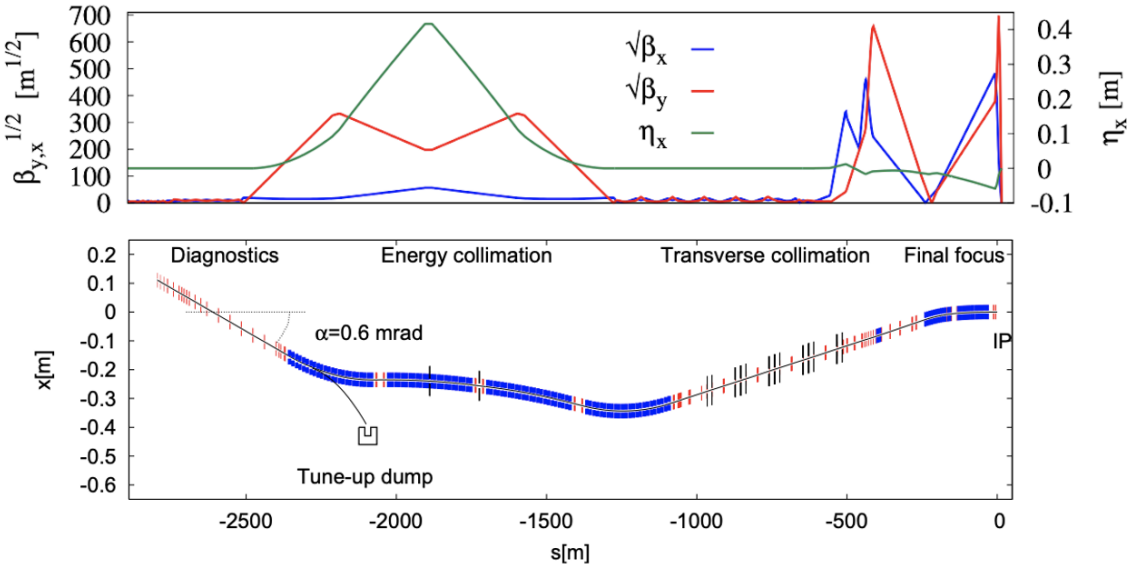

Figure 2.3: Optics (top) and layout (bottom) of the CLIC 3 TeV current BDS with L*= 6 m.

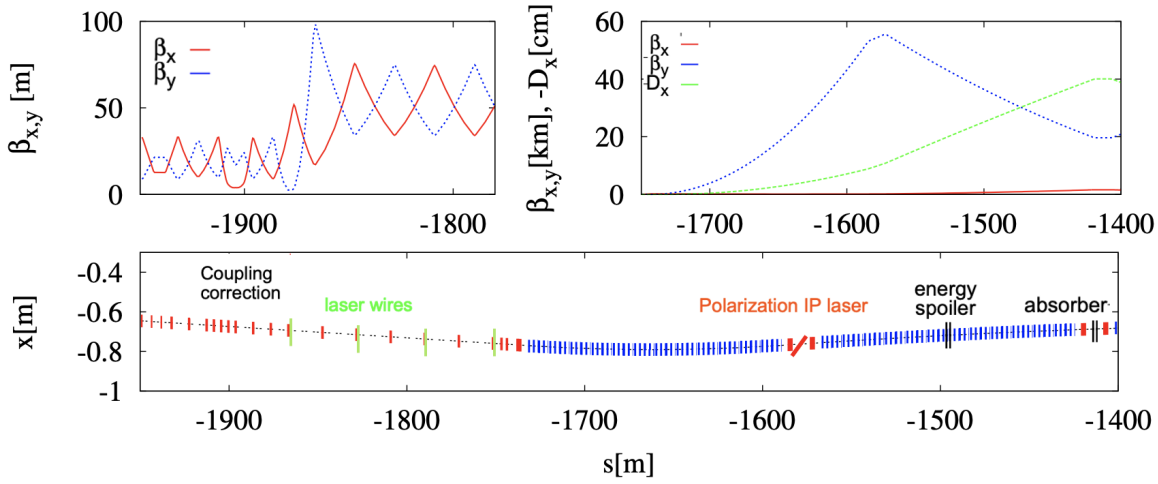

Figure 2.4: Optics (top) and layout (bottom) of the CLIC 380 GeV current DS and energy collimation sections.

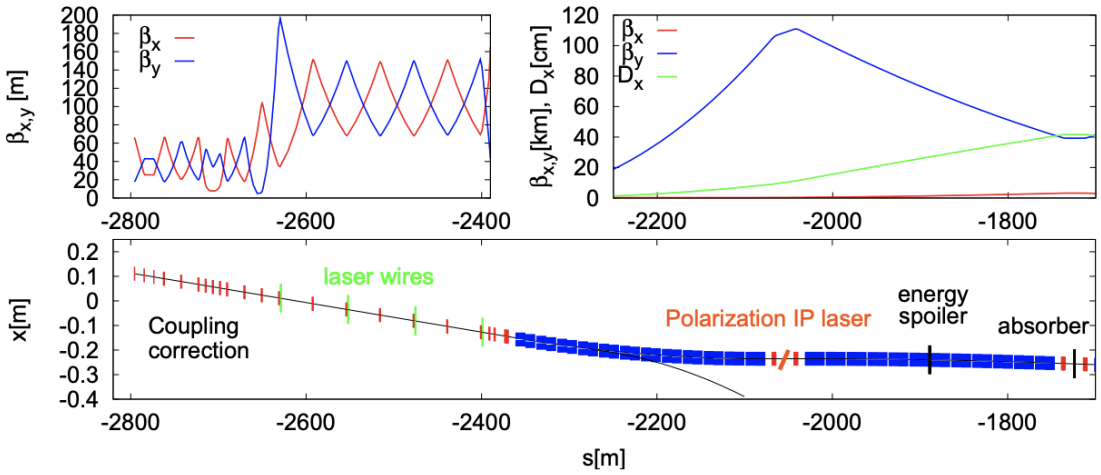

Figure 2.5: Optics (top) and layout (bottom) of the CLIC 3 TeV current DS and energy collimation sections.

The emittance DS contains four laser wires which are capable of measuring horizontal and vertical r.m.s. beam sizes down to 1 μm. The wire scanners are separated by 45° in betatron phase to allow a complete measurement of the 2D transverse phase space and determination of the projected horizontal and vertical emittances [15].

The energy measurement has been designed to minimize the required space due to the tight constraints on the CLIC total length. The deflection of the first dipole in the energy collimation section together with high precision BPM pairs before and after the dipole provides the most compact energy measurement. The integrated magnetic field is

assumed to have a calibration error of 0.01% and the BPM resolution must be 100 nm or better. This setup provides a relative energy resolution better than 0.04%. Reference trajectories are regularly established by zeroing the magnetic field and safely disposing of the beam in the tuneup dump.

The BDS has a polarization measurement station integrated into the energy collimation section. Figures 2.4 and 2.5 show the location of the polarization laser IP. At this location, the beam travels parallel to the beam direction at the e^-e^+ IP and there is enough free space for the polarization laser. The backscattered electrons (or positrons) deviate from the main beam trajectory in the bending dipoles. These lower energy particles are collected in a detector right before the energy spoiler. Particles losing about 95% of the energy are deflected on the order of 100 mm. With current existing laser technology, the polarization measurement achieves a resolution better than 0.1% when averaging over 60 seconds.

During the commissioning of the MLs, the beam must be dumped before the collimation, FFS, or IR areas. There is an extraction line before the energy collimation where the beam can be diverted to a water-filled dump capable of absorbing the full beam power. This section is called tune-up extraction line and dumps.

2.1.2 The Collimation Section

The CLIC collimation section has two critical functions: it protects the downstream beamline and detector against mis-steered beams from the ML and it removes the beam halo. The most likely scenario for having mis-steered beams in the BDS is the failure of some component of the accelerating RF in the 20 km linac, resulting in a lower beam energy. Therefore, placing the energy collimation before the betatron collimation guarantees the most efficient absorption of the errant beams. The layout of the energy collimation can be found in Figure 2.4 for CLIC 380 GeV and in Figure 2.5 for CLIC 3 TeV. The energy spoiler is designed to survive the impact of a full bunch train, however, recent simulations indicate that a solid energy spoiler may be damaged by some impacts. This can be avoided by use of a hollow spoiler that provides the same thickness in radiation length at any impact parameter. This requires further investigation during the technical phase, particularly a detailed study of failure scenarios.

The transverse collimators, made of Ti, are sacrificial or consumable. A collimator absorber is placed downstream of the spoiler as shown in Figure 2.6 for CLIC 380 GeV case and in Figure 2.7 for CLIC 3 TeV case to stop the particles scattered at the spoiler.

Particles in the beam halo produce backgrounds in the detector and must be removed in the BDS collimation system. One of the design requirements for the CLIC BDS is that no particles are lost in the last several hundred metres of beamline before the IP. Another requirement is that all SR passes cleanly through the IP to the extraction line. The BDS collimation must remove any particles in the beam halo which do not satisfy these criteria. These requirements define a system where the collimators have very narrow gaps and the system is designed to address the resulting machine protection, survivability and beam

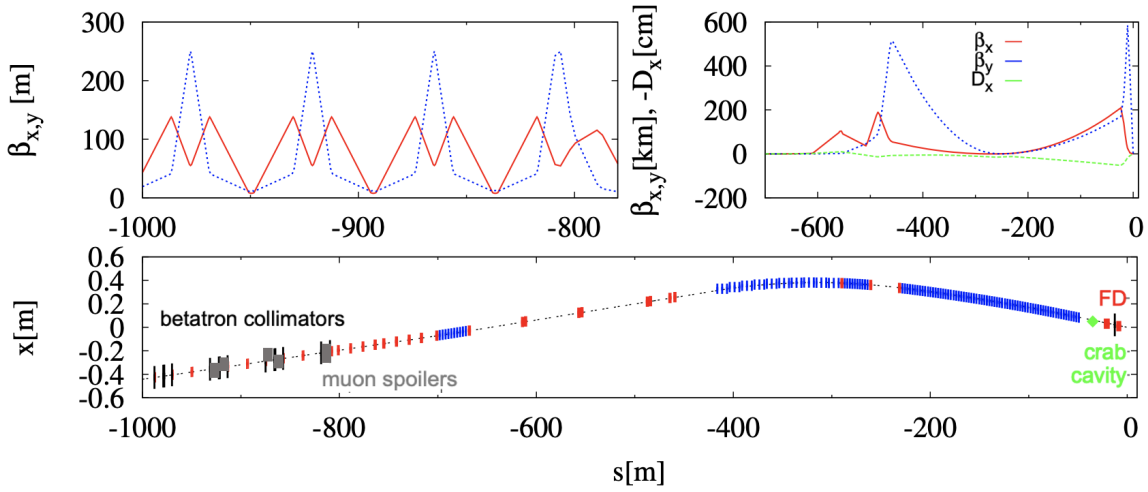

Figure 2.6: Optics (top) and layout (bottom) of the CLIC 380 GeV current betatron collimation and FFS.

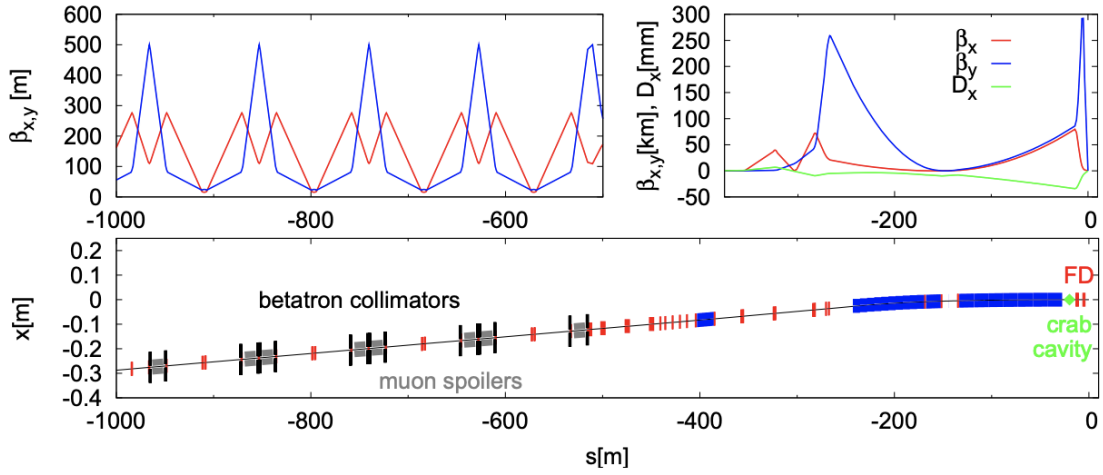

Figure 2.7: Optics (top) and layout (bottom) of the CLIC 3 TeV current betatron collimation and FFS.

emittance dilution issues. The betatron collimation system has four spoiler/absorber x/y pairs located as displayed in Figures 2.6 and 2.7 providing collimation at each of the FD and IP betatron phases. All spoilers and absorbers have adjustable gaps. The layout and the optical functions of the betatron collimation can be found in Figures 2.6 and 2.7.

The actual distribution of halo particles in a realistic machine with imperfections could be much larger than simulated by beam-gas scattering for the ideal machine. For more conservative estimates, the collimation system would be hit by a fraction of 10^{-3} of the

beam particles resulting in one to two orders of magnitude higher muon rates than desirable. One possibility to reduce the muon flux into the detector region is to use cylindrical magnetized iron shielding with an outer radius of 55 cm around the beampipe located about 100 m downstream of the spoilers. A factor of ten reduction of the muon flux would require 80 m long shielding. Space must be reserved in the BDS for the muon shielding as shown in Figures 2.6 and 2.7. The muon shielding could be installed in stages, as required by the actual beam conditions.

2.1.3 The Final Focus System

The strong focusing required to achieve the nanometer level beam size at the IP for CLIC is driven by the two last quadrupoles, referred to as FD. The FFS forms an almost parallel beam at the entrance of the FD of several hundreds of nanometers which is then demagnified down to few nanometers at the IP. The layout of the FFS can be found in Figure 2.6 for the CLIC 380 GeV case and in Figure 2.7 for the CLIC 3 TeV case, while the Twiss functions for both energy stage cases can be found in Figure 2.8.

The beam coming from the ML is not fully monochromatic and even a minor energy spread of a fraction of percent ($\approx$ 0.3 % for CLIC), will focalize particles with different energies at different points causing large dilution of the beam size at the IP. The chromaticity is amplified by the focusing strength of the FD and by the length of the focal distance between QD0 and the IP, L*. The FFS design is thus driven by the compensation of these chromatic effects mainly generated by the FD. The chromaticity is corrected using sextupoles in dispersive regions and located in a way to cancel the geometrical aberrations. The residual higher order aberrations are further minimized with octupoles and decapoles.

In the case of the CLIC BDS the local chromaticity correction scheme, already demostrated in ATF2, is used.
Given the facts that crossing angles are considered, crab cavities are required to rotate the bunches so they collide head on. They apply a z-dependent horizontal deflection to the bunch that zeroes at the center of the bunch. The crab cavities are located prior to the FD as shown in Figure 2.7 and with 90° degrees phase advance from the IP.

2.2 Novel Dual CLIC BDS for two IRs

Dual BDS designs were already considered for other LCs, the Next Linear Collider (NLC) [52] and the ILC. These designs can be considered as the starting point for the development of the model to construct the novel dual BDS for CLIC, first presented in this thesis work.

In Figure 2.9 the dual BDS layout for NLC [53] can be seen. In this layout the luminosity performance for the two detectors was found to be within 30% up to the energy of 1.3 TeV.

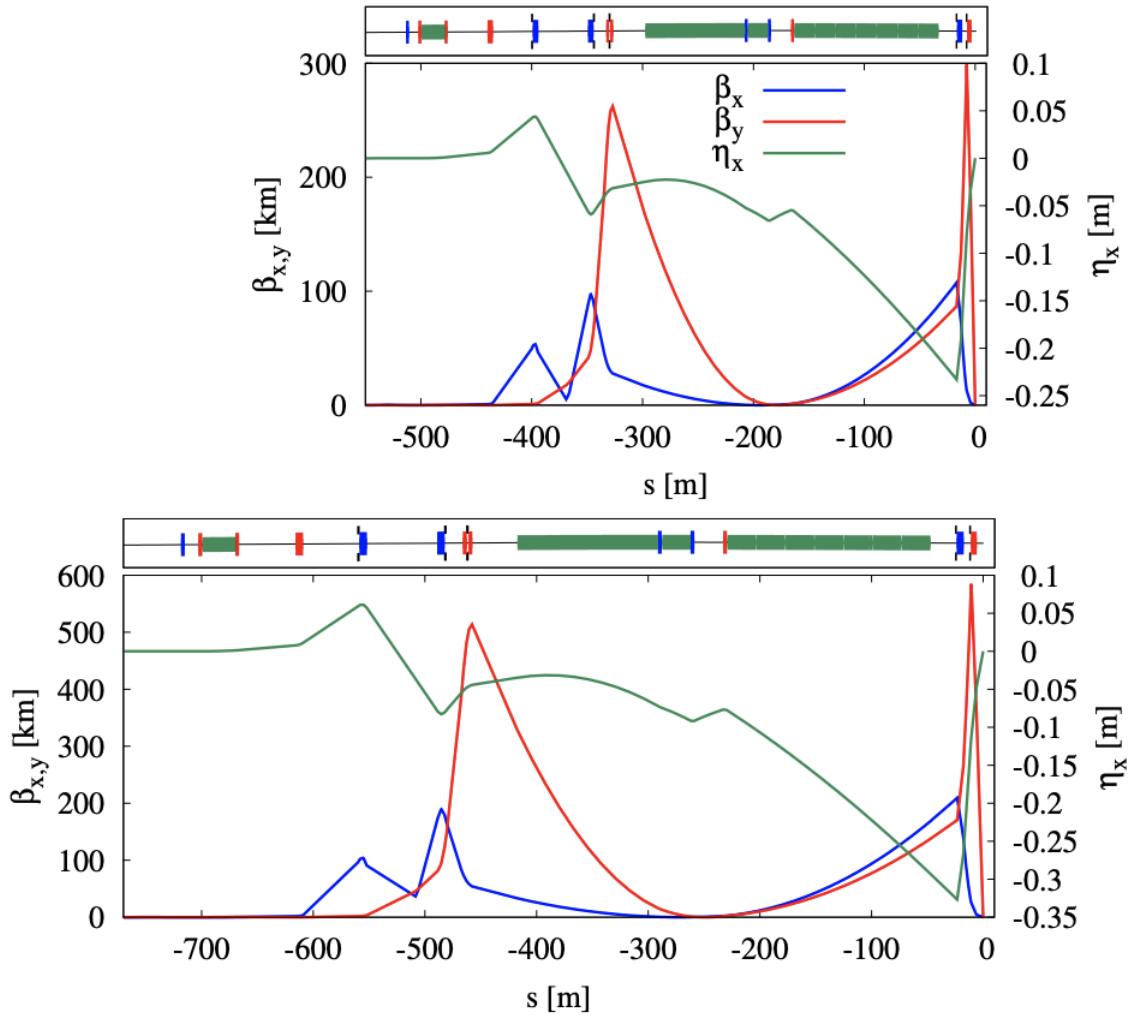

Figure 2.8: Twiss functions in the FFS for CLIC 380 GeV (top) and CLIC 3 TeV (bottom) respectively.

A dual BDS preliminary layout has been proposed also for ILC allowing two distinct IRs with crossing angles of 2 mrad and 20 mrad respectively [54, 55]. Figure 2.10 shows the preliminary ILC dual BDS layout.

This thesis work will present a new design with comparable luminosity imbalance up to an energy of 3 TeV.

The novel optics design of the dual BDS has been made with the code MAD-X [56]. In order to create a second IR area, bending dipoles have been added at the entrance of the DS, to separate the beams at the exit of the ML, trying to minimize the length of the added section. The optics of the DS has been rematched to the rest of the BDS in order to keep its performance. The choice of starting separating the IRs from the DS is mostly to minimize the required dipole field and, hence, the emittance growth from SR. The designs

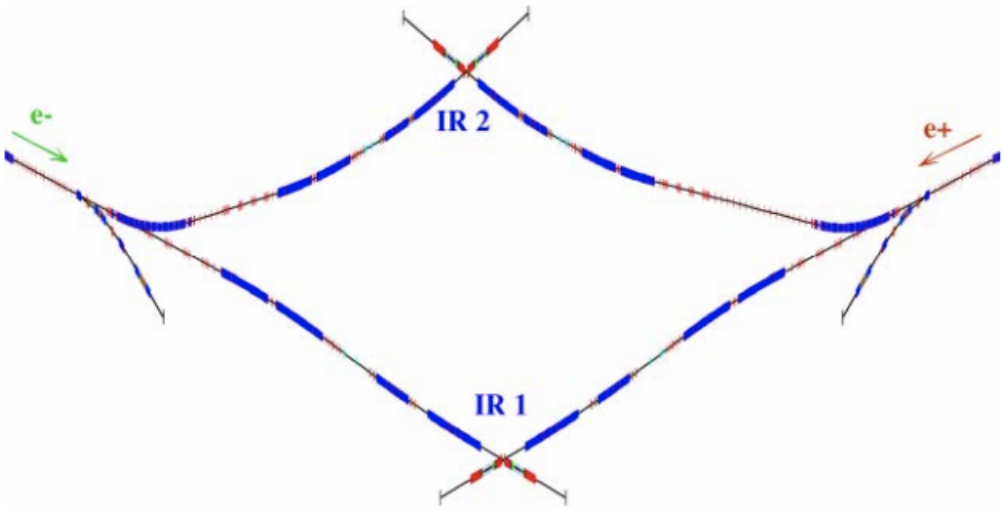

Figure 2.9: Layout of NLC Beam Delivery Systems for two IRs. Anamorphic scale (the transverse direction is stretched about a hundred times). Straight-ahead BDS for the 1^{st} IR and one-way-bending BDS for 2^{nd} IR (Figure taken from [53]).

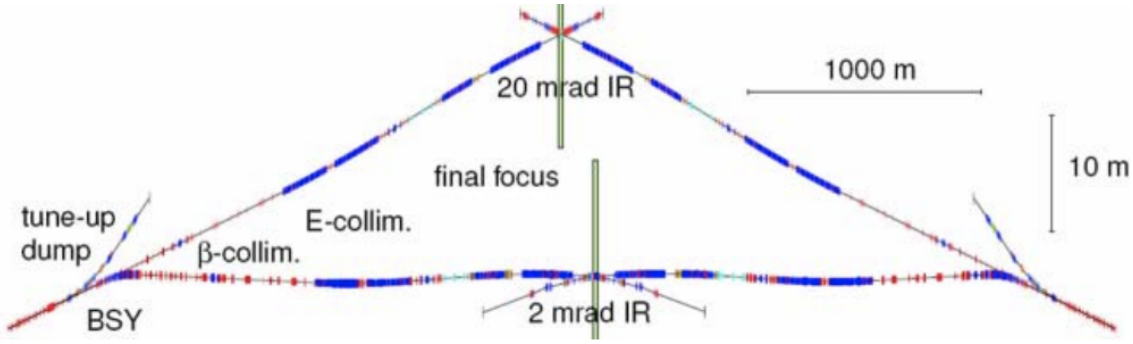

Figure 2.10: Layout of the two IRs and associated BDS sections in the ILC baseline conceptual design (Figure taken from [54]).

are presented in the following sections for both energy stages. In Appendix A the MAD-X code implementation can be found more in detail, in the following instead only the results of the optimization are shown.

2.2.1 Novel dual BDS optics design for CLIC 380 GeV

The novel dual CLIC BDS at 380 GeV has been constructed by adding 8 more FODO cells, of a phase advance, μ, of 45° in the existing DS, with an additional total length of about 300 m. The four BDS systems at either side of the two IPs (BDS1 $e^{\pm}$ and BDS2 $e^{\pm}$) need to have different DS lengths to provide the desired longitudinal and transverse separations at the IP. As can be seen from the two new DS designs, Figures 2.11 and 2.12

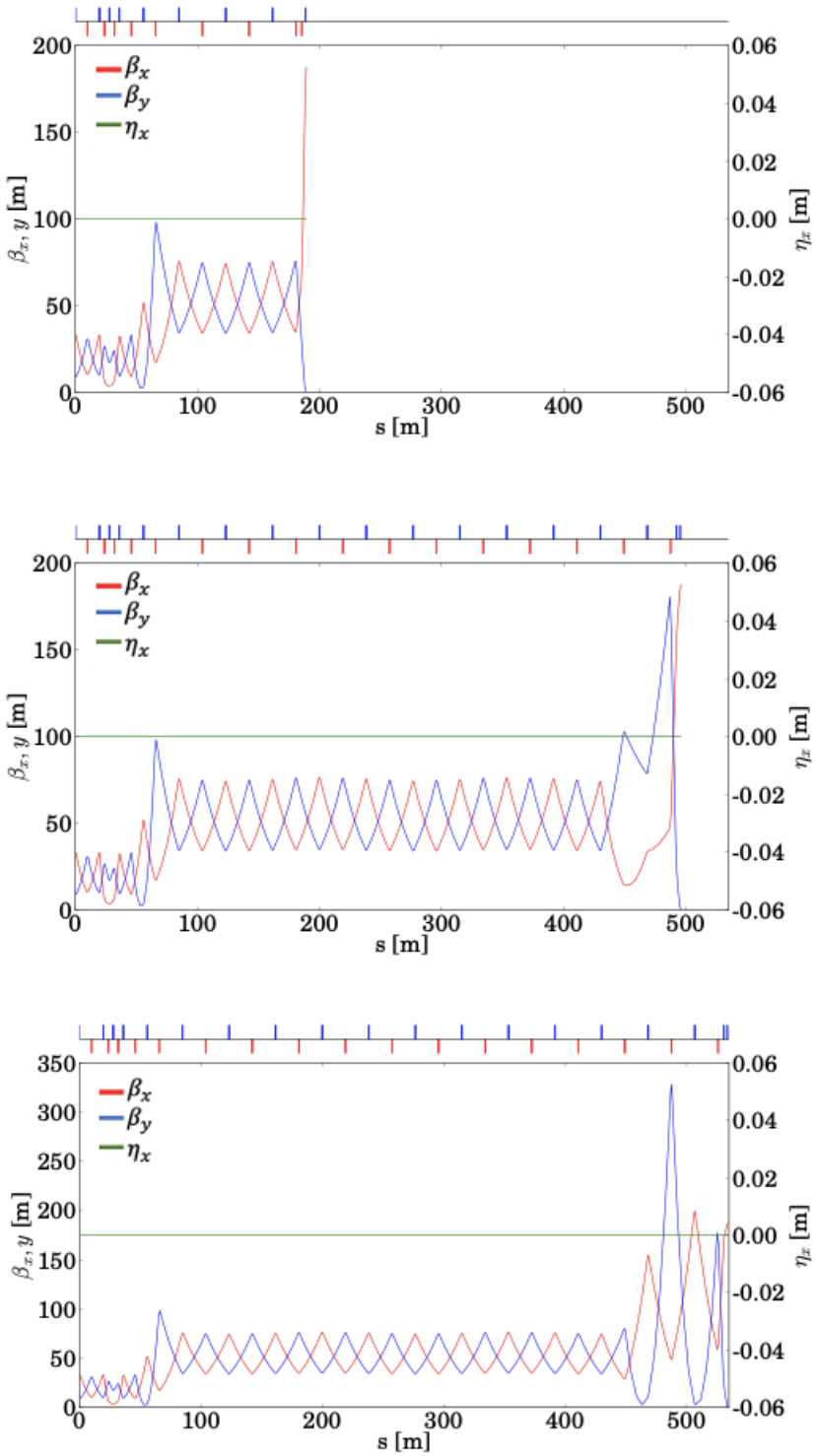

Figure 2.11: Top: DS of CLIC 380 GeV for the single IR. Middle: New DS for the dual IRs in the case of BDS1 e^+. Bottom: New DS for the dual IRs in the case of the BDS1 e^-.

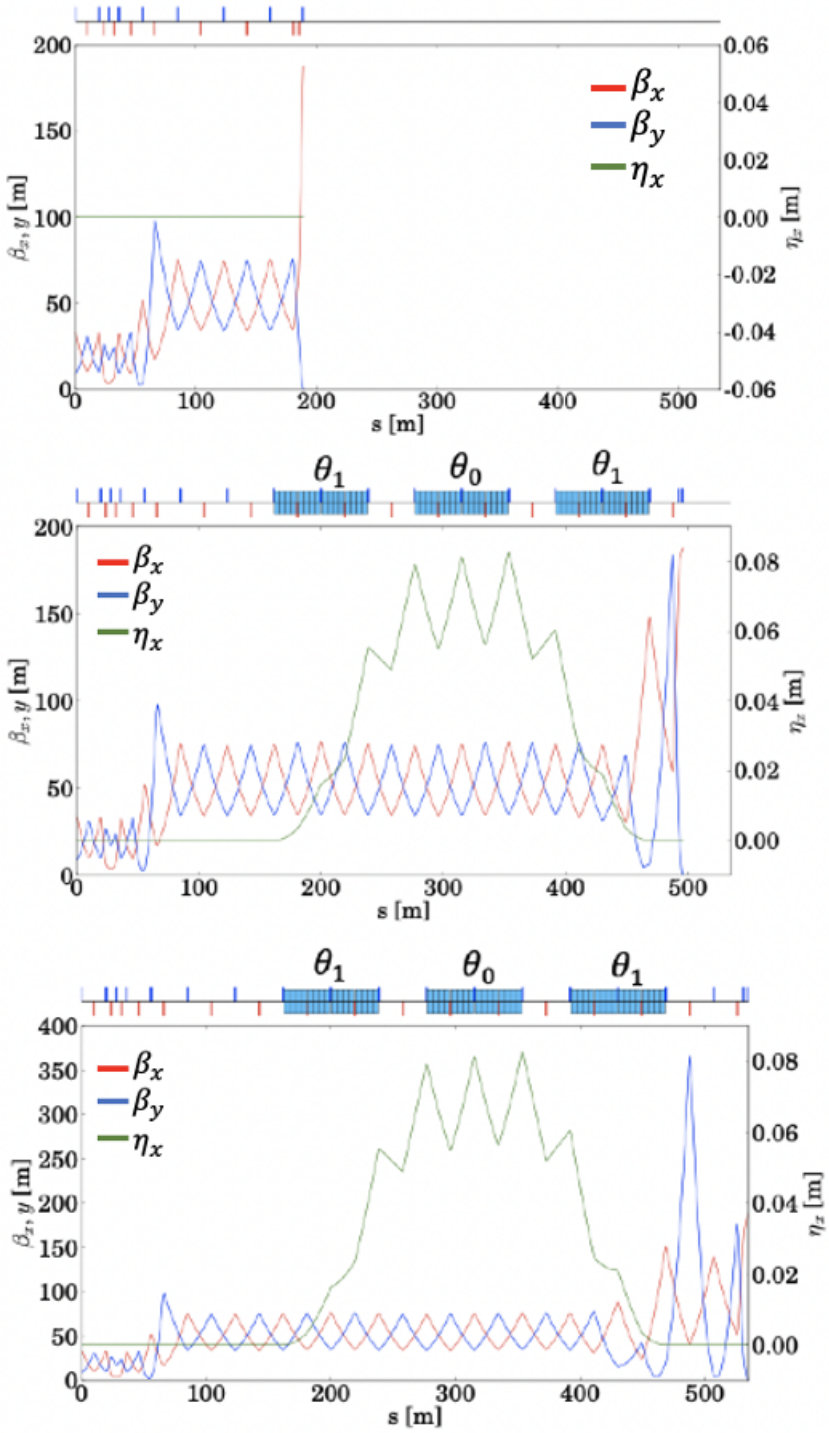

Figure 2.12: Top: DS of CLIC 380 GeV for the single IR. Middle: New DS for the dual IRs in the case of BDS2 e^-. Bottom: New DS for the dual IRs in the case of the BDS2 e^+.

BDS1 is just longer in respect to the current baseline design while in the BDS2 the bending magnets have been added in order to have the separation of the two beams at the IRs. Figures 2.11 and 2.12 show the Twiss functions, β_x, β_y and η_x as function of the longitudinal position along the DS for the BDS1 $^{\pm}$ and BDS2 $^{\pm}$. In particular, in Figures 2.11 and 2.12 it is possible to see the optics structure of the DS before that is the current BDS (the first figure on the top) and in the other two plots the new design for the dual BDS: the middle one, shows the case of the shorter BDS (in Figure 2.11 BDS1 e^+ and in Figure 2.12 BDS2 e^-), while the bottom one shows the case of the longer BDS (in Figure 2.11 BDS1 e^- and in Figure 2.12 BDS2 e^+). On the top of each figure there are the magnets appearing in the DS: in blue the focusing quadrupoles, in red the defocusing ones and in light blue the dipoles (only for the BDS2e $^{\pm}$ cases).

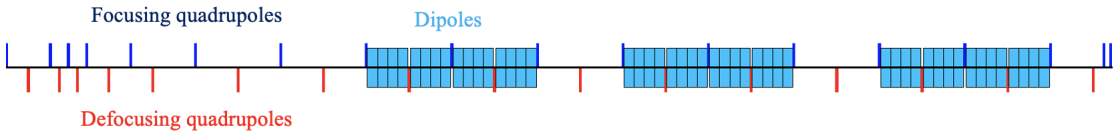

Figure 2.13: Zoom on the magnets layout of the BDS2 $e^{\pm}$ DS for the CLIC 380 GeV.

In Figure 2.12 is shown the BDS2 $e^{\pm}$ where in the current DS has been added three dipoles, with bending angles θ_1, θ_0 and θ_1 in agreement with the figure, in order to separate the two BDS. In order to have a clearer view on the bending magnets structure, a zoom on the new magnets layout of the DS is shown in Figure 2.13. The three dipoles with bending angles θ_1, θ_0 and θ_1 are given by 4 small dipoles added between the focusing and the defocusing quadrupoles multiplied 4 times. So the three dipoles are given by 16 small dipoles inside the FODO cell structure. The bending angles are arranged to suppress dispersion at the exit of the DS. The strengths of the dipoles are related as $\theta_1 = \theta_0/\sqrt{2}$ [57]. We define as θ the total bending angle, $\theta = 2\theta_1 + \theta_0$. The value $\theta = 4.83$ mrad has been chosen to provide the desired transverse separation of 10 m between the two detectors to fit the experimental cavern, since $\theta * L_{BDS} \approx 10$ m. The Twiss functions at the DS exit have been matched to the design values and then the new DS has been connected to the rest of the BDS in order to get the beam to two different IRs. The layout of the new dual BDS is shown in Figure 2.14 displaying all the magnets along the beamlines. Concerning the longitudinal separation of the two detectors, it was chosen to be about 40 m (that corresponds to one FODO cell in the DS), even if it introduces issues with train synchronization, it is necessary in order to minimize the transverse separation space to allocate the two detectors. The two crossing angles are respectively 16.5 mrad for IR1 and 26 mrad for IR2 (compatible with gamma-gamma collisions).
A zoom of the IRs is shown in Figure 2.15 depicting the different beamlines. IR1 is longitudinally shifted 40 m ahead of IR2 and it is transversely separated by 10 m from IR2 to allow the necessary cavern sizes to allocate the two detectors without any interference between them. Table 2.2 summarizes the geometrical parameters and the optics functions of the novel dual BDS for CLIC 380 GeV.

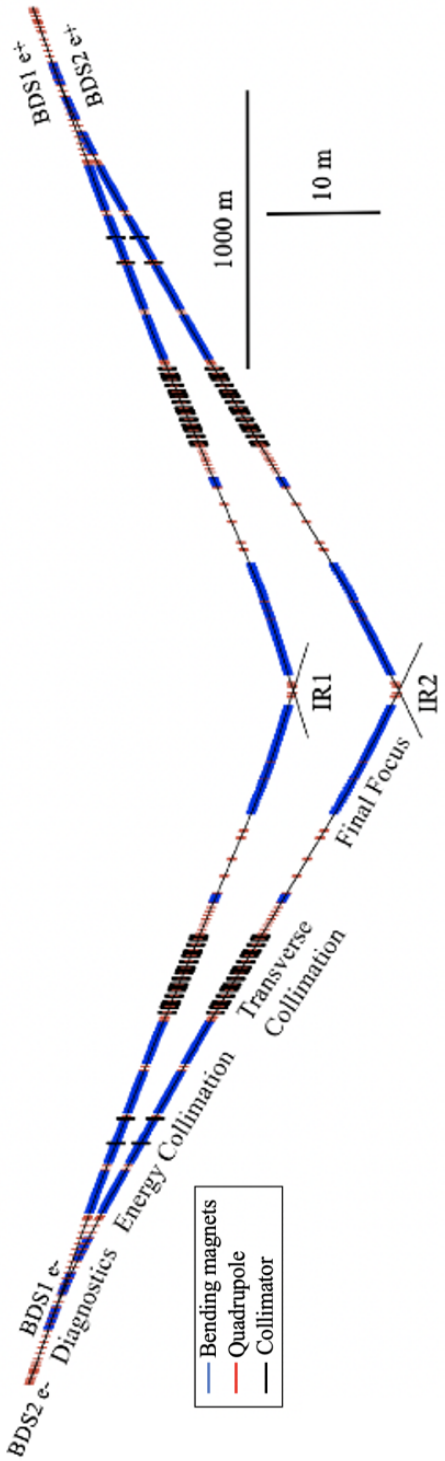

Figure 2.14: Layout of the new dual CLIC 380 GeV BDS System for two IRs.

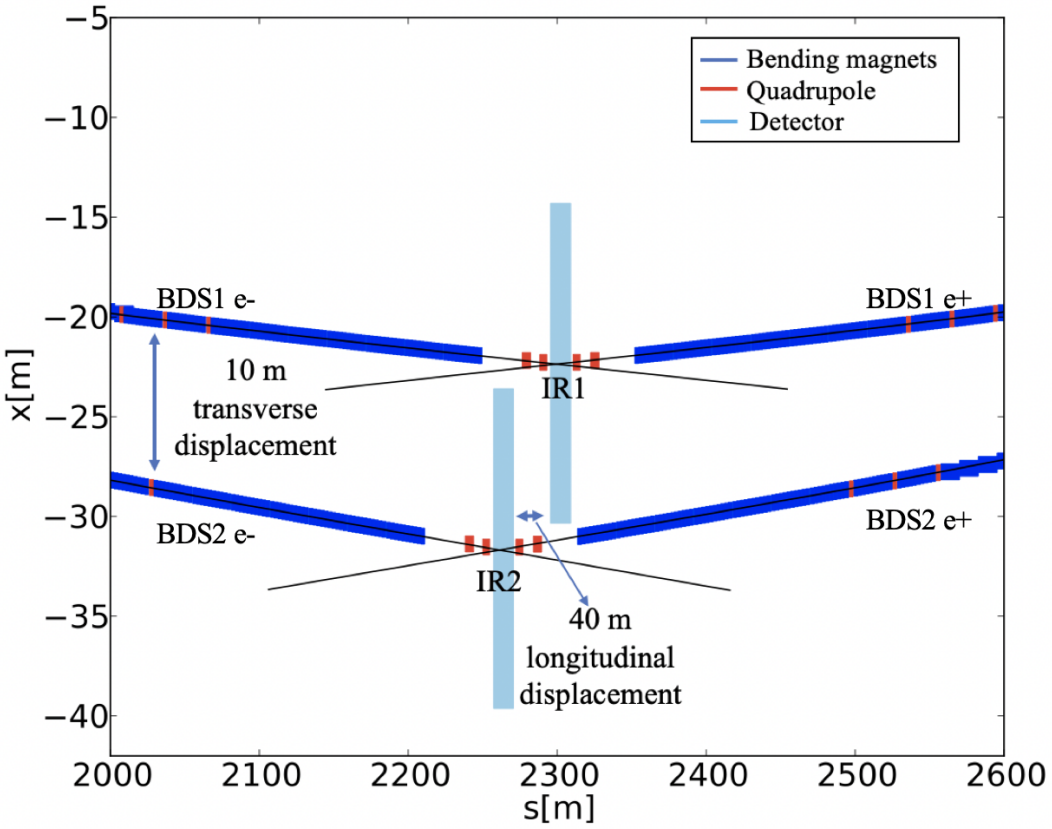

Figure 2.15: Zoom at the IRs to have a clear visualization on the longitudinal and transverse separations between the two detectors of about 40 m and about 10 m, respectively (not in a scale).

Table 2.2: Summary table of the geometrical parameters and the optics functions of the novel dual BDS for CLIC 380 GeV.

CLIC 380 GeV				
	IR1		**IR2**	
	BDS1 e$^+$ (short)	**BDS1 e$^-$** (long)	**BDS2 e$^-$** (short)	**BDS2 e$^+$** (long)
θ [mrad]	0	0	4.83	4.83
L_{dipole}[m]	0	0	218.11	218.11
L_{FODO} [m]	38.36	38.36	38.36	38.36
L_{DS}[m]	512.89	551.24	512.89	551.24
L_{BDS} [m]	2255.95	2294.3	2255.95	2294.3
c.a. [mrad]	16.5	16.5	26	26

2.2.2 Novel dual BDS optics design for CLIC 3 TeV

The dual lattice design is also developed for CLIC 3 TeV, keeping the compatibility between the two energy stages for both IRs. The procedure to make the new beamlines has been the same but in this case the additional length in order to place the dipoles is about 1 km. Figures 2.16 and 2.17 show the Twiss functions, β_x, β_y and η_x as function of the longitudinal position along the DS. The first figure on the top shows the existing DS with the FODO cell structure. The two figures on the bottom show the optics structure of the DS of the new design for the dual BDS: the middle one shows the shorter BDS (in Figure 2.16 BDS1 e^+ and in Figure 2.17 BDS2 e^-), while the bottom one shows the longer BDS (in Figure 2.16 BDS1 e^- and in Figure 2.17 BDS2 e^+). In the case of BDS2 $e^\pm$ three dipoles have been added in order to separate the two BDS. The θ value is 2.75 mrad to provide exactly the same transverse separation, 10 m, as for the 380 GeV design (the same locations of the IRs) and the crossing angles are for IR1 and IR2 respectively 20 mrad and 25.5 mrad. The new dual BDS layout design for CLIC 3 TeV option is shown in Figure 2.18. The layout of CLIC at both energy stages and for both BDS, is shown in Figure 2.19 where the crossing angles (c.a.) are indicated at the different IRs. The layout of CLIC 3 TeV is longer than the 380 GeV by 2000 m. These results indicate the tunnel construction compatibility of the dual CLIC BDS, starting from the first energy stage of 380 GeV and going towards higher energies also in the case of the BDS2.
Table 2.3 summarizes the geometrical parameters and the optics functions of the novel dual BDS for CLIC 3 TeV.

Table 2.3: Summary table of the geometrical parameters and the optics functions of the novel dual BDS for CLIC 3 TeV.

CLIC 3 TeV				
	IR1		**IR2**	
	BDS1 e^+ (short)	**BDS1 e^-** (long)	**BDS2 e^-** (short)	**BDS2 e^+** (long)
θ [mrad]	0	0	2.75	2.75
L_{dipole}[m]	0	0	872.45	872.45
L_{FODO} [m]	76.72	76.72	76.72	76.72
L_{DS}[m]	1486	1562.75	1486	1562.75
L_{BDS} [m]	4190.66	4267.37	4190.66	4267.37
c.a. [mrad]	20	20	25.5	25.5

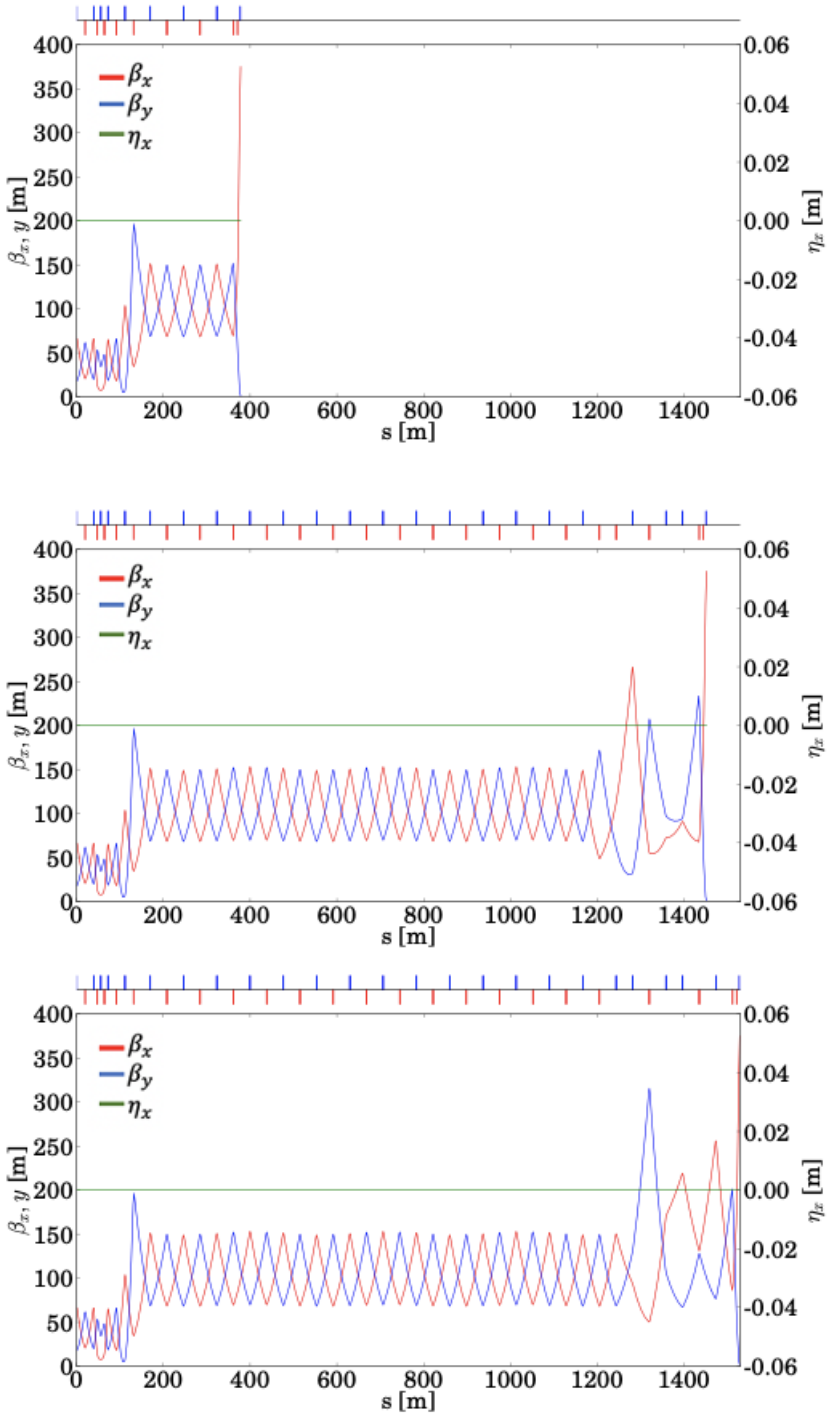

Figure 2.16: Top: DS of CLIC 3 TeV for the single IR. Middle: New DS for the dual IRs in the case of BDS1 e^+. Bottom: New DS for the dual IRs in the case of BDS1 e^-.

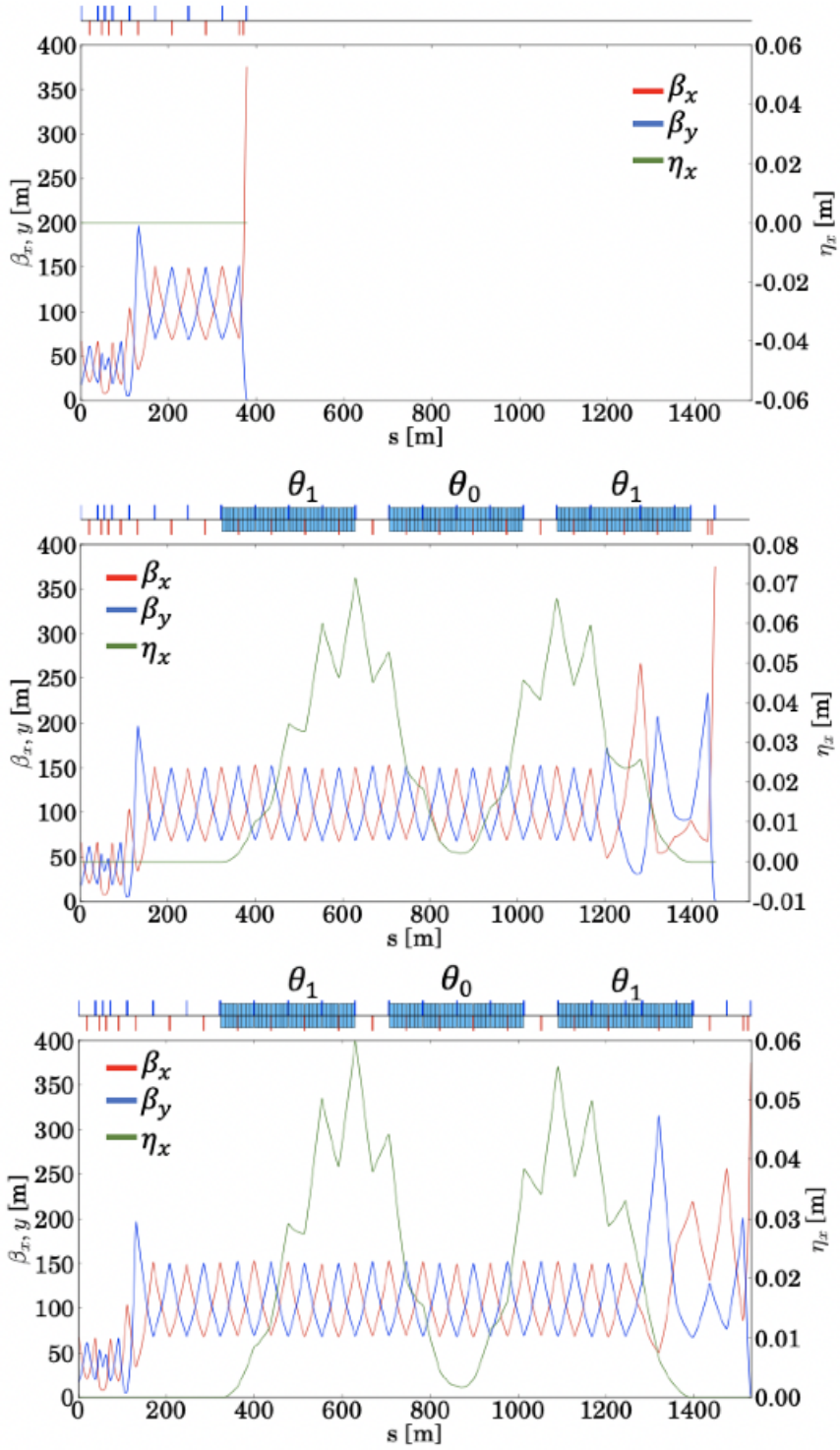

Figure 2.17: Top: DS of CLIC 3 TeV for the single IR. Middle: New DS for the dual IRs in the case of BDS2 e^-. Bottom: New DS for the dual IRs in the case of BDS2 e^+.

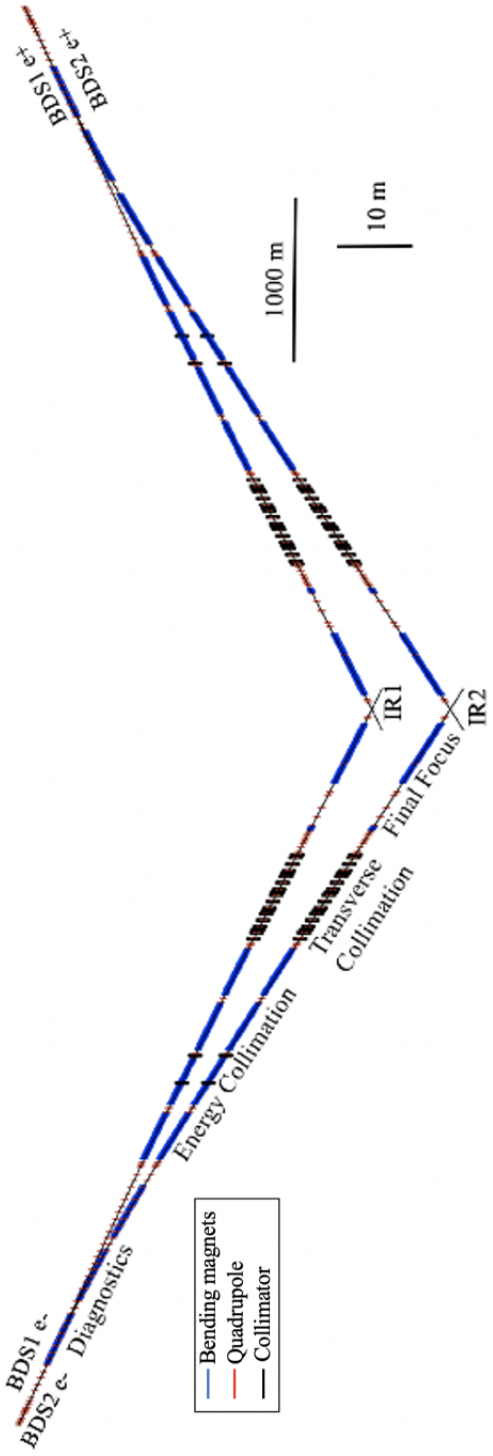

Figure 2.18: Layout of the new dual CLIC 3 TeV BDS System for two IRs.

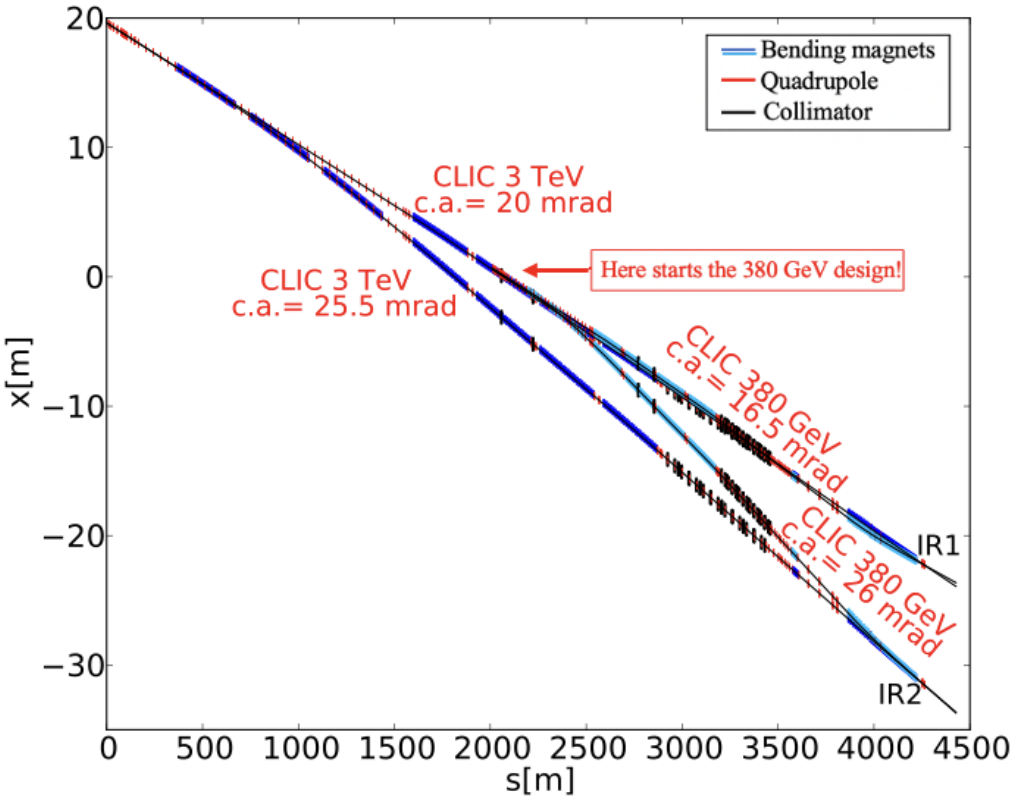

Figure 2.19: Comparison between the dual BDS layout of CLIC 380 GeV and CLIC 3 TeV.

CHAPTER 3

Detector solenoid impact of the CLIC BDS with long L* for one IR at 3 TeV

Aiming to simplify the CLIC MDI, a new detector model called **CLICdet** has been designed [16] allowing the last quadrupole QD0 of the FFS to be located outside of the experiment with a distance L* from the IP of 6 meters.

In this Chapter an overview on the past [15] and the new [16] CLIC MDI is presented. The performance results of the current CLIC 3 TeV design with L*= 6 m have been calculated including the detector solenoid effects for the first time.

3.1 CLIC MDI and its detector

The MDI design has to satisfy the requirements from both the FFS and the detector sides. It must ensure the optimum luminosity for the experiment with minimal backgrounds while meeting constraints from the infrastructure. The FFS L* parameter has a considerable impact on the design of the detector and MDI, in particular the integration of the last quadrupole QD0 inside the experiment. As already explained in detail in section 2.1 the L* in the CLIC post-CDR, known as PIP [16], has been extended to 6 m in order to better accommodate the detectors and in order to alleviate engineering and stabilization issues.

The CLIC CDR was considering the construction of two complementary detectors, the **International Large Detector (ILD)** and the **Silicon Detector (SiD)**, installed in a push-pull scheme as designed for the ILC [14], see Figure 3.1. The push-pull goal was to share the luminosity by the two detectors, to ensure a better yield of physics and allow confirming discoveries from independent groups. In order to avoid significant extra cost and loss of beam time during push-pull operations, and also because the physics reach was very similar for ILD [58] and SiD [59, 60], it was agreed to move towards a single detector [15].

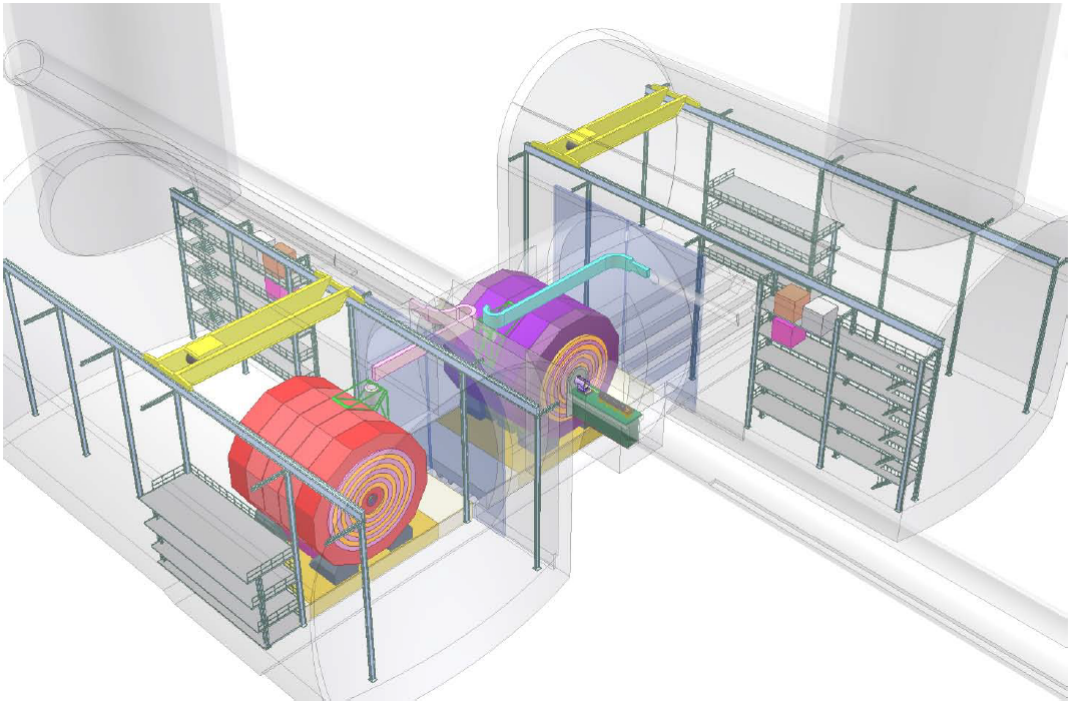

Figure 3.1: General view of the CLIC cavern layout with the push-pull configuration (ILD in violet and SiD in red) (Figure taken from [15]).

The single detector is based on the SiD model and produces a 5 T solenoid field. The FFS baseline for the CDR foresees a short L* of 3.5 m at 3 TeV leading to place the final quadrupole QD0 inside the experiment as illustrated in Figure 3.2. This layout choice was enforced to allow for the highest possible instantaneous luminosity [61] generally obtained with a short L*, assuming no external solenoid field or vibrations from the detector. Any vertical motion of this quadrupole translates into an equivalent displacement of the beam at the IP. To maintain the beams in collision, the vertical position of the quadrupole must be stabilized to 0.15 nm at frequencies above 4 Hz [15]. Measurements on and near the CMS detector [62] indicate that ground motion and technical noise are much larger on the detector than at the ends of the tunnel. It imposes the integration of a pre-insulator system [15, 63] and an active insulation to mitigate vibrations of QD0 inside the detector to the 0.1 nm level. This system still needs to be demonstrated in a detector-like environment. Due to the presence of a strong magnetic field, higher radiation, lack of space and access inside the detector, some critical components require longer interventions, leading to loss of integrated luminosity. Additionally, the QD0 being installed inside the detector takes away a significant fraction of the acceptance in the forward region. This is partially due to the need of shielding QD0 with an anti-solenoid [64], in order to reduce the interplay between the detector and the QD0 fields, which would otherwise cause important

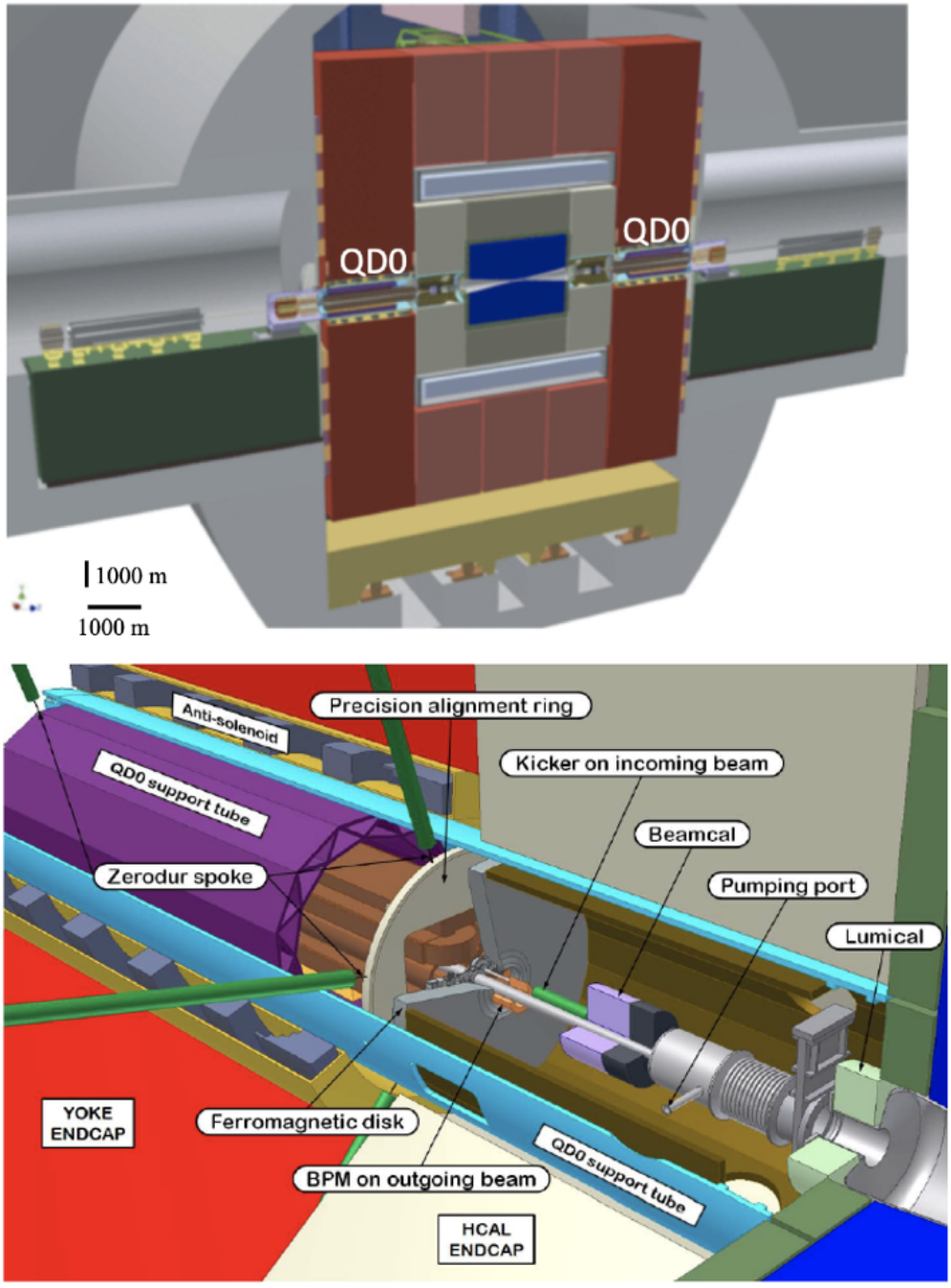

Figure 3.2: Top: Vertical cut through the SiD experiment for CLIC 3 TeV. QD0 is located inside the detector and partially supported by the preinsulator (green block) in the tunnel. The anti-solenoid is present for shielding QD0. Bottom: simplified MDI layout view showing a representation of part of the final-focus quadrupole, QD0, integrated into the CLIC SiD detector and shielded by an anti-solenoid [20].

quadrupole field deterioration and luminosity loss [65]. A schematic overview of the baseline IR design together with the simulated solenoid fields expected with the anti-solenoid are shown in Figure 3.3.

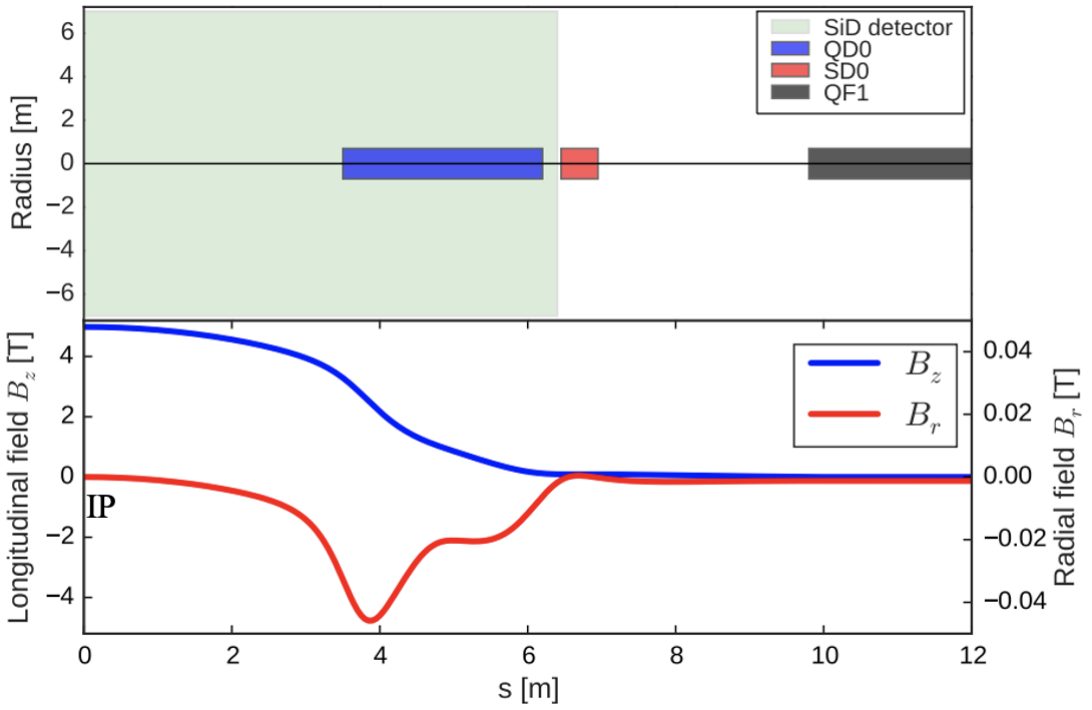

Figure 3.3: Schematic overview of the SiD interaction region layout from the last 12 meters of the FFS (top). Simulation of the longitudinal and radial fields (bottom). QD0 overlaps with the SiD solenoid field for L* = 3.5 m of CLIC 3 TeV.

Because the beam enters the detector solenoid with a crossing angle, the magnetic field of the solenoid has a component perpendicular to the incoming beam direction. This causes several distortions of the beam at the IP. The longitudinal component also produces coupling. With the short L*, the most severe effects come from the fact that the main solenoid and QD0 fields overlap. In addition, since the QD0 uses permendur and permanent magnet material, the QD0 must be shielded from external fields. In order to both shield the QD0 magnet and reduce the beam distortions, an anti-solenoid is required. Preliminary designs of such an anti-solenoid consist of bucking coils surrounding the QD0 support tube and connected to the detector end-caps. The current of each bucking coil is adjusted in order to minimize the detector solenoid flux density along the beam trajectory. Beam dynamics simulations show that the anti-solenoid can cancel more than 90% of the beam distortions at the IP. The simulated field map is shown in Figure 3.4 for SiD [15] [28].

In order to alleviate engineering and stabilization issues of the CDR MDI design, it has been proposed in [66, 67] to move out QD0 from the detector to the tunnel by increasing

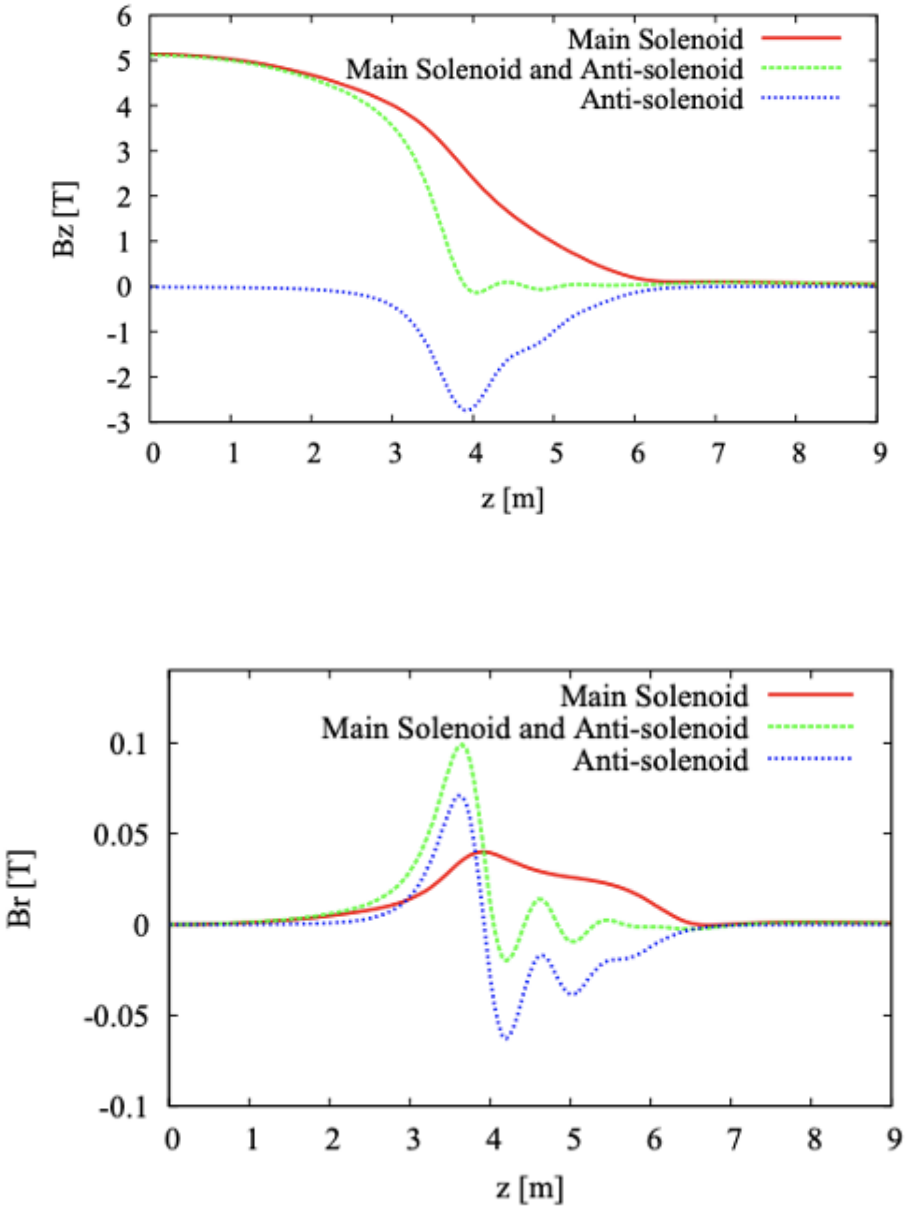

Figure 3.4: Longitudinal field after compensation, B_z, with the anti-solenoid (top), radial field, B_r, (bottom), for the SiD layout with L*= 3.5 m and for CLIC 3 TeV (Figure taken from [15]).

L*. Previous different studies post-CDR of the L* has been made and then decided to focus the design optimization studies on a FFS with L* = 6 m which started

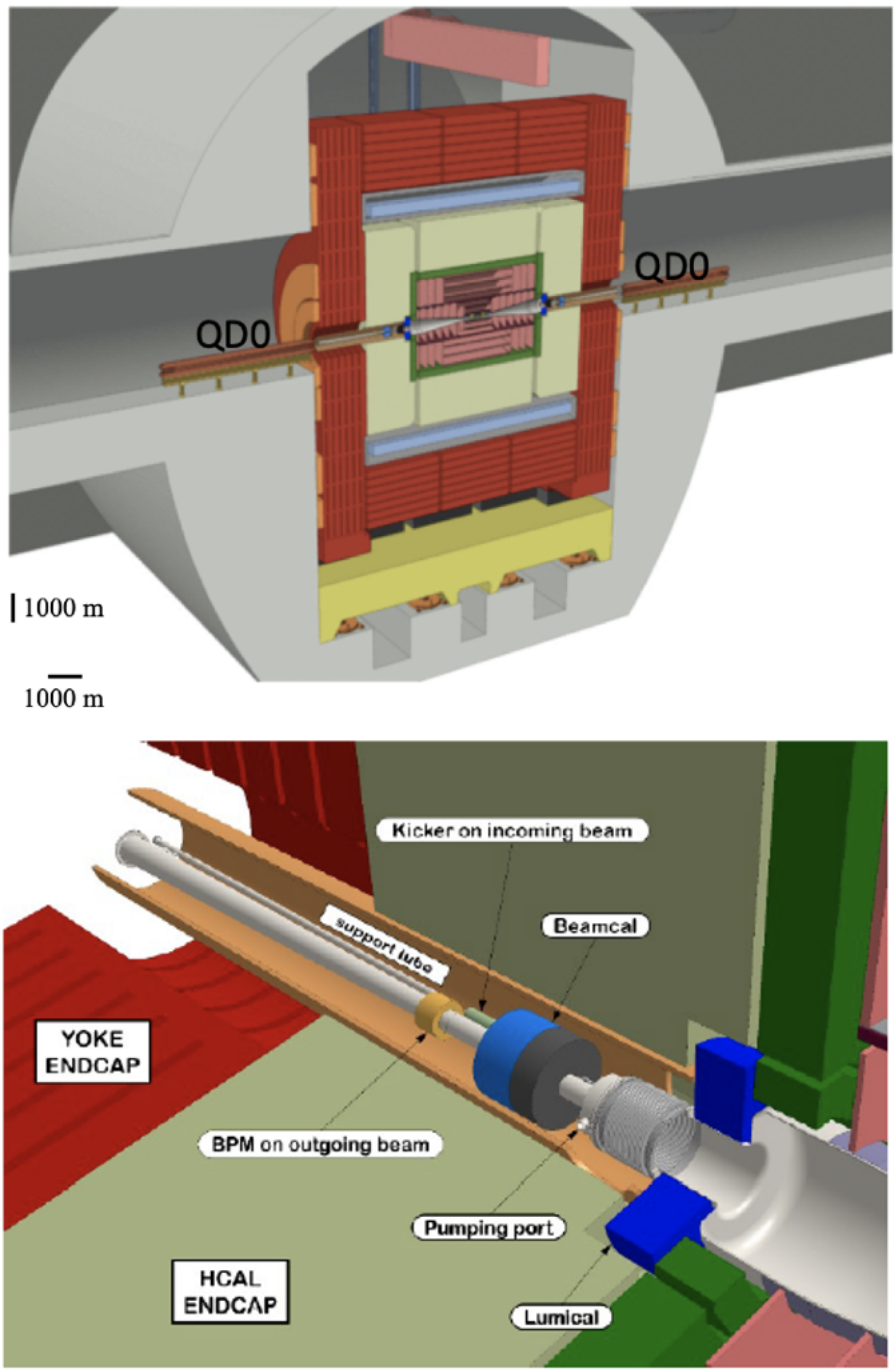

Figure 3.5: Top: Vertical cut through the new detector model CLICdet allowing QD0 to be located outside of the experiment for CLIC 3 TeV. No preinsulator or QD0 shielding with anti-solenoid are needed as opposed to the short L* design in Figure 3.2. Bottom: Forward region of the CLICdet experiment [20].

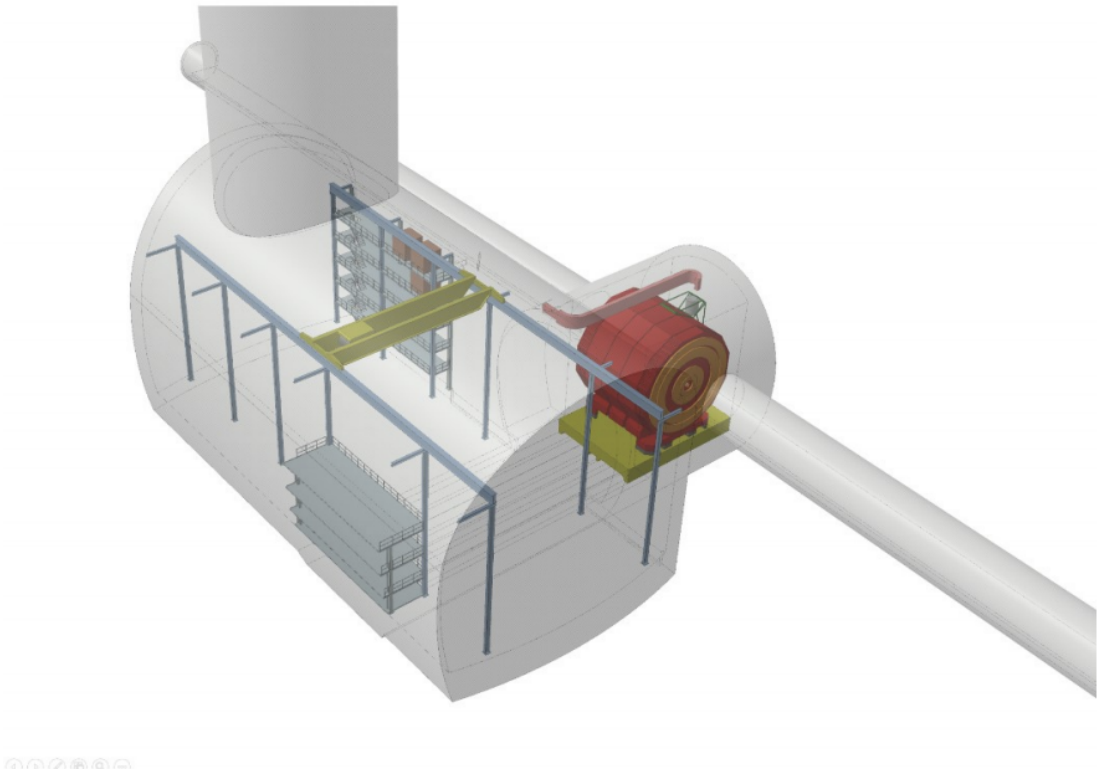

Figure 3.6: New cavern layout with the CLICdet (Figure taken from [16]).

in [43, 68], delivering luminosity close to the requirement but with more stringent tolerances against misalignment compared to the nominal design. The CLIC experiments have proposed a new detector model named **CLICdet** [69], allowing to move out QD0 from the experiment to the tunnel with a minimum L* of 6 m. The novel IR layout is illustrated in Figure 3.5 and the new cavern layout is shown in Figure 3.6.

This new detector provides a 4 T solenoid field. The reduced end-cap and barrel yoke give a half length of the detector of 5918 mm which includes 4 ring coils used to remove the solenoid stray fields in the tunnel. The tunnel floor is much more stable than the detector which will significantly ease the QD0 stabilization [66, 67]. The pre-insulator system is no longer needed and the access to the detector and QD0 is also simplified. The radial and longitudinal fields of the solenoid of the new detector are shown in Figure 3.7 along the first 12 meters from the IP. The fields are zeroed at the QD0 entrance and thus no anti-solenoid shielding is needed. The IP feedback position and latency are not affected by the change in L*. The new detector and FFS layout should reduce the overall risk, improve the MDI feasibility and increase the detector acceptance [28].

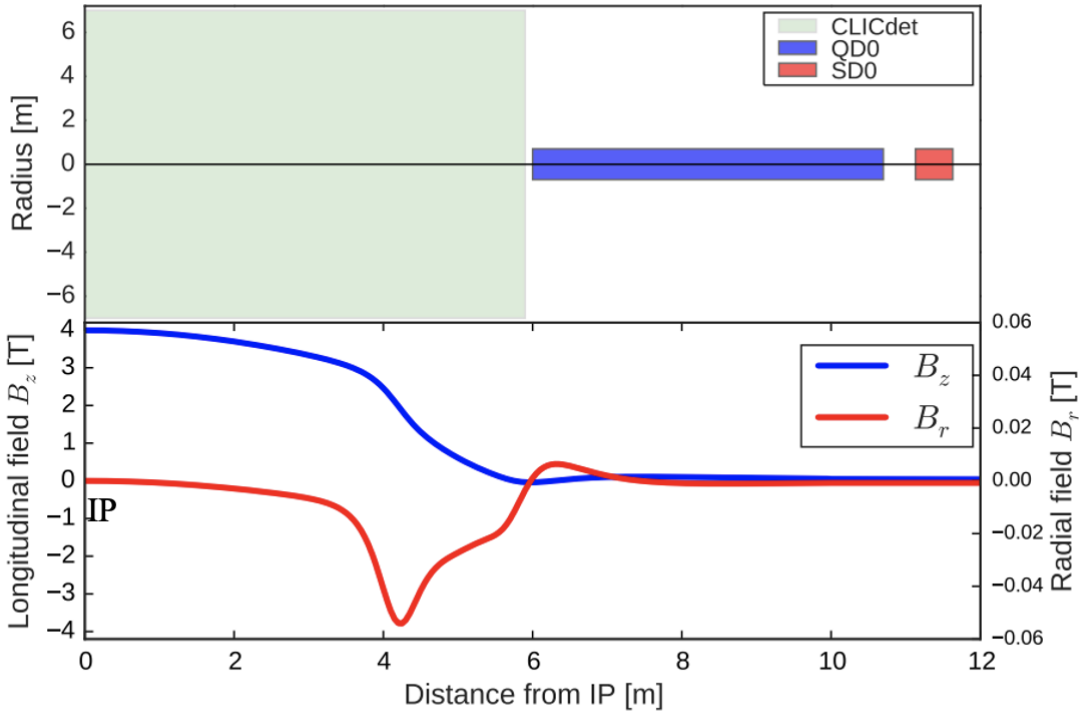

Figure 3.7: Schematic overview of the new detector (CLICdet) interaction region layout from the last 12 meters of the FFS (top). Simulation of the longitudinal and radial fields (bottom). No overlapping between QD0 and the new detector field with L* = 6 m.

3.2 Detector solenoidal effects

The CLICdet experiment forsees a solenoid field of 4 T [15]. Due to the CLIC crossing angle (θ_c) that is 20 mrad for CLIC 3 TeV, the beams do not travel parallel to the solenoid field resulting in beam coupling, vertical offset and residual dispersion at the IP. If the FD quadrupoles are away from the influence of the solenoid field, the vertical offset at the IP is given by [70]:

$$\Delta y^* = \frac{B_s L^{*2}}{B\rho_r}\frac{\theta_c}{4} \tag{3.1}$$

where B_s is the solenoid field. If QD0 and QF1 are outside of the detector, the e^+ and e^- beams will ideally have zero vertical orbit deviation a the IP and furthermore the coupling terms are also cancelled at the IP [71]. The vertical orbit offset generates SR and the beam size is [70]

$$(\Delta\sigma_y^{SR})^2 = C_E\gamma^5\int_0^\infty \frac{R_{36}^2(z)}{|\rho_r(z)|^3}dz \tag{3.2}$$

with

$$C_E = \frac{55}{24\sqrt{3}} r_e \lambda_e. \tag{3.3}$$

3.3 Calculation of the impact of the detector solenoid effects for the CLIC BDS with long L* at 3 TeV

In CLIC this vertical orbit offset is typically of the order of 10 μm, for a solenoid field of 4 or 5 T and 1.5 TeV beam energy. The displacement results in a large vertical dispersion at the IP. Furthermore, the beams in CLIC are exceptionally flat, ($\sigma_x^* \gg \sigma_y^*$), which means that any coupling to the vertical plane significantly deteriorates the luminosity. Particles with large angles at the IP have a large displacement from the beam orbit in the region close to the last focusing magnet, where the radial solenoid field is strongest. Hence, the experimental solenoid introduces strong < y, x'> coupling at the IP which must be corrected. Furthermore, due to the high beam energy in CLIC, there is a significant emission of SR as a result of the beam deflection in the solenoid region.

The unrecoverable loss is an important concern for CLIC. Optical aberrations can be corrected in several ways; the first method is adding skew quadrupoles or compensating solenoid, as done around the FINUDA detector at DAΦNE [72], the second is using dipole orbit corrector integrated into the experiment [73], proposed for ILC [70] and finally considering longer L* [66]. This last option has been chosen for CLIC.

The impact of the detector solenoid on CLIC luminosity performance was studied in [74] for the L* = 3.5 m design for CLIC 3 TeV. The MDI design taken into account in that study was the one of the SiD experiment [15]. Using the tracking approach described in the following section, it has been evaluated that the loss of peak luminosity due to the detector solenoid effects including the anti-solenoid was found to be about 4% for the SiD detector solenoid field map. The anti-solenoid reduces the losses by approximately 1%, and strongly reduces the optical distortions.

In order to evaluate the luminosity loss due to the solenoidal field effects a special tracking procedure has been used. This procedure has been developed in [74]. The procedure sketched in Figure 3.8 is the following: the beam is first tracked forward without SR, and without the solenoid field present (1). This provides the optimal beam distribution at the IP. The ideal IP beam distribution is tracked backwards through the beam line, with the solenoid field turned on but still without SR (2). The result is a beam distribution with a perfect compensation for the coupling introduced by the solenoid field. Finally, the SR is turned on, and the beam is tracked forward through the solenoid (3). The estimated luminosity is compared to a normal tracking of the beam without the solenoid field, but including the SR. From now on, this tracking procedure will be called forward-backward-forward. The results are compared with the direct (classic) tracking procedure to show consistency of results. For doing these particle tracking simulations, PLACET [75] has been used while GUINEA-PIG [76] has been used for the evaluation of the luminosity.

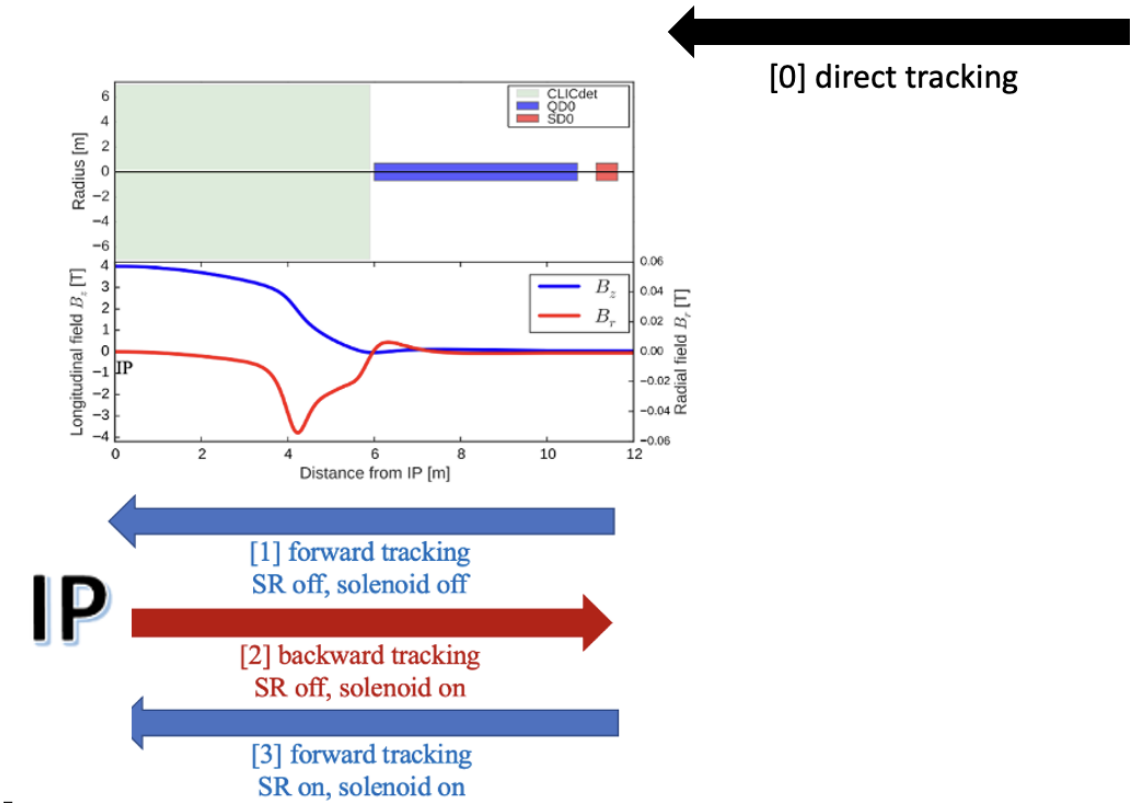

Figure 3.8: The direct and the forward-backward-forward tracking procedure is visualised in the last 12 metres of the FFS in CLIC.

The tracking including the solenoid field is done using a new 4th order symplectic integrator [74]. The code used for the evaluation of the performance results is briefly described in the appendix of the thesis, see B.

Using this technique and using the CLICdet experiment, the performance of the current CLIC BDS with one IR at 3 TeV including the impact of the detector solenoid field are first presented here. The beam size and the luminosity results are presented in Table 3.1. The ideal case does not consider SR and solenoid effects. The two tracking procedures used are the direct PLACET tracking procedure (the classic tracking with PLACET for the results of ideal and with SR) and the forward-backward-forward tracking procedure for the evaluation of the solenoid effects (results of ideal, with solenoid and with solenoid plus SR). The ideal case shows the same performance from the two different tracking procedures, as expected. The luminosity loss from the solenoid field for the current baseline with L*= 6 m is about 4% like for the previous design with L*= 3.5 m, see Section 3.3. The new performance for the current baseline with L*= 6 m will be used as the new reference for the evaluation of the performance for the CLIC dual BDS. We could already

advance that the solenoid impact for the CLIC 380 GeV case can be considered negligible since the results obtained for the BDS1 of the dual BDS configuration, shown in Chapter 4, have been found to be also negligible for this case.

Table 3.1: Beam size and luminosity simulations evaluated with the direct PLACET tracking procedure for the CLIC 3 TeV baseline design with L*=6 m (optics optimized in [28]) and with the forward-backward-forward tracking procedure for the evaluation of the solenoid effects.

CLIC 3 TeV								
	σ_x^* **[nm]**		σ_y^* **[nm]**		$\mathscr{L}_{TOT}$ $[10^{34}\,\mathrm{cm}^{-2}\mathrm{s}^{-1}]$			
	ideal	**w/ SR**	**ideal**	**w/ SR**	**ideal**	**w/ SR**	**w/ sol.**	**w/ sol.+SR**
baseline	41.4	50.3	1.06	1.69	9.40	6.50	8.65	6.22

CHAPTER 4

Global performance optimization of the novel CLIC Dual BDS for two IRs at 380 GeV and 3 TeV including the detector solenoid effects

In this chapter the performance optimization in terms of beam size and achievable luminosity for the CLIC dual BDS at both energy stages and including also the detector solenoid effects is presented. Moreover, the impact of the anti-solenoid for the CLIC 3 TeV case is studied.

4.1 Performance Results for the CLIC Dual BDS at both energy stages

This section presents the global optimization results for the novel dual CLIC BDS for both energy stages. These simulations do not include the impedance. The study on the wakefields for the CLIC BDS can be found in [77]. In fact, also wakefields deteriorate the beam quality and in particular there are some components that can be high impedance sources in the IRs, like the resistive wall wakefields. The wakefield effect concentrates in the FFS, so a small increase of impedance is expected for the longer DS but mitigations could be possible as beam-screen size increase. This needs to be studied in the future.

4.1.1 Beam size calculations at both energy stages

In order to evaluate the **beam size** for the two different IRs, the direct PLACET tracking procedure has been used. The simulations include pinching of the beams and emission of beamstrahlung and assuming head-on collisions. In Table 4.1 the results are shown.

Table 4.1: Beam sizes for the BDS1/BDS2 e^- simulations for the two different IRs for both CLIC energies evaluated with PLACET direct tracking procedure (no solenoid), computed for BDS1 $e^{\pm}$ and BDS2 $e^{\pm}$.

CLIC 380 GeV				
	σ_x^* **[nm]**		σ_y^* **[nm]**	
	ideal	**w/ SR**	**ideal**	**w/ SR**
IR1	141	144	3.07	3.08
IR2	141	144	3.06	3.07
CLIC 3 TeV				
	ideal	**w/ SR**	**ideal**	**w/ SR**
IR1	43.5	51.5	1.02	1.71
IR2	44.9	64.8	1.02	1.92

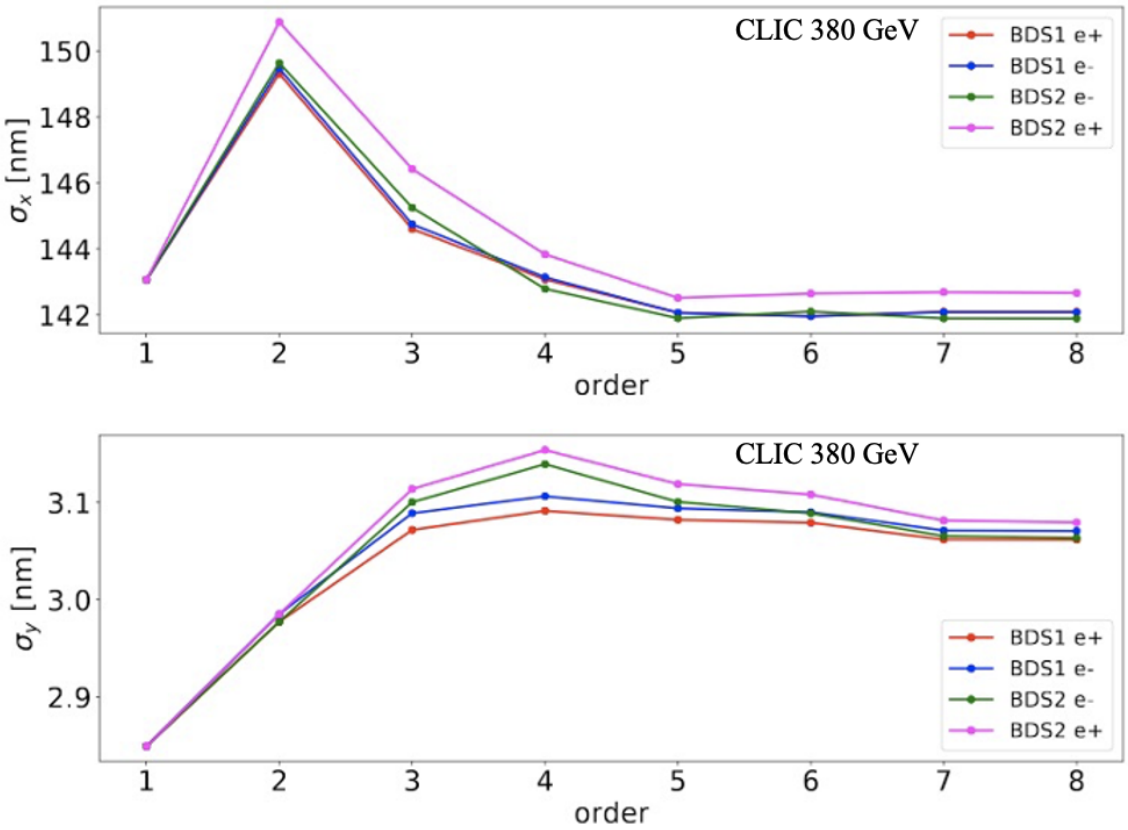

Figure 4.1: σ_x^* and σ_y^* evaluated with MAPCLASS until the 8^{th} order aberrations for the 380 GeV case.

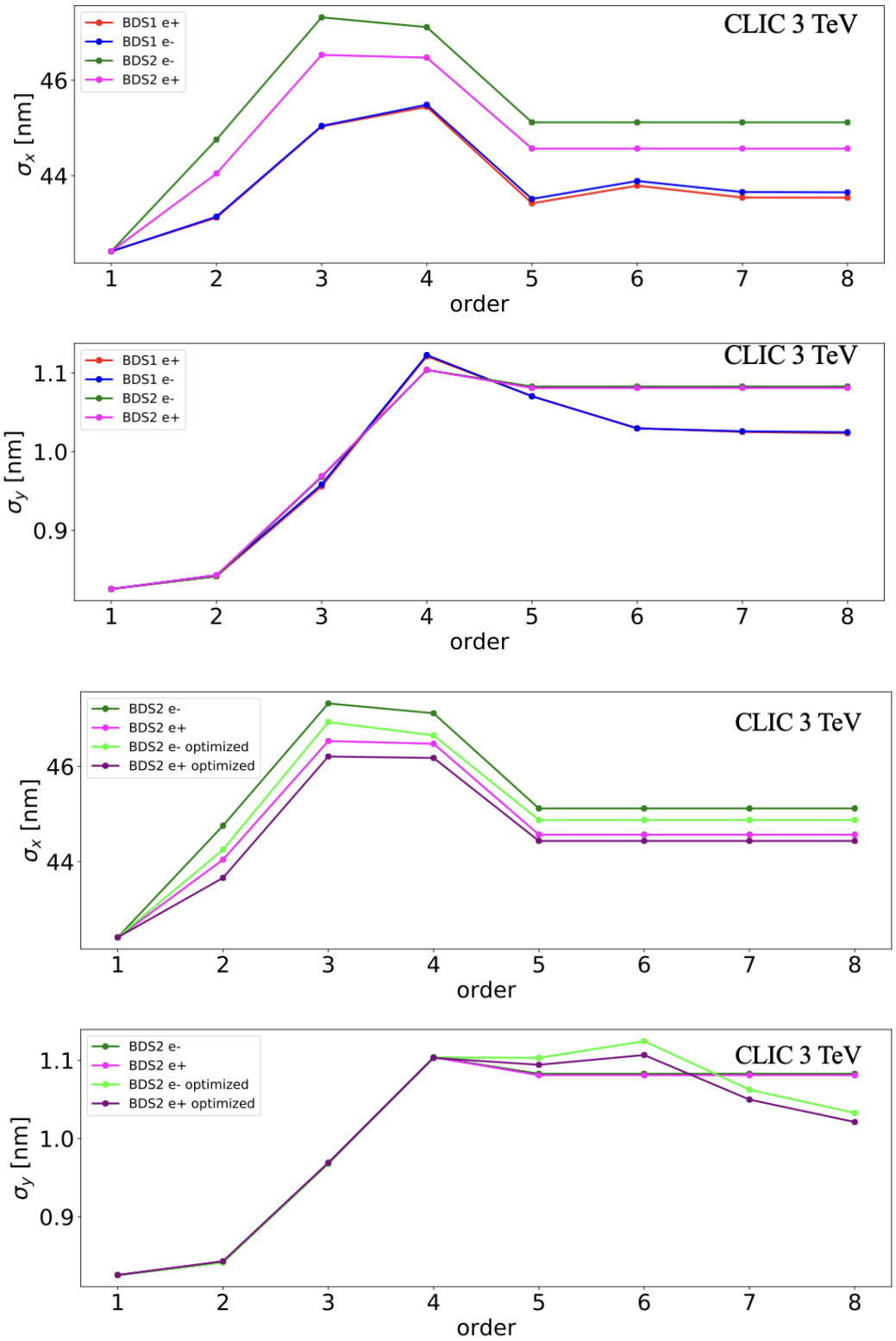

Figure 4.2: Top:σ_x^* and σ_y^* evaluated with MAPCLASS until the 8^{th} order aberrations for the 3 TeV case. Bottom:σ_x^* and σ_y^* evaluated with MAPCLASS until the 8^{th} order aberrations for the BDS2 e^+ e^- after the optimization for the 3 TeV case.

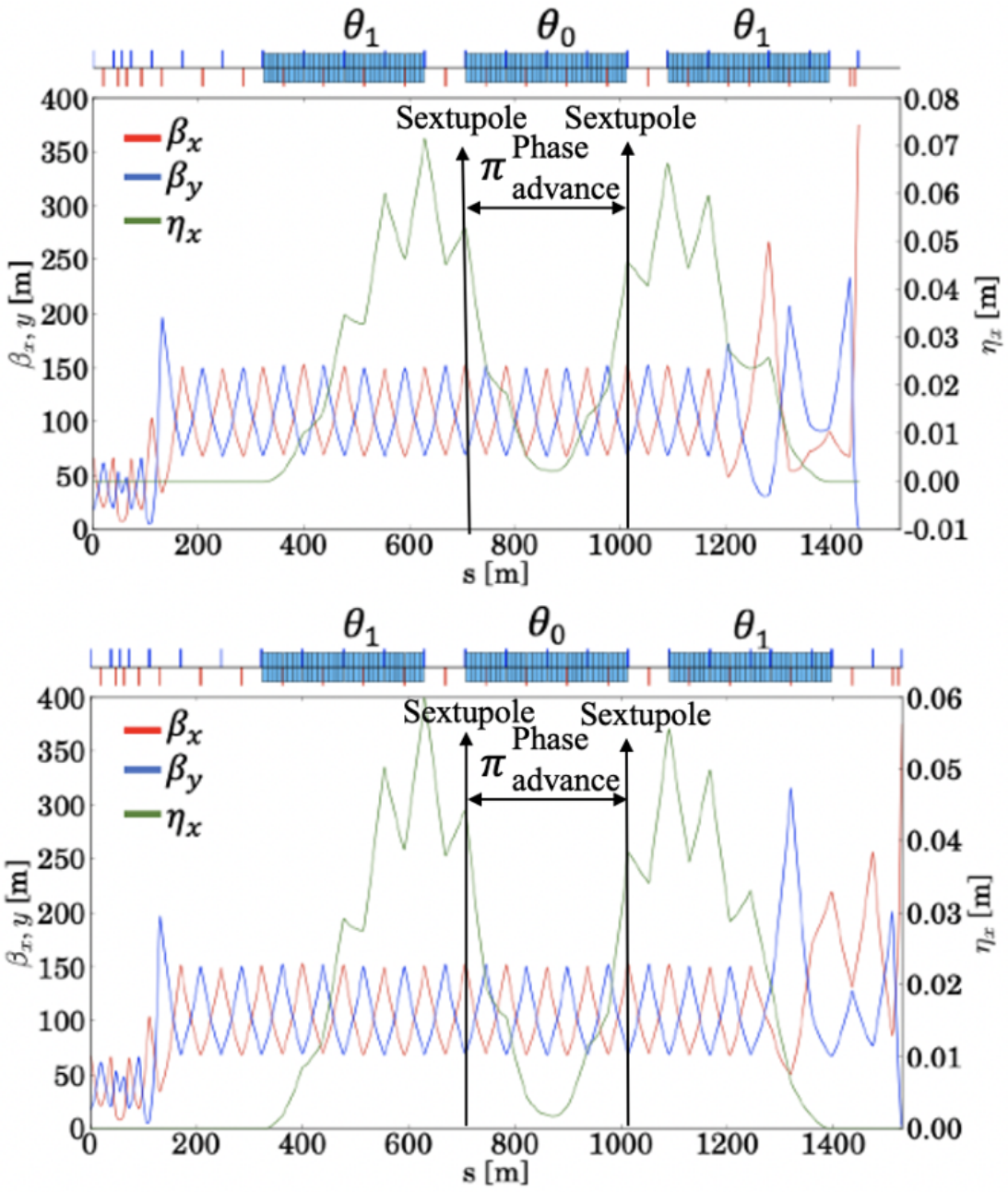

Figure 4.3: Top: New DS for the dual IRs in the case of BDS2 e^- including the added sextupoles positions for CLIC 3 TeV. Bottom: New DS for the dual IRs in the case of BDS2 e^+ including the added sextupoles positions for CLIC 3 TeV.

The tracking and the evaluation of the beam size has been benchmarked with MAP-CLASS [78–80] and PTC [81] codes showing good agreement. The results of these simulations are shown in Figures 4.1 and 4.2, where the beam size is evaluated up to

8^{th} order aberrations. The simulation was done for all the different BDS, the longer and the shorter cases (considering the different longitudinal displacement of the four different new beamlines) and for both energies, 380 GeV and 3 TeV. Figure 4.1 shows that the aberrations that mostly contribute to a beam size increase are the second order for the horizontal beam size and the third and fourth ones for the vertical beam size in the 380 GeV case. In Figure 4.2 we have a horizontal beam size increase due to the third order aberrations while a vertical beam size increase due to fourth order aberrations. In view of this, a further optimization of the 3 TeV cases was needed. This was performed by correcting the aberrations that mostly increase the beam size with a pair of sextupoles in the new DS (SF and SD). The sextupoles were added at locations with a large dispersion and β_x-function and with a π phase advance between them. The integrated sextupoles strength $K_2 l_q$ has been set to $-0.0205\,\mathrm{m}^{-2}$ for both sextupoles, with l_q= 0.5 m. Figure 4.3 shows the position of the sextupoles in the DS. Thanks to that, a small improvement of the beam size trend for the IR2 can be seen in Figure 4.2.

4.1.2 Luminosity calculations at both energy stages

Luminosities are evaluated with GUINEA-PIG using two bunches tracked along BDS1 and BDS2, respectively, with direct PLACET tracking procedure. Table 4.2 shows the luminosity performance for the two IRs for both CLIC energies. The direct tracking routine has been used and the results obtained are the ideal case and the case w/SR. The ideal case corresponds to the case without SR and without solenoid effects. The case w/SR corresponds to the case where the luminosity is evaluated with the SR effects on. The SR effects are very important because one of the main design drivers is the luminosity loss due to emittance increase and related widening of the beam sizes caused by the emission of SR as generated in the bending magnet section in the first added part of the BDS, the DS, to separate the two IRs. This effect is much more significant for the CLIC 3 TeV case.

4.1.3 Detector Solenoid Effects

The effect of the detector solenoid has been calculated with the forward-backward-forward tracking procedure described in section 3.3. The residual transverse magnetic field from the CLICdet solenoid is considered negligible beyond 10 m from the IP on the beamline. Different crossing angles imply different magnetic field near the IP. In fact, the transverse solenoid magnetic field increases with the increase of the design crossing angle, as shown in Figure 4.4 where we can also see the different radial and longitudinal fields for the different crossing angles of 16.5 mrad, 20 mrad, 25.5 mrad and 26 mrad respectively.

The CLICdet solenoid maps have been taken from [82] for all the 4 different crossing angles. In Appendix B the PLACET and GUINEA-PIG codes as well as the solenoid maps are reported. In Table 4.2 we can see the results of the simulations where the ideal

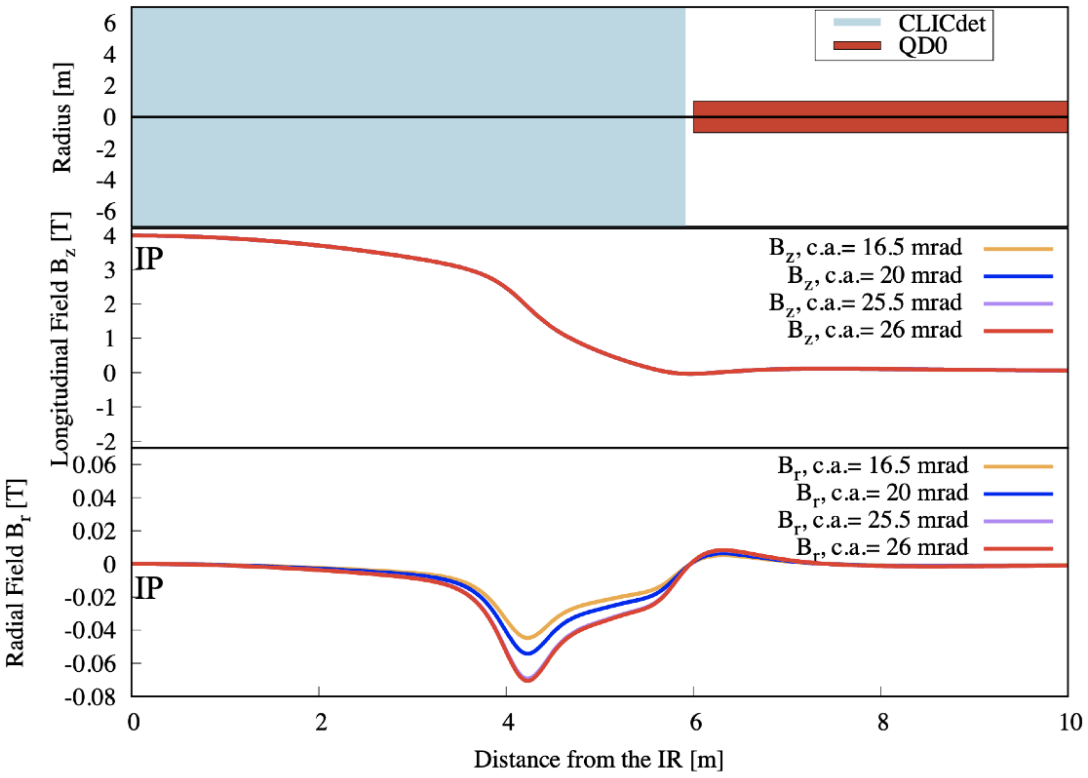

Figure 4.4: The radial and the longitudinal solenoid magnetic fields along the last 10 m before the IR in the solenoid reference system.

case is computed with both tracking procedures, the direct and the forward-backward-forward for comparison, while the case w/SR is evaluated with the direct tracking procedure, as explained before and the cases w/sol. and w/sol+SR are computed with the forward-backward-forward tracking procedure. From Table 4.2 we can conclude that the solenoid effects on luminosity for CLIC 3 TeV for the dual CLIC BDS are respectively of about 4% for IR1 and 19% for IR2. For comparison, a reference for the impact of all the past experiment solenoids on the CLIC luminosity can be found in [83].

Table 4.3 shows a complete summary of all the parameters of interest of the new CLIC dual BDS design taking into consideration also the solenoid effects for the luminosity evaluation in comparison with the current BDS design. For the dual BDS configuration, the beam sizes are the values computed w/SR while for the luminosities the values reported are the ones computed w/sol.+SR.

In order to increase the luminosity performance of the CLIC Dual BDS1 design at the level of the current CLIC baseline (L*= 6 m) the possibility of adding an anti-solenoid has been explored in the case of CLIC 3 TeV (20 mrad). A simulation with the new design but with the SiD experiment configuration [74], that includes the anti-solenoid, has been done.

Table 4.2: Luminosity performance evaluated with both PLACET tracking procedures, the direct and the forward-backward-forward (results for ideal, with solenoid, with solenoid plus SR), for the two different IRs and for the baseline for both CLIC cases.

CLIC 380 GeV				
	$\mathscr{L}_{TOT}$ [10^{34} cm^{-2}s^{-1}]			
	ideal	**w/ sol.**	**w/ SR**	**w/ sol.+SR**
IR1	1.515	1.512	1.492	1.412
IR2	1.491	1.475	1.466	1.392
CLIC 3 TeV				
	ideal	**w/ sol.**	**w/ SR**	**w/ sol.+SR**
baseline	9.40	8.65	6.50	6.22
IR1	9.00	8.21	6.30	6.09
IR2	8.33	7.59	5.14	4.17

Table 4.3: Parameters of the new dual CLIC BDS System for two IRs where the beam sizes are the values computed w/SR while for the luminosities the values reported are the ones computed w/sol.+SR.

CLIC	**380 GeV**			**3 TeV**		
	Current	**Dual BDS**		**Current**	**Dual BDS**	
	IR1	**IR1**	**IR2**	**one IR**	**IR1**	**IR2**
L* [m]	6	6	6	6	6	6
BDS length [m]	1949	2294	2256	3117	4267	4191
Norm. emittance $\gamma\varepsilon_x$ [nm]	950	950	950	660	660	660
Norm. emittance $\gamma\varepsilon_y$ [nm]	30	30	30	20	20	20
Beta function (IP) β_x^* [mm]	8	8	8	7	7	7
Beta function (IP) β_y^* [mm]	0.1	0.1	0.1	0.12	0.12	0.12
IP beam size σ_x^*[nm]	144	144	144	40	51	65
IP beam size σ_y^*[nm]	2.9	3.08	3.07	0.9	1.7	1.9
Bunch length $\sigma_z[\mu$m]	70	70	70	44	44	44
rms energy spread δ_p[%]	0.3	0.3	0.3	0.3	0.3	0.3
Bunch population N_e [10^9]	5.2	5.2	5.2	3.72	3.72	3.72
Number of bunches n_b	352	352	352	312	312	312
Repetition rate f_{rep} [Hz]	50	50	50	50	50	50
Crossing Angle [mrad]	16.5	16.5	26	20	20	25.5
Luminosity $\mathscr{L}_{TOT}$ [10^{34} cm^{-2}s^{-1}]	1.5	1.41	1.39	5.9	6.09	4.17

In the case of SiD experiment the central field is 5 T while for the CLICdet is 4 T, so the comparison is pessimistic. In fact, a central field of 4 T plus an anti-solenoid could improve even more the situation in our specific case. The presence of the anti-solenoid, as explained in Section 3.1 leads to a decrease of the SR effects, the optical aberrations

and the solenoid stray fields. So, adding an anti-solenoid to the dual CLIC BDS1 could reduce luminosity loss by at least 3% from the total of 4% coming from the solenoid and the SR effects. This option could be considered in future CLIC designs.

CHAPTER 5

First experiments for the validation of the ultra-low β_y^* nanometer beam size at ATF2 (CLIC FFS optics)

This chapter reports the ATF2 experimental tuning study done with the ultra-low β_y^* during March 2019 beam operation. This optics has a level of chromaticity comparable to the CLIC FFS and it is expected to reduce ATF2 σ_y^* below 40 nm.

5.1 The ATF2 Beamline and its FFS

As described in Section 1.3.2, the ATF2 accelerator facility is a scale down implementation of the FFS concept based to test the novel local chromaticity correction scheme that is implemented in the ILC and the CLIC FFS designs. One of the main goal of ATF2 is to achieve a vertical beam size at the IP of 37 nm. In 2016 an unprecedented vertical beam size at the IP of 41 ± 3 nm was reached in ATF2 using a reduced aberrations optics, known as nominal optics ($10\beta_x^* \times 1\beta_y^*$) [84, 85]. As shown in Figure 1.20 the ATF/ATF2 complex consists of:

- **Source and Linac**: The 88 m long ATF linac consists of an 18 m long 80 MeV pre-injector section and a 70 m long regular accelerator section with energy compensation structures. The RF gun with a 1.6 cell S-Band CsTe photocathode driven by a multi-bunch UV laser generates an electron beam with intensities up to 3.2 nC per bunch. Eight RF units of accelerating gradient of 35.2 MeV/m are used to accelerate the particle trains containing up to 20 bunches of up to 2×10^{10} particles per bunch. The beam energy at the linac exit is tunable up to a maximum energy of 1.54 GeV, while 1.3 GeV is the usual beam energy in recent operation. The

linac is operated at a repetition rate of 25 pps (pulses per second) to accommodate 5 circulating bunch trains in the DR [86].

- **Damping Ring (DR)**: The ATF DR is a race-track shaped storage ring with a 138.6 m circumference. The ring arcs are based on the FOBO type cells, where B stands for a combined function bending magnet with horizontal defocusing. The dispersion function is minimized in the bending magnet which helps in reaching a small equilibrium emittance [45]. The beam energy loss due to the SR is compensated by the 714 MHz RF cavity giving harmonic number of 330 and 165 buckets with 2.8 ns spacing [86].

- **Extraction Line (EXT)**: The EXT extends over 52 m and it comprises an extraction and a diagnostics section. The diagnostics section is used for measuring the emittance and the Twiss parameters and for correcting the dispersion and transverse coupling of the electron beam [43]. The beam is horizontally extracted from the DR straight section using a pulsed kicker (KEX1) and a current-sheet septum magnet (BS1X). The septum magnet is followed by two strong dipole magnets (BS2X and BS3X) that bend the extracted beam at an angle of about 20°. A dogleg inflector is located downstream from the septum dipoles comprising two approximately 10° bends (BH1X and BH2X) that offset the beam by 6 m from the damping ring. Downstream from the inflector is the $< x, y >$ coupling correction section consisting of four skew-quadrupoles with appropriate betatron phase advance to make the effects of the skew-quadrupoles orthogonal. The required conditions are that the first and second and also the third and fourth skew-quadrupoles are separated by 90° of phase advance in both planes, and the second and third skew-quadrupoles are separated by 180° in a horizontal plane and 90° in a vertical plane. In consequence, the first skew-quadrupole controls the $< x, y >$ phase, the second controls the $< x', y' >$ phase, the third the $< x', y >$ phase, and the fourth the $< x, y' >$ phase. The coupling correction section is followed by the emittance diagnostic section. Because of tight space constraints, the optics for this system is a short, modified FODO structure. The transverse beam emittances are reconstructed by measuring the transverse beam sizes using four Optical Transition Radiation (OTR) monitors [87]. These monitors provide fast single-shot measurements with full ellipse-fitting, allowing simultaneous measurement of the projected x and y spot sizes and the x-y tilt of the beam. Beam sizes at the measurement locations for the ATF2 nominal emittances (ε_x =2 nm, ε_y = 12 pm) range from 75 to 155 µm in x and from 7 to 20 µm in y [45]. The beam orbit diagnostic in the extraction line is handled by 46 beam position monitors (BPMs). Until November 2016 there were 13 stripline BPMs, located mainly in the inflector, with a single-shot resolution of about 10 µm, 33 C-band cavity BPMs [88], with sub-micron single-shot resolution and 2 button-type BPMs located near the septum [86].

- **Final Focus System (FFS)**: The ATF2 FFS beam line extends over 40 m and it is responsible for transporting and vertically focusing the beam at the IP to tens of

nanometers. It consists of a matching section composed of six quadrupole magnets (denoted by QM16FF, QM15FF, QM14FF, QM13FF, QM12FF, and QM11FF) whose function is to match the β functions measured in the EXT diagnostics section. In addition there are 14 quadrupole magnets which transport the beam to the FD that include one focusing (QF1FF) and one defocusing (QD0FF) quadrupoles meant to focus the transverse beam size at the IP. The last nine quadrupoles of the EXT beam line plus the transport quadrupoles of the FFS are referred to as QEA magnets. Three bending magnets, namely B1FF, B2FF, and B5FF, generate the required dispersion to correct the chromaticity by means of the five normal sextupoles, namely SF6FF, SF5FF, SD4FF, SF1FF, and SD0FF. In addition four skew-sextupoles, namely SK1FF, SK2FF, SK3FF, and SK4FF, have been installed in the FFS [84]. The lattice elements of the ATF2 FFS are shown in Figure 5.1. Figure 5.2 shows the $\beta_{x,y}$ and η_x functions along the FFS beam line in the case of the nominal and the ultra-low β_y^* optics [85], while the parameters can be found in Table 1.3.

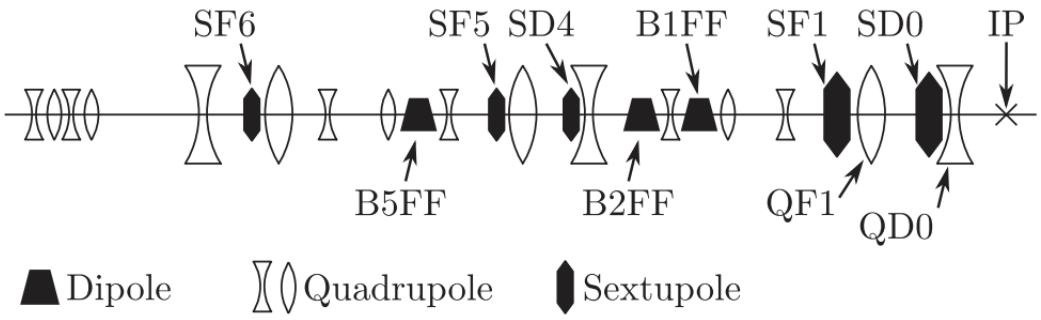

Figure 5.1: Schematic layout of the ATF2 FFS (Figure taken from [86]).

Two octupole magnets were added to the ATF2 beamline in 2016 in order to correct the multipolar field errors [43] and quadrupolar fringe fields [89] in the case of the ultra-low β_y^* optics. The octupole magnets design and manufacturing was done at CERN [23, 49]. One of the octupoles is installed in a dispersive location and the other in a non-dispersive location, with a phase advance of π between them, in Figure 5.3 the optics functions and the position of the two octupoles in the beamline is shown. The proposed and the actual locations for the octupole magnets are: OCT1FF (weaker octupole and the closest to the IP) between QD2AFF and SK1FF and OCT2FF (stronger octupole and furthest to the IP) between QD6FF and SK3FF. In Figure 5.4 the two ocupoles added in ATF2 beamline are shown.

- **Interaction Point (IP)**: The ATF2 focal point is called IP by analogy with particle colliders. In fact, the ATF2 provides just one particle beam, so no collisions occur there. Instead, the ATF2 performance is verified by measuring the IP beam sizes using the so-called Shintake monitor [90, 91]. This system consists of laser optics

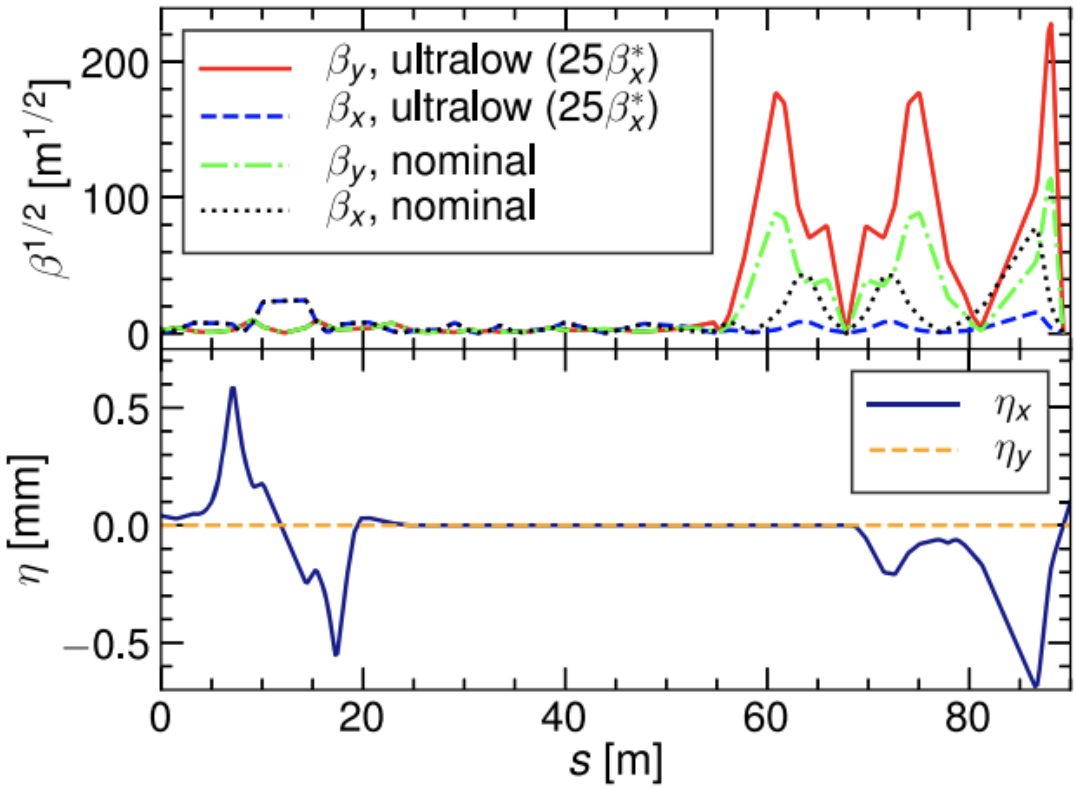

Figure 5.2: β functions and dispersion (η) along the ATF2 beam line for the ultralow β_y^* ($25\beta_x^*$) and nominal optics (Figure taken from [48]).

and a gamma detector. The laser, located outside the accelerator tunnel, generates laser pulses of wavelength $\lambda = 532$ nm, which are transported to an upright standing optical table located at the IP. The laser beam is there split into upper and lower paths. The two laser beams are focused at the IP where they cross in the plane transverse to the e^- beam to form interference fringes. The schematic layout of the beam size monitor is shown in Figure 5.5. As the e^- beam interacts with the laser interference fringes, the fringe pattern is modified by changing the phase of one laser path using the optical delay line. The beam size is inferred from the modulation of the resulting Compton scattered photon signal detected by a downstream photon detector. After collision, the beam is bent by a dipole magnet safely into a dump. The smaller σ_y^* is with respect to the fringe pitch, the larger the observed modulation will be (see Figure 5.5). The number of signal photons (N) is calculated by Eq. 5.1 as the convolution of a Gaussian beam distribution and the laser fringe intensity:

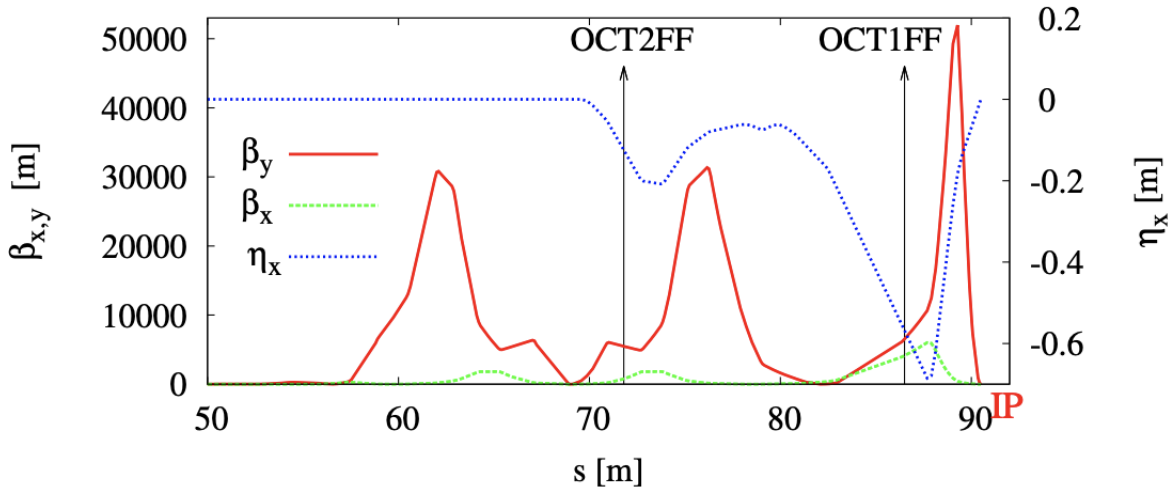

Figure 5.3: Optical functions of the ultra-low ($1\beta_x^* \times 0.25\beta_y^*$) lattice along the FFS beamline and location of the pair of octupoles installed at ATF2.

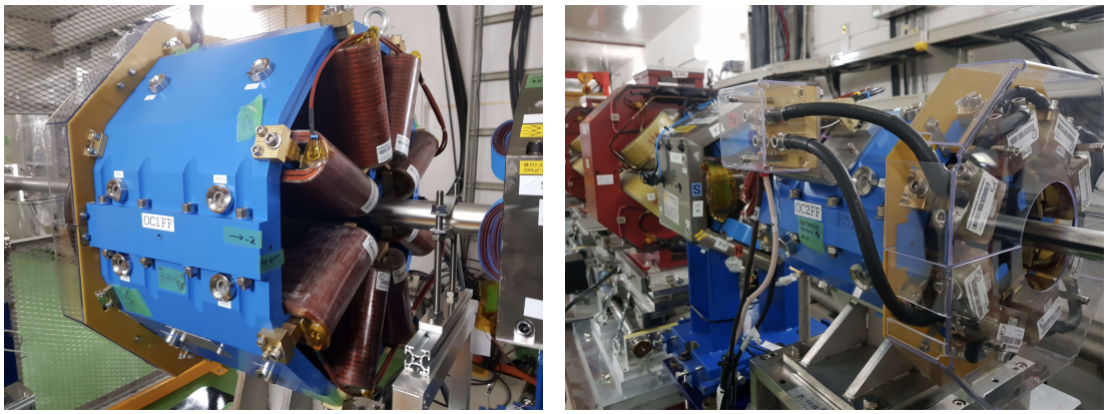

Figure 5.4: Octupoles installed in ATF2 FF beamline in November 2016. Left: OCT1FF; Right: OCT2FF (Figure taken from [28]).

$$M = \frac{N_+ - N_-}{N_+ + N_-} = |\cos\theta| \exp\left[-2(k_y\sigma_y)^2\right]$$
$$\Rightarrow \sigma_y = \frac{d}{2\pi}\sqrt{2\ln\left(\frac{|\cos\theta|}{M}\right)}, \tag{5.1}$$

where $k_y = \frac{\pi}{d}$, the fringe pitch $d = \frac{\lambda}{2\sin(\theta/2)}$, N_+ and N_- are the maximum and minimum signal intensity respectively and θ is the laser crossing angle. The Shintake

monitor has three laser crossing angle modes (2-8 deg, 30 deg, 174 deg) that extend the dynamic range from 5 µm to 20 nm, see Figure 5.6.

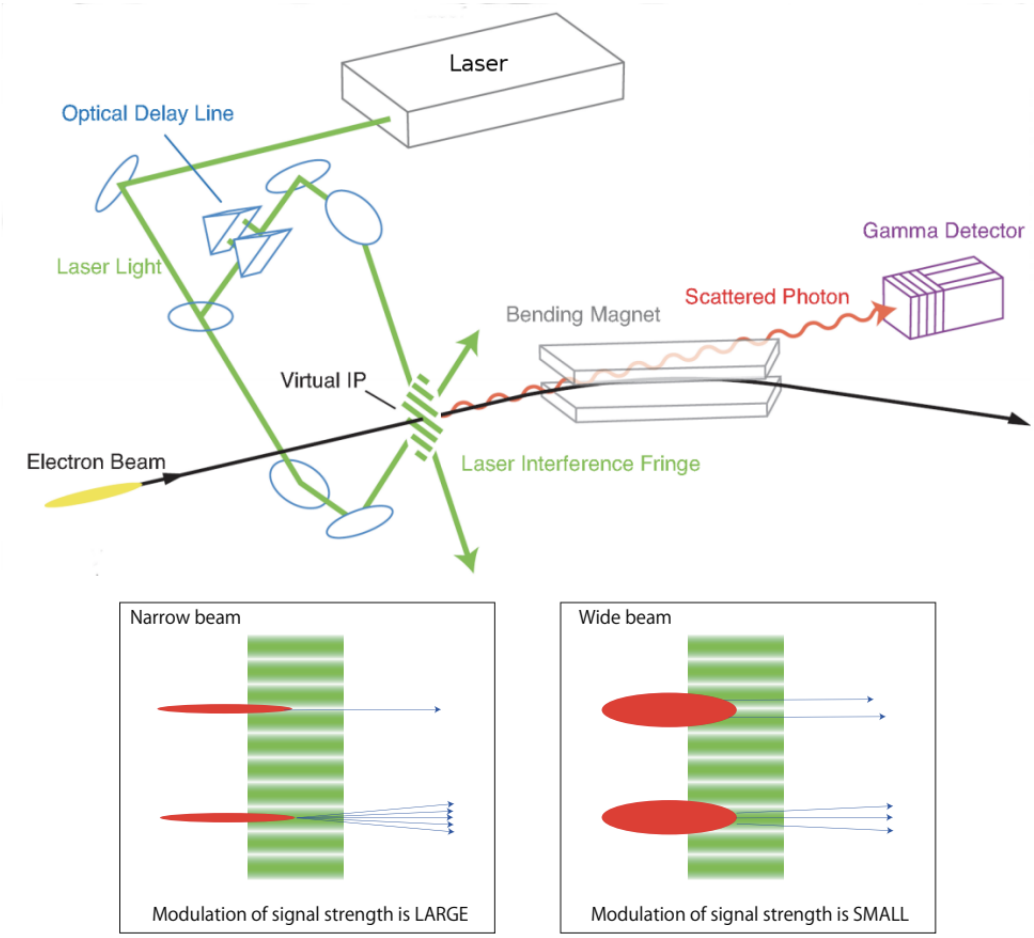

Figure 5.5: Shintake monitor schematic design. The electron beam interacts with a transverse interference pattern generated by two crossing laser beams. The number of scattered photons varies with the fringe size and the particle beam size (Figure taken from [28]).

An example of modulation measurement taken at ATF2 during the beam tuning, using the crossing angle mode $\theta = 30$ deg, shown in Figure 5.7.

Beam size measurements with the Shintake monitor experience various types of systematic errors that lead to an over-evaluation of the observed beam size. The overall effect of the systematic errors are represented by the modulation reduction factor C where $M_{measured} = CM_{ideal}$. The systematic errors related to the laser imperfections (alignment accuracy, polarization, temporal coherence, phase jitter, tilt of the fringe pattern and spherical wave front) were evaluated in [92, 93]. One important systematic error to be evaluated for the ultra-low β_y^* optics is related to the beam size growth within the fringe pattern. Due to the stronger focusing of the

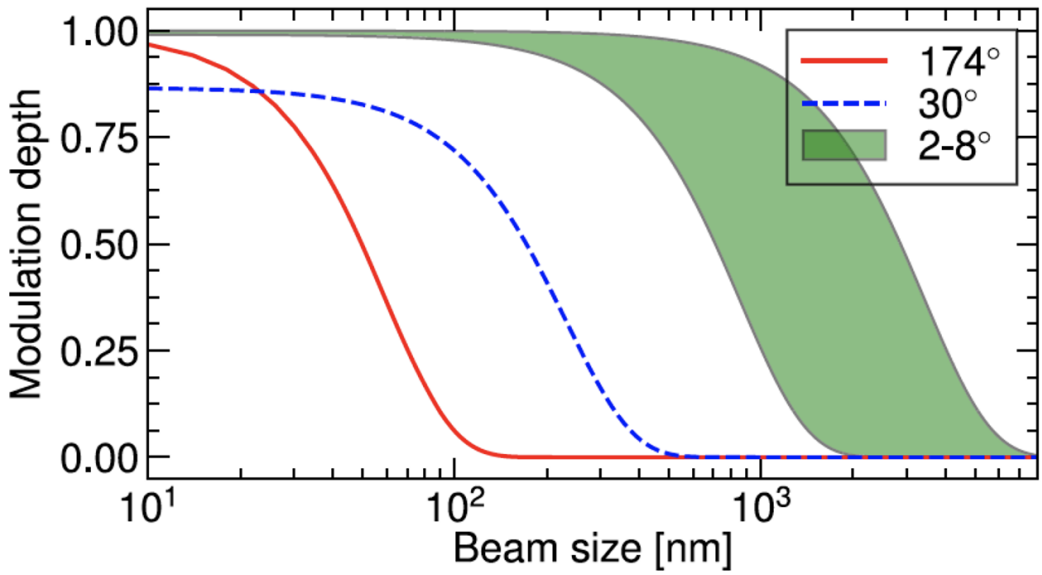

Figure 5.6: Modulation depth of the Compton signal as a function of σ_y^* for different operation modes (θ=2-8, 30, 174 deg) of the ATF2 Shintake monitor (Figure taken from [48]).

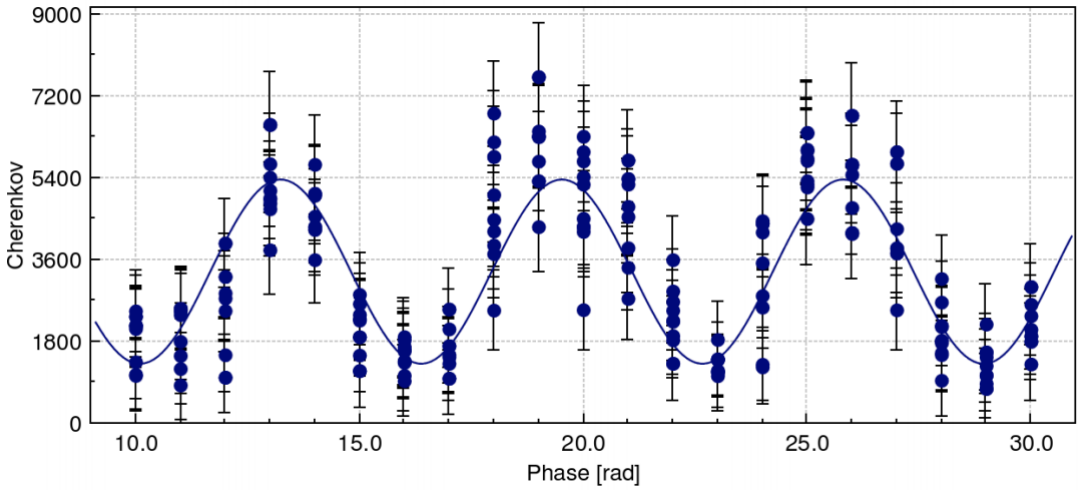

Figure 5.7: Example of an interference scan for vertical beam size measurement using the Shintake monitor at 30 deg mode (M = 0.6 $\Rightarrow$ σ_y^* = 130 nm) (Figure taken from [28]).

ultra-low β_y^* optics compare to the nominal one, the laser spot size at the IP in the longitudinal direction $\sigma_{z,laser}$, where $\sigma_{z,laser} \approx 15$ μm at 174 deg mode, becomes influencial on the measured modulation (see Figure 5.8). The modulation reduction factor due to beam size growth within the fringes ($C_{\sigma ygrowth}$) is given by [93]:

$$M_{meas.} = \left(1 + 4k_y^2 \sigma_{z,laser}^2 \frac{\varepsilon_y}{\beta_y^*}\right)^{-\frac{1}{2}} M_{ideal}. \tag{5.2}$$

For ultra-low optics (β_y^* = 25 μm) and ε = 12 pm, $C_{\sigma ygrowth}$ = 97.1 % at 174 deg mode while for the nominal optics (β_y^* = 100 μm) $C_{\sigma ygrowth}$ =99.7 %.

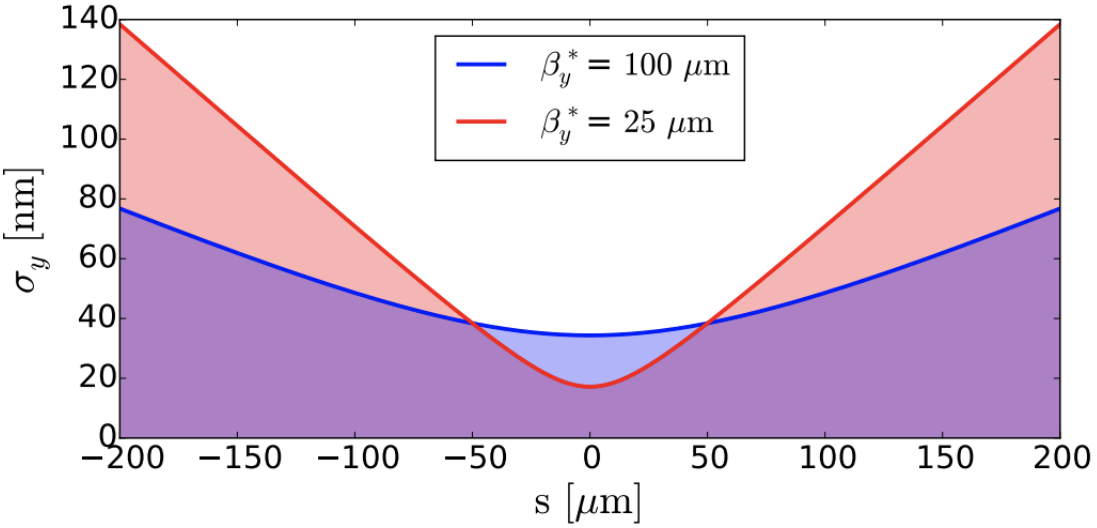

Figure 5.8: Vertical beam size comparison around the virtual IP for nominal optics (β_y^* = 100 μm) and ultra-low optics (β_y^* = 25 μm) (Figure taken from [28]).

5.2 The CLIC FFS test: ultra-low β_y^* at ATF2

In order to test the feasibility of the FFS local correction scheme in the condition of CLIC, with a chromaticity value about a factor 5 higher, the ultra-low β_y^* optics study has been proposed and studied in ATF2 (see Table 1.3), where the β_y^* value is reduced to 25 μm [23]. The expected ideal minimum beam size achievable, after high order optimization of the ultra-low β_y^* FFS design, is 20 nm when optimized with a pair of octupoles, added in order to correct the magnetic imperfections and the high order aberrations produced in ATF2 beamline [89]. Different opticshave been tested in ATF2 such as the nominal one (β_y^* = 100 μm), the half β_y^* (β_y^* = 50 μm) [85] and the ultra low β_y^* (β_y^* = 25 μm) [20, 94]. This chapter describes the ultra low β_y^* machine study done in March 2019 run.

5.3 First attempt for the experimental validation of the ultra-low β_y^* optics in ATF2 in March 2019

Following the same tuning procedure used with the half β_y^* optics in 2016 [85] and with the ultra-low β_y^* optics done in December 2017 and February 2018 (see vertical beam size reached in Figure 1.23) [20, 94], another attempt was done in March 2019 operation to study again the ultra-low β_y^* optics. A total of 7 shifts (56 hours) have been allocated for the ultra-low β_y^* optics study in March 2019 run. The results of these experimental studies are reported below.

5.3.1 Complete machine tuning procedure description

The ATF2 machine tuning procedure consists of [95]:

1. **Orbit correction**: the beam is steered flat at the BPMs center using the available EXT line correctors and the FFS magnet movers.
2. **Dispersion correction**: dispersion is measured along the FFS by observing the orbit change for the off-momentum beam compared to the on-momentum beam and it is corrected for the horizontal dispersion with QF6X quadrupole, while for the vertical dispersion with a pair of skew quadrupoles QS1X and QS2X.
3. **Coupling correction**: coupling is observed at the entrance of the FFS with m-OTR [95] and it is corrected by minimizing the emittance with Δ-knob and the skew quadrupoles.
4. **Optics matching at the IP**: Twiss parameters are measured with the wire scanner and matched to the design values with the matching quadrupoles.
5. **Beam based alignment (BBA)**: each sextupole is aligned with respect to the beam orbit by observing the orbit change on the downstrem BPM.
6. **Beam size tuning**: linear and non linear knobs are combinations of multiple magnets displacements meant to control a chosen set of beam aberrations in order to reach the desired beam size at the IP. They are iteratively used in the tuning process. The IP beam size is measured using the Shintake monitor.

More in detail:

5.3.1.1 Orbit correction

The first step for a correct machine tuning involves the orbit correction in order to reach the best reference orbit possible, called "golden orbit" that corresponds to the orbit with the skew sextupoles aligned in the center (as skew sextupoles are not on movers). The beam orbit diagnostic in the extraction line is handled by 46 BPMs.

In Figure 5.9 the position of the skew sextupoles along the beamline is shown. To reach this orbit, some of the ATF2 horizontal and vertical steering magnets are used and the orbit correction is done by changing their currents to minimize the beam offset at the BPMs located along the FF beamline [88]. We could also see an illustration of the orbit during March 2019 beam operation. To be noticed that the last two BPMs around 80 m are not working correctly due to BPM reference signal drifts and that at the beginning of the EXT line (at around 10 m) there is an orbit bump due to the septum presence and the higher sensitivity of the BPMs in that specific location. The black orbit in Figure 5.9 represents the difference between the real time orbit and the "golden orbit" and it was quite stable during all March 2019 dedicated week for the ultra-low β_y^* study.

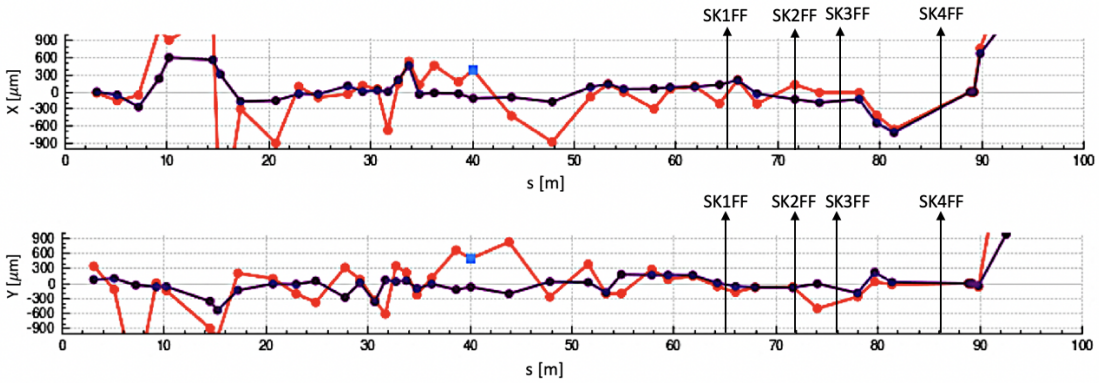

Figure 5.9: An example of the orbit displayed during March 2019 operation. Red: Real time orbit. Black: difference between the "golden orbit" and the real time orbit.

5.3.1.2 Dispersion and Coupling Correction

After correcting the orbit, dispersion is measured by changing the beam energy in the DR and observing the orbit change at the BPMs in the ATF2 beamline. Each measurement involved records the horizontal and vertical position shifts Δx and Δy at the BPMs for different settings of the damping ring rf frequency and fitting linear dependencies to the data to extract the dispersions:

$$D_{x,y} = \frac{\Delta x, y}{\Delta p/p}, \tag{5.3}$$

where $\Delta p/p$ is the relative momentum shift related to the frequency change Δf by

$$\frac{\Delta p}{p} = -\frac{\Delta f}{f_{DR}} \frac{1}{\alpha}, \tag{5.4}$$

where $\alpha = 2.14 \times 10^{-3}$ is the momentum compaction factor of the DR.

During dispersion measurements the DR frequency is changed by $\pm$ 2 kHz leading to a relative beam energy change of about $\mp$ 0.13%. The dispersion correction procedure at ATF2 uses quadrupole strength variations. In order to correct the dispersion along the FFS while not affecting too much other parameters, the quadrupoles used for the correction are located at the peaks of dispersion in the extraction line. The vertical dispersion is corrected using a pair of skew quadrupoles QS1X and QS2X that generate vertical dispersion via coupling from the horizontal dispersion. Their locations are shown in Figure 5.10. The <x, y> coupling generated by QS1X is canceled by QS2X thanks to the *-I* transfer matrix in both planes. The horizontal dispersion is corrected using 2 normal quadrupoles QF1X (located close to QS1X) and QF6X (located close to QS2X). Their strengths are varied independently until matching the design horizontal dispersion [20]. Figure 5.11 shows the horizontal and vertical dispersion corrected during March 2019 beam operation.

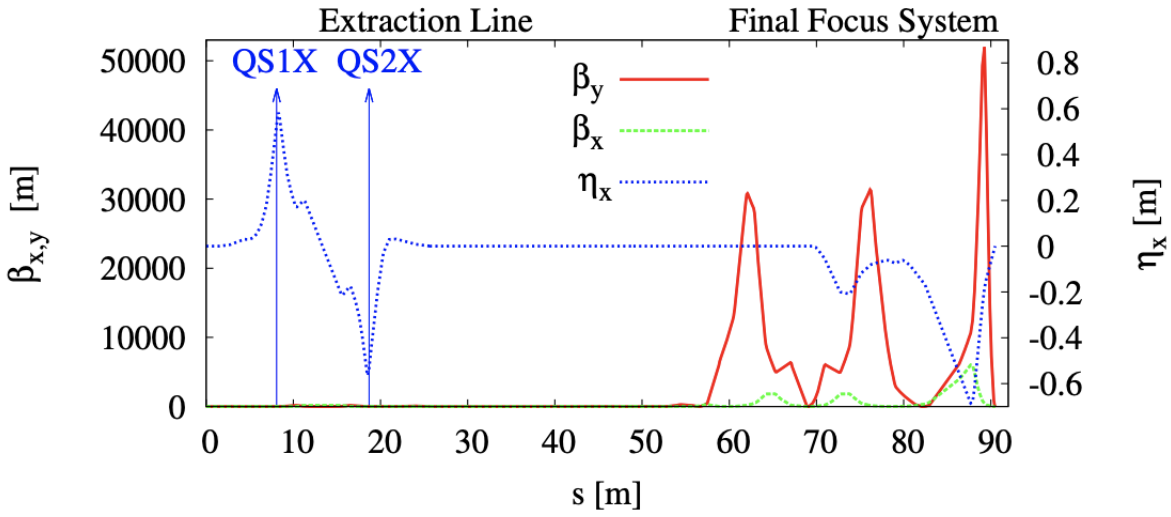

Figure 5.10: Optical functions along the extraction and the FF beamline with the location of the pair of skew quadrupoles used to correct horizontal dispersion and <x, y> coupling.

5.3.1.3 Optics Matching at the IP and BBA

The measurements of the $\beta_{x,y}^*$ values are crucial to verify that the desired optics was correctly implemented. The quadrupole scan method is used at ATF2 for the evaluation of the transverse beam parameters. The strengths of the FD quadrupoles QF1FF and QD0FF are scanned while the horizontal and vertical beam size, respectively, are measured using the IP carbon-wire scanner [71]. In the vincinity of the IP, σ_x and σ_y depend on the beam divergence and waist longitudinal displacement $\Delta f_{x,y}$ according to [20]:

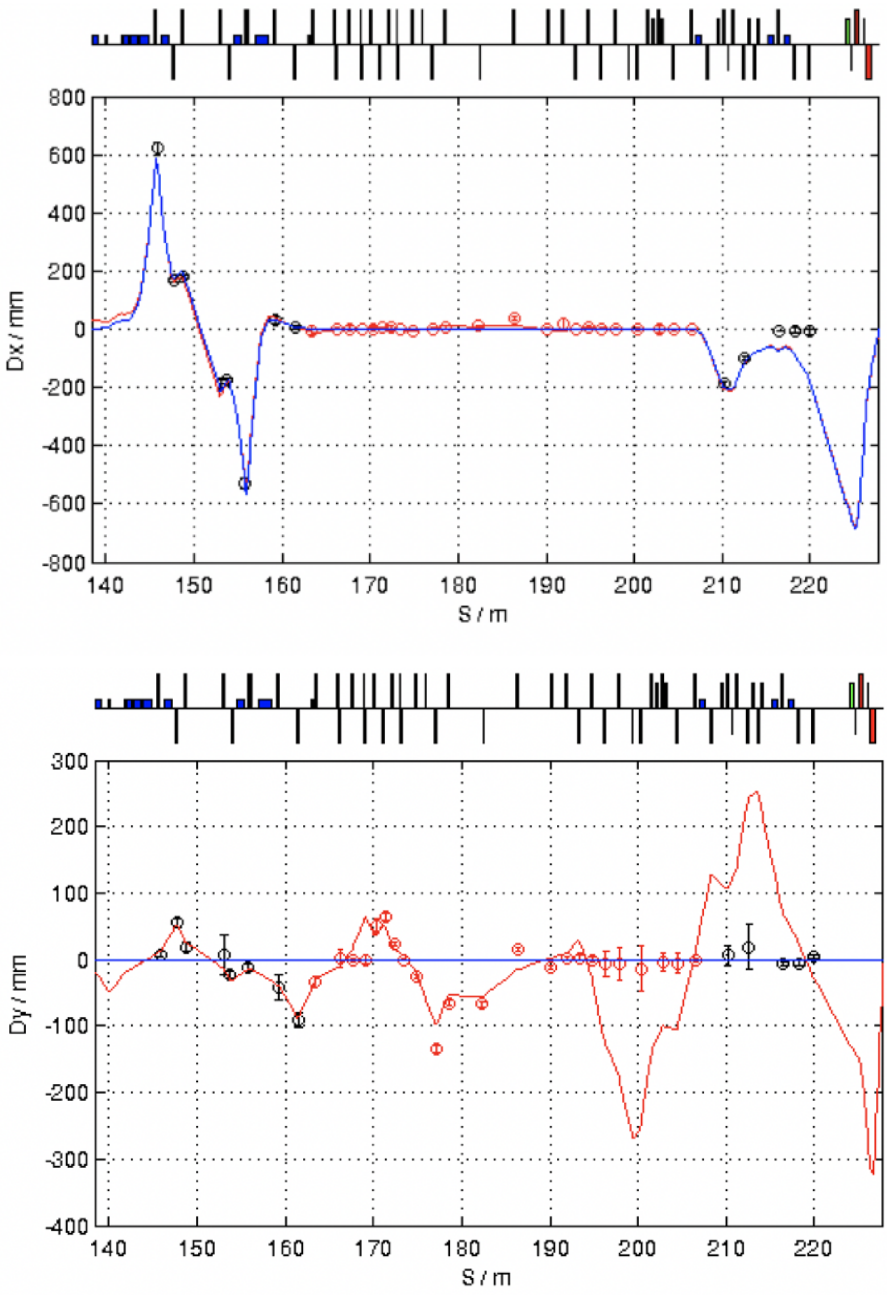

Figure 5.11: Horizontal (top) and vertical (bottom) dispersion after correction during March 2019 operation. The blue curves represent the design dispersion without machine errors for ATF2 beamline, while the red represents the fit done thanks to the measurements (black points).

$$\sigma_{x,y}^2 = \varepsilon_{x,y}\beta_{x,y}^* + \frac{\varepsilon_{x,y}}{\beta_{x,y}^*}\Delta f_{x,y}^2 \tag{5.5}$$

where the $\beta_{x,y}^*$ are the expected $\beta_{x,y}^*$ at the waist and the measured beam size has to be corrected for residual dispersion at the IP and for the geometric properties of the carbon wire as

$$\sigma_{x,y}^2 = \sigma_{x,y,measured}^2 - \sigma_\varepsilon^2 \eta_{x,y}^2 - \left(\frac{d}{4}\right)^2. \tag{5.6}$$

The ATF2 energy spread σ_ε is 0.6% for low beam intensity of 10^9 e^- bunch and the carbon wire diameter is d = 5 μm. For the horizontal beam size, for which the usual values vary from 6 μm to 10 μm, one can resolve the minimum beam size at the waist so that both emittance and β functions can be determined simultaneously by fitting the parabolic curves to the measured data as a function of the quadrupole magnet current. For the vertical beam size, instead, we expect that it is smaller than 1 μm at the start of the tuning and therefore it cannot be precisely measured at waist with the carbon wire. Only the beam divergence can be measured:

$$\frac{\varepsilon_y}{\beta_y^*} = \frac{\sigma_y^2}{\Delta f_y^2}. \tag{5.7}$$

Usually in ATF2, the vertical β function at the IP is determined by considering the vertical emittance measured upstream the FFS with the m-OTR [87]. During this run we did not evaluate the emittance value at the m-OTR location because of a problem with the vertical dispersion fitting in the software, so the β_y^* value is measured by approximating the emittance in FFS as the one measured in the DR.

From the scans in Figure 5.12 the β functions at the IP have been measured. The β_x^* was 80 $\pm$ 4 mm while the vertical divergence (ε_y^*[nm]/β_y^*[mm]) was 0.29 and considering the ε_y value the one measured in the DR ($\varepsilon_y = 9.9$ pm), the β_y^* was 35 $\pm$ 2 μm with the sextupoles off. The matching of the FFS quadrupoles as well as the sextupole alignment was not performed during the ultra-low β_y^* study. Because of lack of time we used the alignment done during the normal optics operation. Unfortunately, using this alignment that was not very efficient, with the sextupoles on, we had different values of the beta functions since the sextupoles were not well aligned: β_x^* = 120 $\pm$ 4 mm, and β_y^* = 30 $\pm$ 2 μm.

5.3.1.4 Beam Size Tuning

In the ATF2 beamline there are 5 normal sextupoles available for the knobs construction, namely SF6, SF5, SD4, SF1 and SD0 and also 4 skew sexupoles, namely SK4, SK3, SK2, SK1 which are available for the aberrations corrections. The linear knobs, that are currently available in the machine and give the best tuning performance are *AX* knob

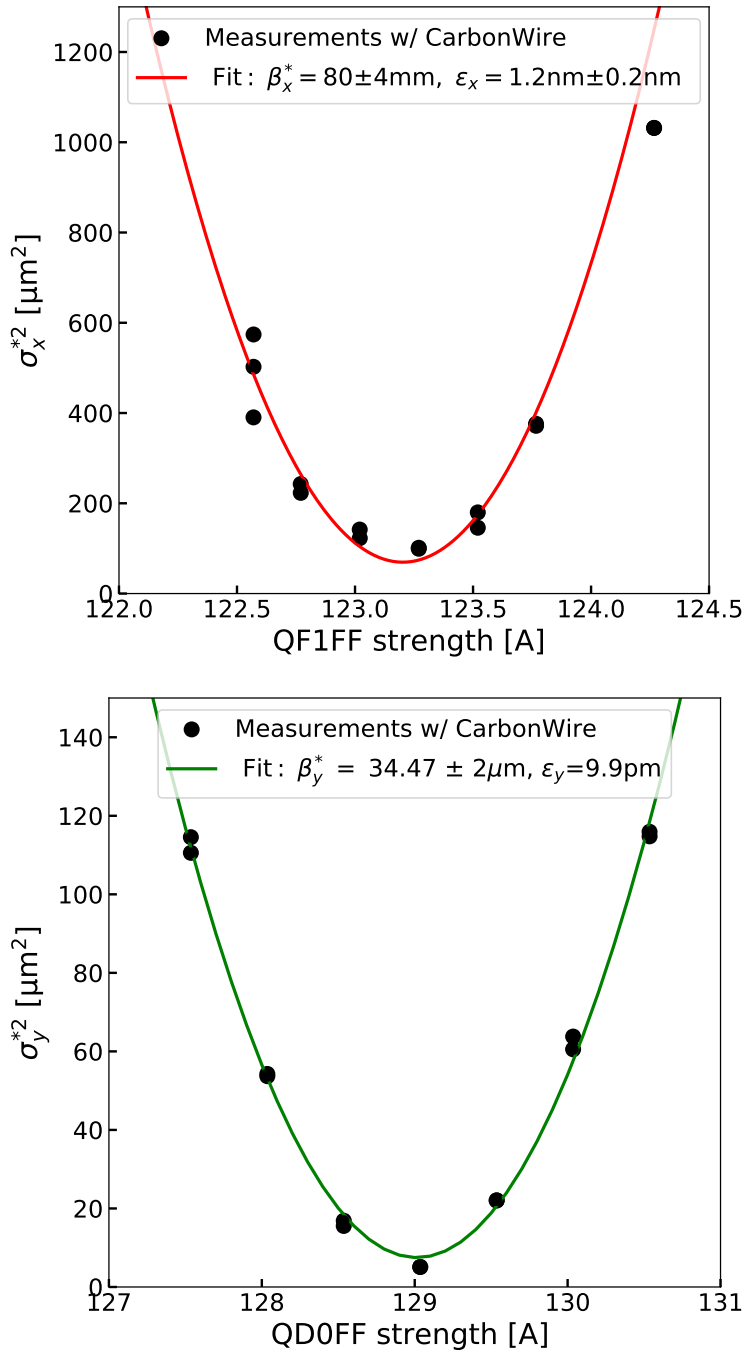

Figure 5.12: Top: Scan of the square of the horizontal beam size versus QF1FF strength done in March 2019 run. Bottom: Scan of the square of the vertical beam size versus QD0FF strength scan done in March 2019 run.

(horizontal waist shift), *AY* knob (vertical waist shift), *Coup*2 knob ($y \times x'$ coupling correction), *EY* knob (vertical dispersion correction). There are also Y_{24} (T^*_{324} term correction) and Y_{46} (T^*_{346} term correction) knobs constructed from the strength variation of the normal sextupoles and Y_{22} (T^*_{322} term correction), Y_{26} (T^*_{326} term correction), Y_{44} (T^*_{344} term correction) and Y_{66} (T^*_{366} term correction) knobs constructed with the skew sextupoles. From the simulations we know that the most important knobs for the tuning are the waist shift knobs, α_x^*, α_y^*, the vertical dispersion knob D_y^* and the coupling knob $< y, x' >$.

In the tuning process the knobs are applied sequentially, one by one. For each knob scan, the beam size is checked with the Shintake monitor for different knob amplitude. The square of the vertical beam size depends quadratically on the knob amplitude. By fitting σ_y^* with a parabola, it is possible to find the required knob amplitude for the minimum beam size. Ideally after a certain number of iterations we should be able to squeeze the vertical beam size to the design value. A detailed description of the ATF2 tuning knobs is given in [84].

The knobs used during March 2019 ultra-low β_y^* study are *AY*, *EY* and *Coup*2, *Y*24 and *Y*46. Figure 5.13 shows the modulation change when the linear knobs *AY*, *EY* and *Coup*2 were used during March 2019 beam operation.

5.3.2 ATF2 Energy dependence study

The study of the energy dependence effects on the vertical beam size (defined as df-knob) was for the first time tried with ultra-low β_y^* optics during March 2019 beam operation. From this first attempt with the df-knob, good results have been obtained. Smaller beam size (that means larger *M*) for higher beam energy can be seen in Figure 5.14 (for $dE/E \approx 0.1$ % (-2 kHz)). Further study for the energy dependence knob has been done during the others beam operations in 2019 and 2020. The results are presented in [96].

5.3.3 Discussion of the results

During March 2019 the ultra-low β_y^* optics was well matched and the Twiss parameters at the IP were well approximated to the design values, but unfortunately, the run ended with an incomplete machine tuning because of some technical problems that turned out to be the main limitations for reaching a very small vertical beam size at the IP.

During March 2019 run, 7 shifts in total have been allocated for the ultra-low β_y^* optics study. The first 4 shifts were mostly used to correct the orbit, the dispersion, the coupling and then match the β functions at the IP with the wire scanner (described in Section 5.3.1.3). A detailed description of the shifts schedule and actions is shown in Table 5.1. From the $\beta^*_{x,y}$ values with sextupoles on/off, it is clear to see that they were not perfectly aligned. Although the BBA was performed the week before the tuning week study, there was a residual sextupoles displacement during the beam operation weeks in March 2019.

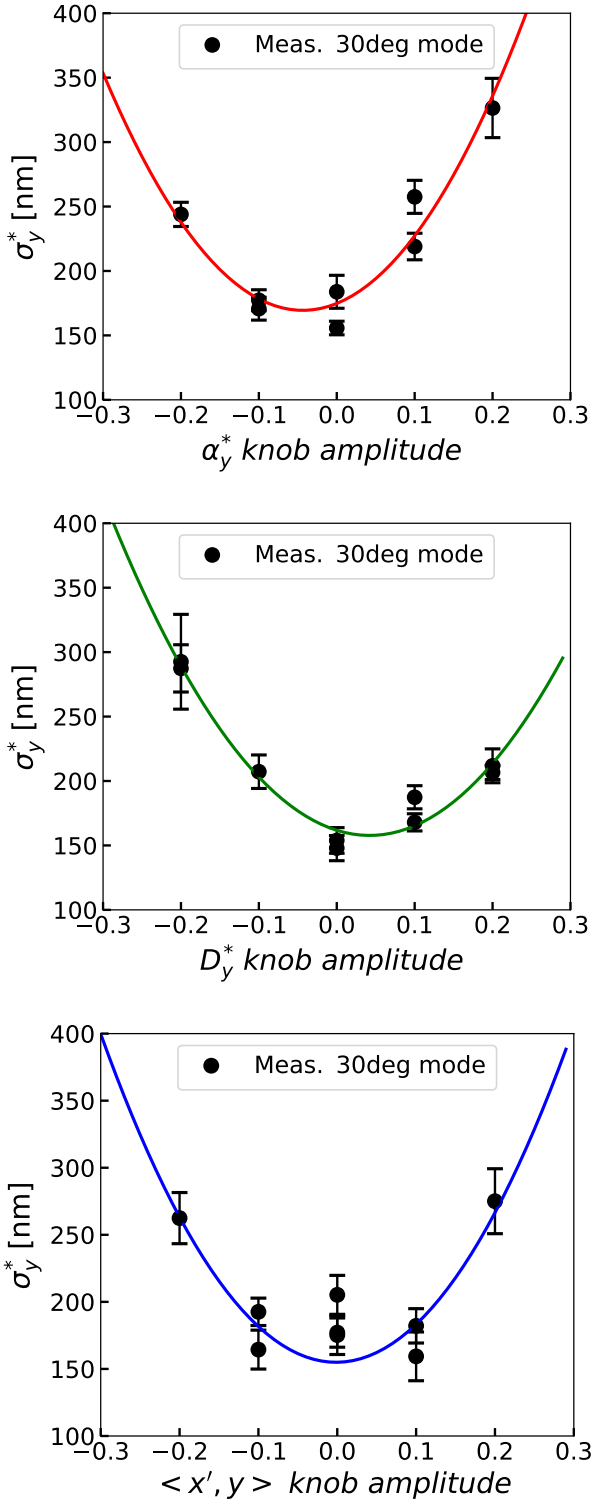

Figure 5.13: Linear Knobs *AY* (α_y^*), *EY* (D_y^*) and *Coup2* ($< x', y >$) scans done during March 2019 operation at 30 degree mode with the Shintake monitor.

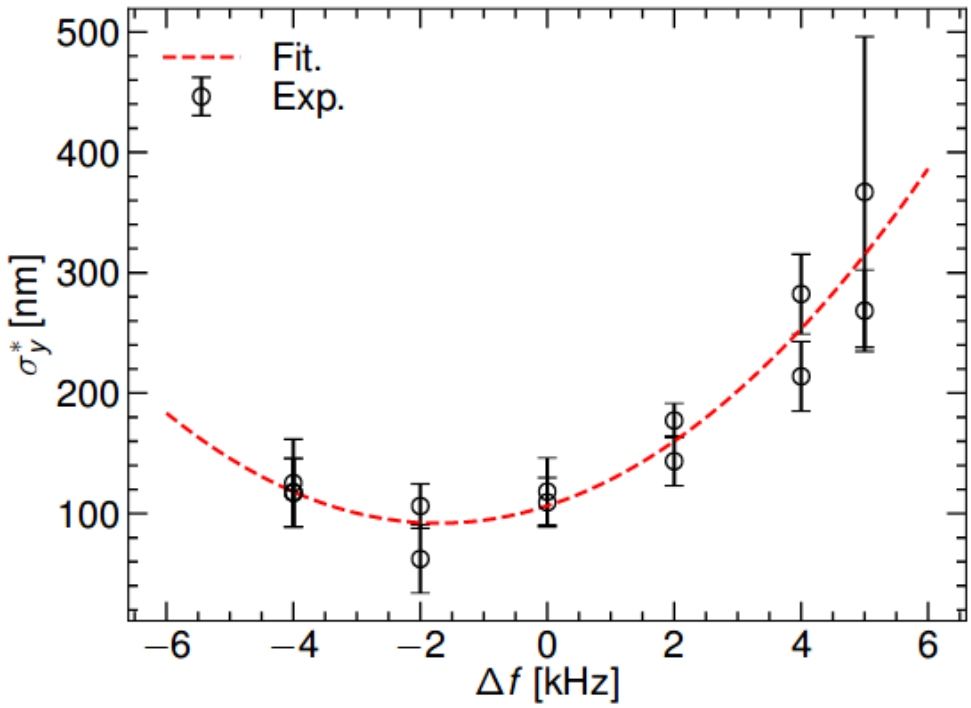

Figure 5.14: Energy dependence (df-knob) scan done during March 2019 run with the vertical beam size at IP considered as a figure of merit.

The rest of the shifts were spent for the beam tuning with IPBSM in 6.4 and 30 degree modes, since 174 degree mode could not be reached in March 2019 operation. Due to that, the use of the ocupoles was limited during March 2019 beam operation since they are expected to be used, when the beam is well tuned in 174 degree mode of the IPBSM, after being properly aligned [20]. The smallest vertical beam size at the IP achieved was 86 ± 14 nm in 30 degree mode (the corresponding modulation was $M \approx 0.76$, see Figure 5.16) after applying linear and Y_{24} and Y_{46} (see Figure 5.15) knobs. A summary table of all the relevant parameters during March 2019 run is shown in Table 5.2. No clear modulation was achieved at 174 degree mode (with $M < 0.1$) since no signal was found with the Z-scan of the Shintake monitor system. To summarize the tuning of the machine, Figure 5.15 shows all the knobs applied during March 2019 operation and the respective vertical beam size and modulation reached.

During the 56 hours of tuning, a total of 3 shifts were lost because of several technical issues: a water leak in the septum, IPBSM laser phase module CPU errors, FD mover drifts, EXT orbit and dispersion drifts because of the temperature change and IPBSM modulation was unstable.

March 2019 run represented the first attempt and the preparation week for the experimental validation of the ultra-low β_y^* optics achieved during June 2019 tuning week. In

Table 5.1: Summary table of the shifts performed in March 2019 beam operation.

Days	Shifts	Objective	Measured Parameters			
			β_x^* [mm]	ε_x^* [nm]	$\frac{\varepsilon_y^*[nm]}{\beta_y^*[mm]}$	M
Wed 13/03	Day	Orbit and dispersion correction, EXT orbit and dispersion drifts	-	-	-	-
	Swing	QF1 and QD0 scans w/ sext. off and on, xy coupling correction, set IPBSM for 6.4 deg mode, FFS mover drifts	82.9 79.9 124.3	1.22 1.16 1.07	0.29 0.29 0.32	-
	Owl	QF1 and QD0 scans, no clear modulation at 6.4 degree mode, septum water leak alarm	-	-	-	-
Thu 14/03	Day	Restart of operation after the water leak, radiation alarm interlock, modulation recovery at 6.4 deg mode, QDO mover problem, phase module system error	96.8	1.56	0.42	-
	Swing	IPBSM problem fixed, clear modulation was found at 6.4 deg mode	-	-	-	-
	Owl	Linear knobs scans at 6.4 deg mode, set IPBSM for 30 deg mode	-	-	-	0.7 (at 6.4 deg mode)
Fri 15/03	Day	Beam size tuning at 30 deg mode, energy dependence study	-	-	-	0.75 (at 30 deg mode)
	Swing	set IPBSM for 174 deg mode, no clear modulation was found, beam off at 19:20	-	-	-	-

Figure 1.23 a summary of the minimum IP vertical beam size achieved in every tuning week from 2012 to 2020 can be seen. In fact, in June 2019 an IP vertical minimum beam size of 50.1 ± 0.6 nm has been obtained during the tuning process. In [48] more detail on the June 2019 tuning week are given. The tuning experiment conducted in June 2019 has demonstrated the capability of achieving over long periods a vertical beam size below 60

Table 5.2: Summary table of the relevant parameters during March 2019 beam operation.

M	β_x^*[mm]	β_y^*[μm]	σ_x^*[μm]	σ_y^*[nm]	ε_x^*[nm]	ε_y^*[pm]
0.76 ± 0.03	80 ± 4	35 ± 2	9.8 ± 1.1	86 ± 14	1.2 ± 0.2	9.9 (DR)

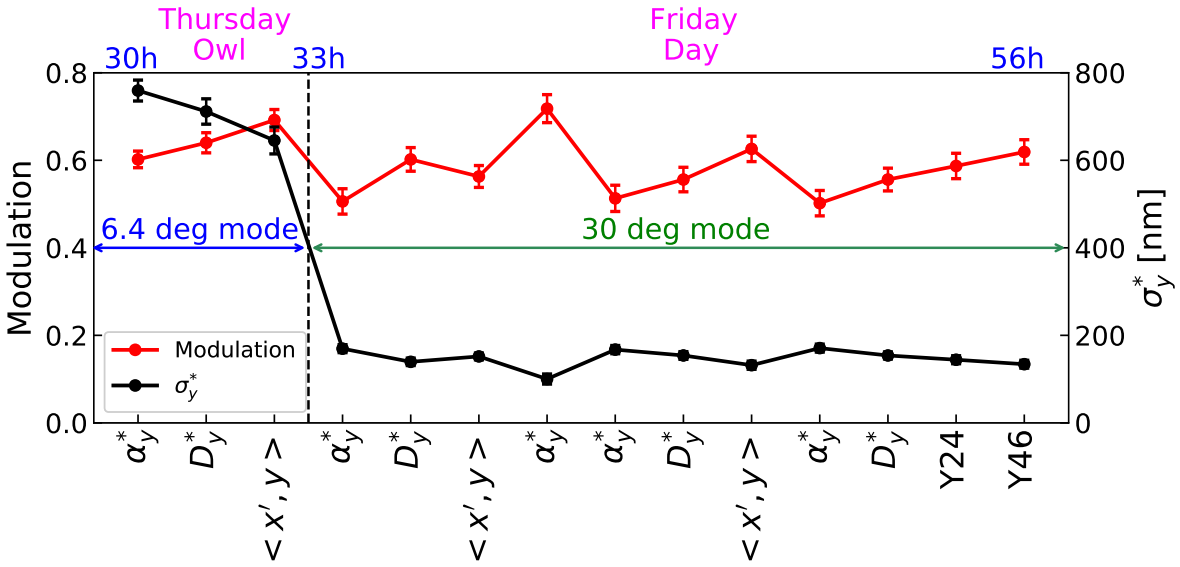

Figure 5.15: Summary of the modulation (in red) and vertical beam size at the IP σ_y^* (in black) for each knob applied during March 2019 operation.

nm. Moreover, these results are comparable to the performances achieved in the nominal optics, $10\beta_x^* \times 1\beta_y^*$ and half-β_y^* optics and represent an important step toward the ultra-low β^* optics with 23 nm design beam size.

The rest of the beam tuning performed in 2019 was used for clarifying the octupoles role in the tuning process and a beam tuning operation week done in March 2020 was used to better understand the potential of the knobs specifically constructed for the ultra-low β_y^* optics and what is the gain they can provide in the terms of tuning effectiveness compared to the knobs presently used on ATF2.

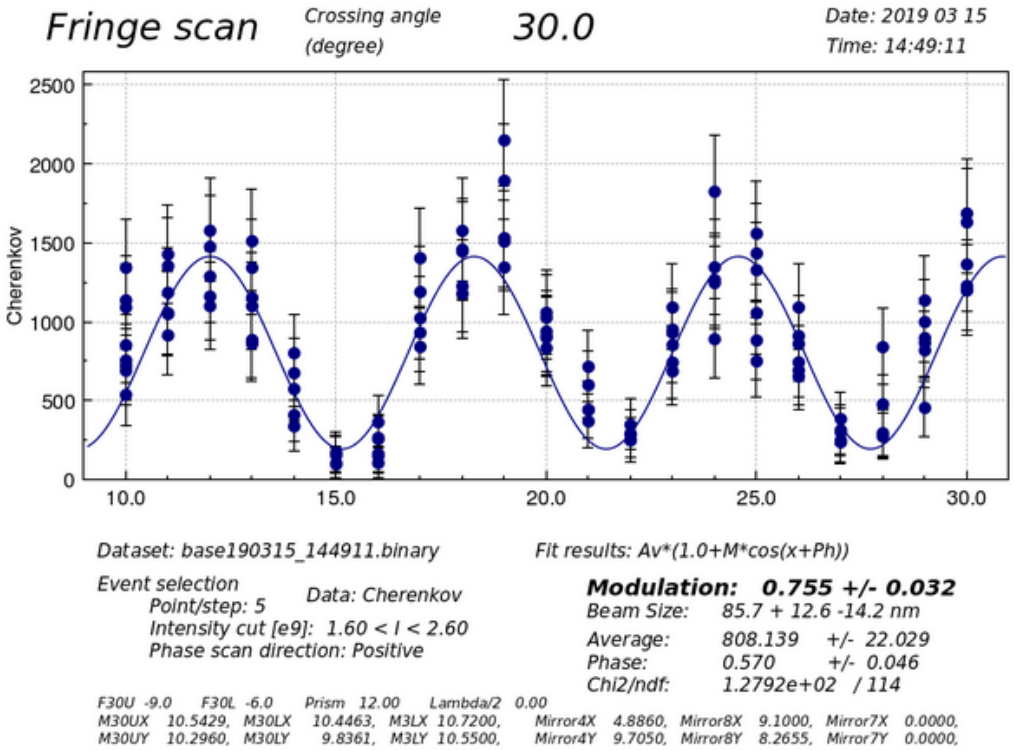

Figure 5.16: Fringe scan for the smallest vertical beam size ($\sigma_y^* = 86 \pm 14$ nm) achieved at ATF2 during March 2019 operation [97].

CHAPTER 6

Conclusions

The novel dual BDS design presented in this thesis work has the potential of making CLIC more competitive versus other future circular collider projects, such as the FCCee and the CepC, by enabling collisions in two detectors.
This PhD leads to a very important results never evaluated before:

- **A complete optics design for the dual BDS layout for both energy stages of CLIC 380 GeV and 3 TeV respectively**. The novel optics design of the dual BDS has been made with the code MAD-X. In order to create a second IR area, bending dipoles have been added at the entrance of the DS, to separate the beams at the exit of the ML, trying to minimize the length of the added section. The optics of the DS has been rematched to the rest of the BDS in order to keep its performance. The complete system have 2 IRs known as **IR1 and IR2 with 16.5 and 26 mrad crossing angle respectively for CLIC 380 GeV and with 20 mrad and 25.5 mrad crossing angle respectively for CLIC 3 TeV**. Four different BDS systems at either side of the two IPs (BDS1 $e^{\pm}$ and BDS2 $e^{\pm}$) have been designed in order to have different DS lengths to provide the desired longitudinal and transverse separations at the IP to have enough space to allocate the two detectors caverns.

- **The impact of the solenoidal field on the luminosity performance for the CLIC 3 TeV**. This has been evaluated for the current CLIC design with L*= 6 m (QD0 outside the detector) using GUINEA-PIG and the PLACET codes and with a special **forward-backward-forward tracking technique** and taking into account other effects as the beamstrhalung or the SR. These calculations give a negligible effect at 380 GeV and at 3 TeV has been found to be $\approx 4\%$ in good agreement with the results obtained for the CDR CLIC 3 TeV design with a L*= 3.5 m.

- **The evaluation of the global performances of the CLIC dual BDS optics at both energy stages**. The evaluation of the beam sizes have been calculated with the

PLACET direct tracking procedure and benchmarked with MAPCLASS and PTC codes showing consistency of results. Then, the detector solenoid effects have been taking into account for the evaluation of the luminosity performance. The impact on CLIC 380 GeV is negligible considering all the effects, including the detector solenoid field. For CLIC 3 TeV instead, the impact on the luminosity performance for the detector solenoid field is about 4% for the dual CLIC BDS1 and about 19% for the dual CLIC BDS2. This represents the total luminosity loss that cannot be corrected once the design is fixed. Considering all effects together there is in total a luminosity performance loss from the baseline design for the CLIC 3 TeV of about 2% at the IR1 and about 33% of luminosity performance loss at the IR2, both with respect to the previous design but including the solenoid. In order to mitigate these effects, the possibility to add an anti-solenoid for the CLIC 3 TeV case in order to increase the luminosity performance of the CLIC dual BDS1 design at the level of the current CLIC baseline (L*= 6 m). A simulation with the new design but with the SiD experiment configuration that includes the anti-solenoid has been done. The results show a decrease of the luminosity losses from about 4% to about 1% and leads to the same luminosity performances in the case of the baseline design and the dual CLIC BDS1 design. For the dual CLIC BDS2 instead we could not estimate the potential of the anti-solenoid since the magnetic design of the solenoid does not exist for now.

To conclude, we can say that the results obtained can be considered good enough in terms of feasibility to possibly consider **the CLIC dual BDS as a realistic option for CLIC**.

Further improvements can still be performed for the dual BDS layout in order to recover part of the luminosity performance, especially for the BDS2 of the CLIC 3 TeV case. Currently all the DS bendings are placed in BDS2 however this could be distributed between BDS1 and BDS2 (with opposite angles). This would reduce luminosity loss in IR2 and increase it in IR1. Another option could be to do a longer BDS to reduce the impact of the SR in the BDS2, followed by optics improvements of the dual BDS. Furthermore, to try to reduce the impact of the solenoid effects for the BDS2, the anti-solenoid is the best option to cancel a good fraction of luminosity losses. Further studies need also to be addressed to understand even better the real potential of the dual BDS layout. These will involve polarimetry, muon supression and tuning. The tuning in particular has been already studied for the CLIC baseline designs in [46, 47] but no studies since now have been done for the novel dual BDS configuration.

In order to test **the real feasibility tuning operation of a CLIC FFS optics type**, the first experimental work with the ultra-low β_y^* in March 2019 at ATF2 in collaboration with KEK has been performed. During March 2019 the optics was well matched and the Twiss parameters at the IP were close enough to the design values, but unfortunately, the run ended with an incomplete machine tuning because of some technical problems that turned out to be the main limitations for reaching the target of 40 nm vertical beam size at

the IP. In facts, during March 2019 run 7 shifts in total have been allocated for the ultra-low β_y^* optics study. The first 4 shifts were mostly used to correct the orbit, the dispersion, the coupling and then match the β functions at the IP with the wire scanner. The rest of the shifts were spent for the beam tuning with IPBSM Shintake monitor in 6.4 and 30 deg modes. Unfortunately, 174 deg mode Shintake monitor could not be reached in March 2019 operation. The smallest vertical beam size at the IP achieved was 86 ± 14 nm in 30 deg mode Shintake monitor (the corresponding modulation was $M \approx 0.76$) after applying linear and non-linear knobs. During the 56 hours of tuning, a total of 3 shifts were lost because of several technical issues: a water leak in the septum, IPBSM laser phase module CPU errors, FD mover drifts, EXT orbit and dispersion drifts because of the temperature change and IPBSM modulation was unstable. All these technical problems ended to be the main limitation to reach the nanometer vertical beam size at the IP. Anyway, **thanks to this first attempt in March 2019, the performance of the IPBSM Shintake monitor at 174 deg mode was recovered during June 2019 beam operation**.

APPENDIX A

MAD-X Code Implementation to construct the dual CLIC BDS for two IRs

In this Appendix the codes implementation done for the construction of the optics design in MAD-X before and the PLACET tracking code used for the the evaluation of the luminosity performances (done with GUINEA-PIG) of the CLIC dual BDS, after, is reported [98].

A.1 MAD-X Implementation of the novel optics design for the dual CLIC BDS

The implementation of the new optics design for the dual CLIC BDS has been done in MAD-X and in particular modifying the diagnostics section (DS), more detail in Section **??**.

In the following sections the MAD-X code with the DS modification for the construction of the new dual BDS is reported for both CLIC energy stages options.

A.1.1 CLIC 380 GeV

```
DSCALE:=0.5;
mu=70.*pi/180.;
L=39.5;
L2=L*0.55;
beta_max:=L*(1+sin(mu/2.))/sin(mu)*DSCALE;
```

```
beta_min:=L*(1-sin(mu/2.))/sin(mu)*DSCALE;
alpha_max:=(-1-sin(mu/2.))/cos(mu/2.);
alpha_min:=(1-sin(mu/2.))/cos(mu/2.);
f_max:=L/(4*sin(mu/2.));
f_min:=-L/(4*sin(mu/2.));
muL=pi/4.;
beta_maxL=150.0;
LL:=beta_maxL*sin(muL)/(1+sin(muL/2.)); // approx 110 m

kf2 =       0.1033739537/DSCALE/DSCALE ;
kd2 =     -0.08499462268/DSCALE/DSCALE ;
kf3 =      0.05660408062/DSCALE/DSCALE ;
kd3 =     -0.07925837696/DSCALE/DSCALE ;
kf4 =       0.1039004288/DSCALE/DSCALE ;
kd5 =      -0.0553809776/DSCALE/DSCALE ;
kf5 =      0.05764637677/DSCALE/DSCALE ;
kd4 =     -0.08989292421/DSCALE/DSCALE ;
kf6 =      0.02612552684/DSCALE/DSCALE ;
kf7 =       0.0199547435/DSCALE/DSCALE ;
kd7 =      -0.0199547435/DSCALE/DSCALE ;
kd6 =     -0.02002336697/DSCALE/DSCALE ;
kd8 =    -5.19004528E-02/DSCALE/DSCALE;
kd9 =    6.73954265E-02/DSCALE/DSCALE;
kf9 =    -7.62238127E-02/DSCALE/DSCALE;
kf8 =     2.00862619E-02/DSCALE/DSCALE;

f_max =        17.39422833 ;
f_min =       -16.95110903 ;

TQF: quadrupole, l=1*DSCALE, k1:=1./f_max/DSCALE/DSCALE;
TQD: quadrupole, l=2*DSCALE, k1:=1./(2*f_min)/DSCALE/DSCALE;
DD: DRIFT, L:=(L/8.-0.5)*DSCALE;
DD2: DRIFT, L:=(L2/8.-(2./3.))*DSCALE;
TQF2A: quadrupole, l=1*DSCALE, k1:=kf2/2;
TQF2B: quadrupole, l=1*DSCALE, k1:=kf2/2;
TQD2A: quadrupole, l=1*DSCALE, k1:=kd2/2;
TQD2B: quadrupole, l=1*DSCALE, k1:=kd2/2;
TQF3A: quadrupole, l=1*DSCALE, k1:=kf3/2;
TQF3B: quadrupole, l=1*DSCALE, k1:=kf3/2;
TQD3A: quadrupole, l=1*DSCALE, k1:=kd3/2;
TQD3B: quadrupole, l=1*DSCALE, k1:=kd3/2;
TQF4A: quadrupole, l=1*DSCALE, k1:=kf4/2;
```

```
TQF4B: quadrupole, l=1*DSCALE, k1:=kf4/2;
TQD4A: quadrupole, l=1*DSCALE, k1:=kd4/2;
TQD4B: quadrupole, l=1*DSCALE, k1:=kd4/2;
TQF5A: quadrupole, l=1*DSCALE, k1:=kf5/2;
TQF5B: quadrupole, l=1*DSCALE, k1:=kf5/2;
TQD5: quadrupole, l=2*DSCALE, k1:=kd5/2;
DDL: DRIFT, L:=(LL/8.-0.5)*DSCALE;
//DDL2: DRIFT, L:=(((LL/8.-0.5)*DSCALE)/2)+1;
DDL89: DRIFT, L:=(LL/8.-2)*DSCALE;
DDLe: DRIFT, L:=(LL/8.*0.63-2)*DSCALE;
TQF6A: quadrupole, l=1*DSCALE, k1:=kf6/2;
TQF6B: quadrupole, l=1*DSCALE, k1:=kf6/2;
TQF7A: quadrupole, l=1*DSCALE, k1:=kf7/2;
TQF7B: quadrupole, l=1*DSCALE, k1:=kf7/2;
TQD6A: quadrupole, l=1*DSCALE, k1:=kd6/2;
TQD6B: quadrupole, l=1*DSCALE, k1:=kd6/2;
TQD7A: quadrupole, l=1*DSCALE, k1:=kd7/2;
TQD7B: quadrupole, l=1*DSCALE, k1:=kd7/2;
TQF8A: quadrupole, l=1*DSCALE, k1:=kf8/2;
TQF8B: quadrupole, l=1*DSCALE, k1:=kf8/2;
TQD8: quadrupole, l=2*DSCALE, k1:=kd8/2;
TQF9: quadrupole, l=2*DSCALE, k1:=kf9/2;
TQD9: quadrupole, l=2*DSCALE, k1:=kd9/2;
TQF10: quadrupole, l=2*DSCALE, k1:=kf10/2;
TQF11A: quadrupole, l=1*DSCALE, k1:=kf11/2;
TQF11B: quadrupole, l=1*DSCALE, k1:=kf11/2;
TQF12A: quadrupole, l=1*DSCALE, k1:=kf12/2;
TQF12B: quadrupole, l=1*DSCALE, k1:=kf12/2;
TQD11A: quadrupole, l=1*DSCALE, k1:=kd11/2;
TQD11B: quadrupole, l=1*DSCALE, k1:=kd11/2;
TQD12A: quadrupole, l=1*DSCALE, k1:=kd12/2;
TQD12B: quadrupole, l=1*DSCALE, k1:=kd12/2;
TQF13A: quadrupole, l=1*DSCALE, k1:=kf13/2;
TQF13B: quadrupole, l=1*DSCALE, k1:=kf13/2;
TQD13A: quadrupole, l=1*DSCALE, k1:=kd13/2;
TQD13B: quadrupole, l=1*DSCALE, k1:=kd13/2;
TQF14A: quadrupole, l=1*DSCALE, k1:=kf14/2;
TQF14B: quadrupole, l=1*DSCALE, k1:=kf14/2;
TQD14A: quadrupole, l=1*DSCALE, k1:=kd14/2;
TQD14B: quadrupole, l=1*DSCALE, k1:=kd14/2;
TQF15A: quadrupole, l=1*DSCALE, k1:=kf15/2;
TQF15B: quadrupole, l=1*DSCALE, k1:=kf15/2;
```

```
TQD15A: quadrupole, l=1*DSCALE, k1:=kd15/2;
TQD15B:quadrupole,l=1*DSCALE, k1:=kd15/2;
TQF16A: quadrupole, l=1*DSCALE, k1:=kf16/2;
TQF16B: quadrupole, l=1*DSCALE, k1:=kf16/2;
TQD16A: quadrupole, l=1*DSCALE, k1:=kd16/2;
TQD16B: quadrupole, l=1*DSCALE, k1:=kd16/2;
TQF17A: quadrupole, l=1*DSCALE, k1:=kf17/2;
TQF17B: quadrupole, l=1*DSCALE, k1:=kf17/2;
TQD17A: quadrupole, l=1*DSCALE, k1:=kd17/2;
TQD17B: quadrupole, l=1*DSCALE, k1:=kd17/2;
TQF18A: quadrupole, l=1*DSCALE, k1:=kf18/2;
TQF18B: quadrupole, l=1*DSCALE, k1:=kf18/2;
TQD18A: quadrupole, l=1*DSCALE, k1:=kd18/2;
TQD18B: quadrupole, l=1*DSCALE, k1:=kd18/2;
TQF19A: quadrupole, l=1*DSCALE, k1:=kf19/2;
TQF19B: quadrupole, l=1*DSCALE, k1:=kf19/2;
TQD19A: quadrupole, l=1*DSCALE, k1:=kd19/2;
TQD19B: quadrupole, l=1*DSCALE, k1:=kd19/2;
DDL2: DRIFT, L:=4.16;
M1: MARKER;
M2: MARKER;

stheta=0.0004905;
//stheta=0.000;
DDLB: SBEND, L:=(LL/8.-0.5)*DSCALE, ANGLE:=stheta/4;
DDLA: SBEND, L:=(LL/8.-0.5)*DSCALE, ANGLE:=stheta/sqrt(2)/4;
DDL0: DRIFT, L:=(LL/8.-0.5)*DSCALE;

// BDS1 e- (longer option no dipoles)

DIAGNOSTICS: LINE:=(TQF ,DD ,DD ,DD ,DD ,TQD ,DD ,DD ,DD ,DD,
TQF2A ,TQF2B, DD2 , DD2 ,DD2 ,TQD2A, TQD2B, DD2 ,DD2 ,DD2 , TQF3A,
TQF3B, DD2 ,DD2 ,DD2 ,TQD3A, TQD3B, DD2,DD2 ,DD2, TQF4A, TQF4B,
DD ,DD , DD ,DD, TQD4A, TQD4B, DD,DD,DD ,DD, TQF5A, TQF5B,
DD , DD ,DD ,DD ,TQD5 ,DDL ,DDL ,DDL ,DDL ,TQF6A, TQF6B,
DDL, DDL ,DDL ,DDL ,TQD6A , TQD6B ,DDL ,DDL ,DDL ,DDL ,TQF7A ,
TQF7B , DDL ,DDL ,DDL ,DDL ,TQD7A ,TQD7B ,DDL ,DDL, DDL ,DDL ,
TQF11A, TQF11B, DDL0 ,DDL0 ,DDL0 ,DDL0 ,TQD11A , TQD11B ,DDL0, DDL0 ,DDL0 ,
DDL0 ,TQF12A , TQF12B , DDL0 ,DDL0 ,DDL0 ,DDL0 ,TQD12A ,TQD12B ,DDL0 ,DDL0,
DDL0 ,DDL0 , TQF13A, TQF13B, DDL0 ,DDL0 ,DDL0 ,DDL0 ,TQD13A , TQD13B ,DDL0 ,
DDL0 ,DDL0 ,DDL0 ,TQF14A , TQF14B , DDL0 ,DDL0 ,DDL0 ,DDL0 ,TQD14A ,TQD14B ,
DDL0 ,DDL0, DDL0 ,DDL0 , TQF15A, TQF15B , DDL0 ,DDL0 ,DDL0 ,DDL0 ,TQD15A ,
```

```
TQD15B,DDL0 ,DDL0 ,DDL0 ,DDL0 , TQF16A , TQF16B , DDL0 ,DDL0 ,DDL0 ,DDL0,
TQD16A ,TQD16B , DDL0 ,DDL0, DDL0 ,DDL0 , TQF17A, TQF17B, DDL0 ,DDL0 ,DDL0 ,
DDL0 ,TQD17A , TQD17B ,DDL0 ,DDL0 ,DDL0 ,DDL0 , TQF18A , TQF18B , DDL0 ,DDL0 ,
DDL0 ,DDL0 ,TQD18A ,TQD18B, DDL0 ,DDL0, DDL0 ,DDL0 ,TQF19A, TQF19B ,
DDL0 ,
DDL0 ,DDL0 ,DDL0 ,TQD19A ,TQD19B , DDL0 ,DDL0, DDL0 ,DDL0 , TQF8A, TQF8B,
DDL ,DDL ,DDL ,DDL, TQD8, DDL89, TQF9, DDLe, TQD9);


//BDS1 e+ (shorter option no dipoles)

DIAGNOSTICS: LINE:=(TQF ,DD ,DD ,DD ,DD ,TQD ,DD ,DD ,DD ,
DD, TQF2A ,TQF2B, DD2 ,DD2 ,DD2 ,TQD2A, TQD2B, DD2 ,DD2 ,DD2 ,
TQF3A, TQF3B, DD2 ,DD2 ,DD2 ,TQD3A, TQD3B, DD2,DD2 ,DD2, TQF4A,
TQF4B, DD ,DD ,DD ,DD, TQD4A, TQD4B, DD,DD,DD ,DD,
TQF5A, TQF5B, DD ,DD ,DD ,DD ,TQD5 ,DDL ,DDL ,DDL ,DDL,
TQF6A, TQF6B, DDL ,DDL ,DDL ,DDL ,TQD6A , TQD6B ,DDL ,DDL ,DDL ,
DDL ,TQF7A , TQF7B , DDL ,DDL ,DDL ,DDL ,TQD7A ,TQD7B ,DDL ,DDL,
DDL ,DDL , TQF11A, TQF11B,
DDL0 ,DDL0 ,DDL0 ,DDL0 ,TQD11A , TQD11B ,DDL0,
DDL0 ,DDL0 ,DDL0 ,TQF12A , TQF12B , DDL0 ,DDL0 ,DDL0 ,DDL0 ,TQD12A ,TQD12B ,
DDL0 ,DDL0, DDL0 ,DDL0 , TQF13A, TQF13B,
DDL0 ,DDL0 ,DDL0 ,DDL0 ,TQD13A ,
TQD13B ,DDL0 ,DDL0 ,DDL0 ,DDL0 ,TQF14A , TQF14B ,
DDL0 ,DDL0 ,DDL0 ,DDL0,
TQD14A ,TQD14B , DDL0 ,DDL0, DDL0 ,DDL0 , TQF15A, TQF15B , DDL0 ,DDL0 ,DDL0 ,
DDL0 ,TQD15A , TQD15B,DDL0 ,DDL0 ,DDL0 ,DDL0 , TQF16A , TQF16B , DDL0 ,DDL0 ,
DDL0 ,DDL0 ,TQD16A ,TQD16B , DDL0 ,DDL0, DDL0 ,DDL0 , TQF17A, TQF17B, DDL0 ,
DDL0 ,DDL0 ,DDL0 ,TQD17A , TQD17B ,DDL0 ,DDL0 ,DDL0 ,DDL0 , TQF18A , TQF18B ,
DDL0 ,DDL0 ,DDL0 ,DDL0 ,TQD18A ,TQD18B, DDL0 ,DDL0, DDL0 ,DDL0 , TQF8A,
TQF8B,DDL ,DDL ,DDL ,DDL, TQD8, DDL89, TQF9, DDLe, TQD9);

//BDS2 e+ (longer option with dipoles)

DIAGNOSTICS: LINE:=(TQF ,DD ,DD ,DD ,DD ,TQD ,DD ,DD ,DD ,DD, TQF2A ,
TQF2B, DD2 ,DD2 ,DD2 ,TQD2A, TQD2B, DD2 ,DD2 ,DD2 , TQF3A, TQF3B, DD2,
DD2 ,DD2 ,TQD3A, TQD3B, DD2,DD2 ,DD2, TQF4A, TQF4B, DD ,DD ,DD ,DD,
TQD4A, TQD4B, DD,DD,DD ,DD, TQF5A, TQF5B, DD ,DD ,DD ,DD ,TQD5 , DDL,
DDL ,DDL ,DDL ,TQF6A, TQF6B, DDL ,DDL ,DDL ,DDL ,TQD6A , TQD6B ,DDL,
DDL ,DDL ,DDL ,TQF7A , TQF7B , DDL ,DDL ,DDL ,DDL ,TQD7A ,TQD7B , DDL,
DDL, DDL ,DDL , TQF11A, TQF11B,
DDLA ,DDLA ,DDLA ,DDLA ,TQD11A , TQD11B ,DDLA ,DDLA ,DDLA ,DDLA ,
```

```
TQF12A , TQF12B , DDLA ,DDLA ,DDLA ,DDLA , TQD12A ,TQD12B ,DDLA ,
DDLA, DDLA ,DDLA ,TQF13A, TQF13B, DDL0 ,DDL0 ,
DDL0 ,DDL0 ,TQD13A , TQD13B ,DDL0 ,DDL0,
DDL0 ,DDL0 ,TQF14A , TQF14B , DDLB ,DDLB ,DDLB ,DDLB ,TQD14A ,TQD14B ,
DDLB ,DDLB, DDLB ,DDLB , TQF15A, TQF15B , DDLB ,DDLB ,DDLB ,DDLB ,
TQD15A , TQD15B, DDLB ,DDLB ,DDLB ,DDLB , TQF16A , TQF16B , DDL0,
DDL0 ,DDL0 ,DDL0 ,TQD16A ,TQD16B , DDL0 ,DDL0, DDL0 ,DDL0 , TQF17A,
TQF17B, DDLA ,DDLA ,DDLA ,DDLA ,TQD17A , TQD17B ,DDLA ,DDLA ,DDLA,
DDLA , TQF18A , TQF18B , DDLA ,DDLA ,DDLA ,DDLA ,TQD18A ,TQD18B,
DDLA ,DDLA, DDLA ,DDLA ,TQF19A, TQF19B , DDL0 ,DDL0 ,DDL0 ,DDL0 ,
TQD19A ,TQD19B , DDL0 ,DDL0, DDL0 ,DDL0 , TQF8A, TQF8B,
DDL ,DDL ,DDL ,DDL, TQD8, DDL89, TQF9, DDLe, TQD9);

//BDS2 e- (shorter option with dipoles)

DIAGNOSTICS: LINE:=(TQF ,DD ,DD ,DD ,DD ,TQD ,DD ,DD ,DD ,DD, TQF2A ,
TQF2B, DD2 ,DD2 ,DD2 ,TQD2A, TQD2B, DD2 ,DD2 ,DD2 , TQF3A, TQF3B, DD2,
DD2 ,DD2 ,TQD3A, TQD3B, DD2,DD2 ,DD2, TQF4A, TQF4B, DD ,DD ,DD ,DD,
TQD4A, TQD4B, DD,DD,DD ,DD, TQF5A, TQF5B, DD ,DD ,DD ,DD ,TQD5 ,DDL,
DDL ,DDL ,DDL ,TQF6A, TQF6B, DDL ,DDL ,DDL ,DDL ,TQD6A , TQD6B ,DDL,
DDL ,DDL ,DDL ,TQF7A , TQF7B , DDL ,DDL ,DDL ,DDL ,TQD7A ,TQD7B ,DDL,
DDL, DDL ,DDL , TQF11A, TQF11B,
DDLA ,DDLA ,DDLA ,DDLA ,TQD11A , TQD11B ,DDLA ,DDLA ,DDLA ,DDLA ,
TQF12A , TQF12B , DDLA ,DDLA ,DDLA ,DDLA ,TQD12A ,TQD12B ,DDLA ,DDLA,
DDLA ,DDLA ,TQF13A, TQF13B, DDL0 ,DDL0 ,DDL0 ,DDL0 ,TQD13A , TQD13B ,
DDL0 ,DDL0,DDL0 ,DDL0 ,TQF14A , TQF14B , DDL0 ,DDL0 ,DDL0 ,DDL0,
TQD14A , TQD14B ,DDL0 ,DDL0 ,DDL0 ,DDL0 ,TQF15A , TQF15B , DDLA ,
DDLA ,DDLA ,DDLA ,TQD15A,TQD15B , DDLA ,DDLA, DDLA ,DDLA , TQF16A,
TQF16B , DDLA, DDLA ,DDLA ,DDLA ,TQD16A , TQD16B, DDLA ,
DDLA ,DDLA ,DDLA , TQF8A ,TQF8B , DDL ,DDL ,DDL ,DDL, TQD8, DDL89,
TQF9, DDLe, TQD9);
```

A.1.2 CLIC 3 TeV

```
mu=70.*pi/180.;
L=39.5;
L2=L*0.55;
beta_max:=L*(1+sin(mu/2.))/sin(mu);
beta_min:=L*(1-sin(mu/2.))/sin(mu);
alpha_max:=(-1-sin(mu/2.))/cos(mu/2.);
```

```
alpha_min:=(1-sin(mu/2.))/cos(mu/2.);
f_max:=L/(4*sin(mu/2.));
f_min:=-L/(4*sin(mu/2.));


muL=pi/4.;
beta_maxL=150.0; !To get 1mu at the laser wires with emit_y=20nm
LL:=beta_maxL*sin(muL)/(1+sin(muL/2.)); ! approx 110 m

kf2 =       0.1033739537 ;
kd2 =     -0.08499462268 ;
kf3 =      0.05660408062 ;
kd3 =     -0.07925837696 ;
kf4 =       0.1039004288 ;
kd5 =      -0.0553809776 ;
kf5 =      0.05764637677 ;
kd4 =     -0.08989292421 ;
kf6 =      0.02612552684 ;
kf7 =       0.0199547435 ;
kd7 =      -0.0199547435 ;
kd6 =     -0.02002336697 ;


kd8     =                  -5.19004528E-02;
kd9      =                  6.73954265E-02;
kf9       =                -7.62238127E-02;
kf8        =                2.00862619E-02;

f_max =        17.39422833 ;
f_min =       -16.95110903 ;




TQF: quadrupole, l=1, k1:=1./f_max, APERTURE:=AP_min;
TQD: quadrupole, l=2, k1:=1./(2*f_min), APERTURE:=AP_min;
DD: DRIFT, L:=L/8.-0.5;
DD2: DRIFT, L:=L2/8.-(2./3.);
TQF2A: quadrupole, l=1, k1:=kf2/2, APERTURE:=AP_min;
TQF2B: quadrupole, l=1, k1:=kf2/2, APERTURE:=AP_min;
TQD2A: quadrupole, l=1, k1:=kd2/2, APERTURE:=AP_min;
TQD2B: quadrupole, l=1, k1:=kd2/2, APERTURE:=AP_min;
```

```
TQF3A: quadrupole, l=1, k1:=kf3/2, APERTURE:=AP_min;
TQF3B: quadrupole, l=1, k1:=kf3/2, APERTURE:=AP_min;
TQD3A: quadrupole, l=1, k1:=kd3/2, APERTURE:=AP_min;
TQD3B: quadrupole, l=1, k1:=kd3/2, APERTURE:=AP_min;
TQF4A: quadrupole, l=1, k1:=kf4/2, APERTURE:=AP_min;
TQF4B: quadrupole, l=1, k1:=kf4/2, APERTURE:=AP_min;
TQD4A: quadrupole, l=1, k1:=kd4/2, APERTURE:=AP_min;
TQD4B: quadrupole, l=1, k1:=kd4/2, APERTURE:=AP_min;
TQF5A: quadrupole, l=1, k1:=kf5/2, APERTURE:=AP_min;
TQF5B: quadrupole, l=1, k1:=kf5/2, APERTURE:=AP_min;
TQD5: quadrupole, l=2, k1:=kd5/2, APERTURE:=AP_min;
DDL: DRIFT, L:=LL/8.-0.5;
DDL89: DRIFT, L:=LL/8.-2;
DDLe: DRIFT, L:=LL/8.*0.63-2;   //0.45968487E-01
TQF6A: quadrupole, l=1, k1:=kf6/2, APERTURE:=AP_min;
TQF6B: quadrupole, l=1, k1:=kf6/2, APERTURE:=AP_min;
TQF7A: quadrupole, l=1, k1:=kf7/2, APERTURE:=AP_min;
TQF7B: quadrupole, l=1, k1:=kf7/2, APERTURE:=AP_min;
TQD6A: quadrupole, l=1, k1:=kd6/2, APERTURE:=AP_min;
TQD6B: quadrupole, l=1, k1:=kd6/2, APERTURE:=AP_min;
TQD7A: quadrupole, l=1, k1:=kd7/2, APERTURE:=AP_min;
TQD7B: quadrupole, l=1, k1:=kd7/2, APERTURE:=AP_min;
TQF8A: quadrupole, l=1, k1:=kf8/2, APERTURE:=AP_min;
TQF8B: quadrupole, l=1, k1:=kf8/2, APERTURE:=AP_min;
TQD8: quadrupole, l=2, k1:=kd8/2, APERTURE:=AP_min;
TQF9: quadrupole, l=2, k1:=kf9/2, APERTURE:=AP_min;
TQD9: quadrupole, l=2, k1:=kd9/2, APERTURE:=AP_min;
TQF10: quadrupole, l=2, k1:=kf10/2, APERTURE:=AP_min;
TQF11A: quadrupole, l=1, k1:=kf11/2;
TQF11B: quadrupole, l=1, k1:=kf11/2;
TQF12A: quadrupole, l=1, k1:=kf12/2;
TQF12B: quadrupole, l=1, k1:=kf12/2;
TQD11A: quadrupole, l=1, k1:=kd11/2;
TQD11B: quadrupole, l=1, k1:=kd11/2;
TQD12A: quadrupole, l=1, k1:=kd12/2;
TQD12B: quadrupole, l=1, k1:=kd12/2;
TQF13A: quadrupole, l=1, k1:=kf13/2;
TQF13B: quadrupole, l=1, k1:=kf13/2;
TQD13A: quadrupole, l=1, k1:=kd13/2;
TQD13B: quadrupole, l=1, k1:=kd13/2;
TQF14A: quadrupole, l=1, k1:=kf14/2;
TQF14B: quadrupole, l=1, k1:=kf14/2;
```

```
TQD14A: quadrupole, l=1, k1:=kd14/2;
TQD14B: quadrupole, l=1, k1:=kd14/2;
TQF15A: quadrupole, l=1, k1:=kf15/2;
TQF15B: quadrupole, l=1, k1:=kf15/2;
TQD15A: quadrupole, l=1, k1:=kd15/2;
TQD15B: quadrupole, l=1, k1:=kd15/2;
TQF16A: quadrupole, l=1, k1:=kf16/2;
TQF16B: quadrupole, l=1, k1:=kf16/2;
TQD16A: quadrupole, l=1, k1:=kd16/2;
TQD16B: quadrupole, l=1, k1:=kd16/2;
TQF17A: quadrupole, l=1, k1:=kf17/2;
TQF17B: quadrupole, l=1, k1:=kf17/2;
TQD17A: quadrupole, l=1, k1:=kd17/2;
TQD17B: quadrupole, l=1, k1:=kd17/2;
TQF18A: quadrupole, l=1, k1:=kf18/2;
TQF18B: quadrupole, l=1, k1:=kf18/2;
TQD18A: quadrupole, l=1, k1:=kd18/2;
TQD18B: quadrupole, l=1, k1:=kd18/2;
TQF19A: quadrupole, l=1, k1:=kf19/2;
TQF19B: quadrupole, l=1, k1:=kf19/2;
TQD19A: quadrupole, l=1, k1:=kd19/2;
TQD19B: quadrupole, l=1, k1:=kd19/2;
TQF20A: quadrupole, l=1, k1:=kf20/2;
TQF20B: quadrupole, l=1, k1:=kf20/2;
TQD20A: quadrupole, l=1, k1:=kd20/2;
TQD20B: quadrupole, l=1, k1:=kd20/2;
TQF21A: quadrupole, l=1, k1:=kf21/2;
TQF21B: quadrupole, l=1, k1:=kf21/2;
TQD21A: quadrupole, l=1, k1:=kd21/2;
TQD21B: quadrupole, l=1, k1:=kd21/2;
TQF22A: quadrupole, l=1, k1:=kf22/2;
TQF22B: quadrupole, l=1, k1:=kf22/2;
TQD22A: quadrupole, l=1, k1:=kd22/2;
TQD22B: quadrupole, l=1, k1:=kd22/2;
TQF23A: quadrupole, l=1, k1:=kf23/2;
TQF23B: quadrupole, l=1, k1:=kf23/2;
TQD23A: quadrupole, l=1, k1:=kd23/2;
TQD23B: quadrupole, l=1, k1:=kd23/2;
TQF24A: quadrupole, l=1, k1:=kf24/2;
TQF24B: quadrupole, l=1, k1:=kf24/2;
TQD24A: quadrupole, l=1, k1:=kd24/2;
TQD24B: quadrupole, l=1, k1:=kd24/2;
```

```
TQF25A: quadrupole, l=1, k1:=kf25/2;
TQF25B: quadrupole, l=1, k1:=kf25/2;
TQD25A: quadrupole, l=1, k1:=kd25/2;
TQD25B: quadrupole, l=1, k1:=kd25/2;
TQF26A: quadrupole, l=1, k1:=kf26/2;
TQF26B: quadrupole, l=1, k1:=kf26/2;
TQD26A: quadrupole, l=1, k1:=kd26/2;
TQD26B: quadrupole, l=1, k1:=kd26/2;
TQF27A: quadrupole, l=1, k1:=kf27/2;
TQF27B: quadrupole, l=1, k1:=kf27/2;
TQD27A: quadrupole, l=1, k1:=kd27/2;
TQD27B: quadrupole, l=1, k1:=kd27/2;
TQF28A: quadrupole, l=1, k1:=kf28/2;
TQF28B: quadrupole, l=1, k1:=kf28/2;
TSF1: sextupole, l=0.5, k2:=ks1;
TSF2: sextupole, l=0.5, k2:=ks1;
TSD1: sextupole, l=0.5, k2:=ks2;
TSD2: sextupole, l=0.5, k2:=ks2;

stheta=0.0001316; //for the longer option
//stheta=0.000146; //for the shorter option
//stheta=0.000;

DDLB: SBEND, L:=(LL/8.-0.5), ANGLE:=stheta/4;
DDLA: SBEND, L:=(LL/8.-0.5), ANGLE:=stheta/sqrt(2)/4;
DDL0: DRIFT, L:=(LL/8.-0.5);

//DS current baseline

DIAGNOSTICS: LINE:=(TQF ,DD ,DD ,DD ,DD ,TQD ,DD ,DD ,DD ,DD,
TQF2A ,TQF2B, DD2 ,DD2 ,DD2 ,TQD2A, TQD2B, DD2 ,DD2 ,DD2 , TQF3A,
TQF3B, DD2 ,DD2 ,DD2 ,TQD3A, TQD3B, DD2,DD2 ,DD2, TQF4A, TQF4B, DD ,
DD ,DD ,DD, TQD4A, TQD4B, DD,DD,DD ,DD, TQF5A, TQF5B, DD ,DD ,DD ,DD,
TQD5 ,DDL ,DDL ,DDL ,DDL ,TQF6A, TQF6B, ,DDL ,DDL ,DDL ,DDL ,TQD6A ,
TQD6B,DDL ,DDL ,DDL ,DDL ,TQF7A , TQF7B , DDL ,DDL ,DDL ,DDL ,
TQD7A,TQD7B ,DDL ,DDL, DDL ,DDL ,TQF8A, TQF8B ,DDL ,DDL ,DDL ,DDL,
TQD8, DDL89, TQF9, DDLe, TQD9);

//BDS1 e- (shorter option no dipoles)

DIAGNOSTICS: LINE:=(TQF ,DD ,DD ,DD ,DD ,TQD ,DD ,DD ,DD ,DD,
TQF2A ,TQF2B, DD2 ,DD2 ,DD2 ,TQD2A, TQD2B, DD2 ,DD2 ,DD2,
```

```
TQF3A, TQF3B, DD2 ,DD2 ,DD2 ,TQD3A, TQD3B, DD2,DD2 ,DD2,
TQF4A, TQF4B, DD ,DD ,DD ,DD, TQD4A, TQD4B, DD,DD,
DD ,DD, TQF5A, TQF5B, DD ,DD ,DD ,DD ,TQD5 ,DDL ,
DDL ,DDL ,DDL ,TQF6A, TQF6B, DDL ,DDL ,DDL ,DDL ,TQD6A ,
TQD6B ,DDL ,DDL ,DDL ,DDL ,TQF7A , TQF7B , DDL ,DDL ,DDL ,
DDL ,TQD7A ,TQD7B ,DDL ,DDL, DDL ,DDL , TQF11A, TQF11B, DDL0 ,
DDL0 ,DDL0 ,DDL0 ,TQD11A , TQD11B ,DDL0 ,DDL0 ,DDL0 ,DDL0 ,TQF12A ,
TQF12B , DDL0 ,DDL0 ,DDL0 ,DDL0 ,TQD12A ,TQD12B ,DDL0 ,DDL0, DDL0 ,
DDL0 , TQF13A, TQF13B,  DDL0 ,DDL0 ,DDL0 ,DDL0 ,TQD13A , TQD13B ,DDL0 ,
DDL0 ,DDL0 ,DDL0 ,TQF14A , TQF14B , DDL0 ,DDL0 ,DDL0 ,DDL0 ,TQD14A ,
TQD14B ,DDL0 ,DDL0, DDL0 ,DDL0 , TQF15A, TQF15B,
DDL0 ,DDL0 ,DDL0 ,
DDL0 ,TQD15A , TQD15B ,DDL0 ,DDL0 ,DDL0 ,DDL0 ,TQF16A , TQF16B , DDL0 ,
DDL0 ,DDL0 ,DDL0 ,TQD16A ,TQD16B , DDL0 ,DDL0, DDL0 ,DDL0 , TQF17A,
TQF17B , DDL0 ,DDL0 ,DDL0 ,DDL0 ,TQD17A , TQD17B,DDL0 ,DDL0 ,DDL0 ,
DDL0 , TQF18A , TQF18B , DDL0 ,DDL0 ,DDL0 ,DDL0 ,TQD18A ,TQD18B , DDL0 ,
DDL0, DDL0 ,DDL0 , TQF19A, TQF19B , DDL0 ,DDL0 ,DDL0 ,DDL0 ,TQD19A ,
TQD19B,DDL0 ,DDL0 ,DDL0 ,DDL0 , TQF20A , TQF20B , DDL0 ,DDL0 ,DDL0 ,DDL0 ,
TQD20A ,TQD20B , DDL0 ,DDL0, DDL0 ,DDL0 , TQF21A, TQF21B, DDL0 ,DDL0 ,
DDL0 ,DDL0 ,TQD21A , TQD21B ,DDL0 ,DDL0 ,DDL0 ,DDL0 , TQF22A , TQF22B ,
DDL0 ,DDL0 ,DDL0 ,DDL0 ,TQD22A ,TQD22B, DDL0 ,DDL0, DDL0 ,DDL0 ,
TQF23A, TQF23B ,DDL0 ,DDL0 ,DDL0 ,DDL0 ,TQD23A , TQD23B ,DDL0 ,DDL0 ,
DDL0 ,DDL0 , TQF24A , TQF24B , DDL0 ,DDL0 ,DDL0 ,DDL0 ,TQD24A ,TQD24B,
DDL0 ,DDL0, DDL0 ,DDL0 , TQF8A, TQF8B,DDL ,DDL ,DDL ,
DDL, TQD8, DDL89, TQF9, DDLe, TQD9);

//BDS1 e+ (longer option no dipoles)

DIAGNOSTICS: LINE:=(TQF ,DD ,DD ,DD ,DD ,TQD ,DD ,DD ,DD ,DD,
TQF2A ,TQF2B, DD2 ,DD2 ,DD2 ,TQD2A, TQD2B, DD2 ,DD2 ,DD2 ,
TQF3A, TQF3B, DD2 ,DD2 ,DD2 ,TQD3A, TQD3B, DD2,DD2 ,DD2,
TQF4A, TQF4B, DD ,DD ,DD ,DD, TQD4A, TQD4B, DD,DD,DD ,
DD, TQF5A, TQF5B, DD ,DD ,DD ,DD ,TQD5 ,DDL ,DDL ,
DDL ,DDL ,TQF6A, TQF6B, DDL ,DDL ,DDL ,DDL ,TQD6A , TQD6B ,
DDL ,DDL ,DDL ,DDL ,TQF7A , TQF7B , DDL ,DDL ,DDL ,DDL ,
TQD7A ,TQD7B ,DDL ,DDL, DDL ,DDL , TQF11A, TQF11B, DDL0 ,DDL0 ,
DDL0 ,DDL0 ,TQD11A , TQD11B ,DDL0 ,DDL0 ,DDL0 ,DDL0 ,TQF12A , TQF12B ,
DDL0 ,DDL0 ,DDL0 ,DDL0 ,TQD12A ,TQD12B ,DDL0 ,DDL0, DDL0 ,DDL0 ,
TQF13A, TQF13B, DDL0 ,DDL0 ,DDL0 ,DDL0 ,TQD13A , TQD13B ,DDL0 ,DDL0 ,
DDL0 ,DDL0 ,TQF14A , TQF14B , DDL0 ,DDL0 ,DDL0 ,DDL0 ,TQD14A ,TQD14B ,
DDL0 ,DDL0, DDL0 ,DDL0 , TQF15A, TQF15B, DDL0 ,DDL0 ,DDL0 ,DDL0 ,
TQD15A , TQD15B ,DDL0 ,DDL0 ,DDL0 ,DDL0 ,TQF16A , TQF16B , DDL0 ,DDL0 ,
```

```
DDL0 ,DDL0 ,TQD16A ,TQD16B , DDL0 ,DDL0, DDL0 ,DDL0 , TQF17A, TQF17B ,
DDL0 ,DDL0 ,DDL0 ,DDL0 ,TQD17A , TQD17B,DDL0 ,DDL0 ,DDL0 ,DDL0 ,
TQF18A , TQF18B , DDL0 ,DDL0 ,DDL0 ,DDL0 ,TQD18A ,TQD18B , DDL0 ,DDL0,
DDL0 ,DDL0 , TQF19A, TQF19B , DDL0 ,DDL0 ,DDL0 ,DDL0 ,TQD19A , TQD19B,
DDL0 ,DDL0 ,DDL0 ,DDL0 , TQF20A , TQF20B , DDL0 ,DDL0 ,DDL0 ,DDL0 ,
TQD20A ,TQD20B , DDL0 ,DDL0, DDL0 ,DDL0 , TQF21A, TQF21B, DDL0 ,DDL0 ,
DDL0 ,DDL0 ,TQD21A , TQD21B ,DDL0 ,DDL0 ,DDL0 ,DDL0 , TQF22A , TQF22B ,
DDL0 ,DDL0 ,DDL0 ,DDL0 ,TQD22A ,TQD22B, DDL0 ,DDL0, DDL0 ,DDL0 ,
TQF23A, TQF23B ,DDL0 ,DDL0 ,DDL0 ,DDL0 ,TQD23A , TQD23B ,DDL0 ,DDL0 ,
DDL0 ,DDL0 , TQF24A , TQF24B , DDL0 ,DDL0 ,DDL0 ,DDL0 ,TQD24A ,TQD24B,
DDL0 ,DDL0, DDL0 ,DDL0 ,TQF25A, TQF25B ,DDL0 ,DDL0 ,DDL0 ,DDL0 ,
TQD25A ,TQD25B , DDL0 ,DDL0, DDL0 ,DDL0 , TQF8A, TQF8B,
DDL ,DDL ,
DDL ,DDL, TQD8, DDL89, TQF9, DDLe, TQD9);

//BDS2 e+ (shorter option with dipoles and sextupoles)

DIAGNOSTICS: LINE:=(TQF ,DD ,DD ,DD ,DD ,TQD ,DD ,DD ,DD ,DD, TQF2A,
TQF2B,DD2 ,DD2 ,DD2 ,TQD2A, TQD2B, DD2 ,DD2 ,DD2 , TQF3A, TQF3B,
DD2 ,DD2 ,DD2 ,TQD3A, TQD3B, DD2,DD2 ,DD2, TQF4A, TQF4B,
DD ,DD ,DD ,DD, TQD4A, TQD4B, DD,DD,DD ,DD, TQF5A, TQF5B, DD,
DD ,DD ,DD , TQD5 , DDL ,DDL , DDL ,DDL ,TQF6A, TQF6B, DDL,
DDL ,DDL ,DDL ,TQD6A , TQD6B , DDL ,DDL ,DDL ,DDL ,TQF7A ,
TQF7B , DDL ,DDL ,DDL ,DDL ,TQD7A ,TQD7B , DDL ,DDL, DDL ,
DDL , TQF11A, TQF11B, DDLA ,DDLA ,DDLA ,DDLA ,TQD11A ,
TQD11B ,DDLA ,DDLA ,DDLA ,DDLA , TQF12A , TQF12B ,
DDLA ,DDLA ,DDLA ,DDLA ,TQD12A ,TQD12B ,DDLA ,DDLA, DDLA,
DDLA , TQF13A, TQF13B, DDLA ,DDLA ,DDLA ,DDLA ,TQD13A ,
TQD13B , DDLA ,DDLA ,DDLA ,DDLA ,TQF14A , TQF14B , DDLA ,
DDLA ,DDLA ,DDLA , TQD14A ,TQD14B ,DDLA ,DDLA, DDLA ,DDLA ,
TQF15A, TQF15B, DDL0 ,DDL0 , DDL0 ,DDL0 ,TQD15A , TQD15B ,
DDL0 ,DDL0 ,DDL0 ,DDL0 ,TQF16A , TQF16B , TSF1,  DDLB-0.5 ,
DDLB ,DDLB ,DDLB ,TQD16A ,TQD16B ,DDLB,DDLB, DDLB ,DDLB ,
TQF17A, TQF17B , DDLB ,DDLB ,DDLB ,DDLB ,TQD17A , TQD17B,
DDLB ,DDLB ,DDLB , DDLB , TQF18A , TQF18B , DDLB ,DDLB ,
DDLB ,DDLB ,TQD18A ,TQD18B , DDLB , DDLB, DDLB ,DDLB ,
TQF19A, TQF19B , DDLB ,DDLB ,DDLB ,DDLB ,TQD19A , TQD19B,
DDLB ,DDLB ,DDLB ,DDLB , TQF20A , TQF20B , TSF2, DDL0-0.5 ,
DDL0 ,DDL0 ,DDL0 , TQD20A ,TQD20B , DDL0 ,DDL0, DDL0 ,DDL0 ,
TQF21A, TQF21B, DDLA ,DDLA ,DDLA , DDLA ,TQD21A , TQD21B ,
DDLA ,DDLA ,DDLA ,DDLA , TQF22A , TQF22B , DDLA ,DDLA ,
DDLA ,DDLA ,TQD22A ,TQD22B, DDLA ,DDLA, DDLA ,DDLA ,
```

```
TQF23A, TQF23B , DDLA ,DDLA ,DDLA ,DDLA ,TQD23A , TQD23B ,
DDLA ,DDLA ,DDLA ,DDLA , TQF24A , TQF24B , DDLA ,DDLA ,DDLA,
DDLA ,TQD24A ,TQD24B, DDLA , DDLA, DDLA ,DDLA ,TQF8A, TQF8B,
DDL ,DDL ,DDL ,DDL, TQD8, DDL89, TQF9, DDLe, TQD9);

//BDS2 e- (longer option with dipoles and sextupoles)

DIAGNOSTICS: LINE:=(TQF ,DD ,DD ,DD ,DD ,TQD ,DD ,DD ,DD ,DD, TQF2A,
TQF2B, DD2 ,DD2 ,DD2 ,TQD2A, TQD2B, DD2 ,DD2 ,DD2 , TQF3A, TQF3B,
DD2 ,DD2 ,DD2 ,TQD3A, TQD3B, DD2,DD2 ,DD2, TQF4A, TQF4B, DD ,
DD ,DD ,DD, TQD4A, TQD4B, DD,DD,DD ,DD, TQF5A, TQF5B, DD ,DD ,
DD ,DD ,TQD5 , DDL ,DDL ,DDL ,DDL ,TQF6A, TQF6B, DDL ,DDL ,DDL,
DDL ,TQD6A , TQD6B ,DDL ,DDL ,DDL ,DDL ,TQF7A , TQF7B , DDL ,
DDL ,DDL ,DDL ,TQD7A ,TQD7B , DDL ,DDL, DDL ,DDL , TQF11A,
TQF11B, DDLA ,DDLA ,DDLA ,DDLA ,TQD11A , TQD11B ,DDLA ,DDLA ,DDLA,
DDLA , TQF12A , TQF12B , DDLA ,DDLA ,DDLA ,DDLA ,TQD12A ,TQD12B,
DDLA , DDLA, DDLA ,DDLA , TQF13A, TQF13B, DDLA ,DDLA ,DDLA ,DDLA,
TQD13A , TQD13B ,DDLA ,DDLA ,DDLA ,DDLA ,TQF14A , TQF14B , DDLA,
DDLA , DDLA ,DDLA ,TQD14A ,TQD14B ,DDLA ,DDLA, DDLA ,DDLA , TQF15A,
TQF15B, DDL0 ,DDL0 ,DDL0 ,DDL0 ,TQD15A , TQD15B ,DDL0 ,DDL0 ,
DDL0 ,DDL0 ,TQF16A , TQF16B , TSF1, DDLB -0.5 ,DDLB ,DDLB ,DDLB,
TQD16A ,TQD16B , DDLB ,DDLB, DDLB ,DDLB , TQF17A, TQF17B , DDLB,
DDLB ,DDLB ,DDLB ,TQD17A , TQD17B,DDLB ,DDLB ,DDLB ,DDLB ,
TQF18A , TQF18B , DDLB ,DDLB ,DDLB ,DDLB ,TQD18A ,TQD18B , DDLB,
DDLB, DDLB ,DDLB , TQF19A, TQF19B , DDLB ,DDLB ,DDLB ,DDLB,
TQD19A , TQD19B,DDLB ,DDLB ,DDLB ,DDLB , TQF20A , TQF20B,
TSF2, DDL0-0.5 ,DDL0 ,DDL0 ,DDL0 ,TQD20A ,TQD20B , DDL0 ,DDL0,
DDL0 ,DDL0 , TQF21A, TQF21B, DDLA ,DDLA ,DDLA ,DDLA ,TQD21A,
TQD21B ,DDLA ,DDLA ,DDLA ,DDLA , TQF22A , TQF22B , DDLA ,DDLA ,
DDLA ,DDLA ,TQD22A ,TQD22B, DDLA ,DDLA, DDLA ,DDLA ,TQF23A, TQF23B,
DDLA ,DDLA ,DDLA ,DDLA ,TQD23A , TQD23B ,DDLA ,DDLA ,DDLA ,DDLA,
TQF24A , TQF24B , DDLA ,DDLA ,DDLA ,DDLA ,TQD24A ,TQD24B, DDLA,
DDLA, DDLA ,DDLA ,TQF25A, TQF25B ,DDL0 ,DDL0 ,DDL0 ,DDL0,
TQD25A ,TQD25B , DDL0 ,DDL0, DDL0 ,DDL0 , TQF8A, TQF8B,
DDL ,DDL ,DDL ,DDL, TQD8, DDL89, TQF9, DDLe, TQD9);
```

APPENDIX B

PLACET and GUINEA-PIG Code Implementation for the tracking and the evaluation of the solenoid field effects

In this Appendix the detector solenoid maps used for the evaluation of the solenoid effects are reported. For the CLIC dual BDS the maps used are referred to the CLICdet and we can find four different crossing angles, 16.5 and 26 mrad for CLIC 380 GeV and 20 and 25.5 mrad for CLIC 3 TeV respectively.

These maps are then used as input in the tracking code for the evaluation of the achievable luminosity for the novel CLIC dual BDS, for the results see Section 4.1.

The SiD map is reported as well since it has been used for the evaluation of the impact of the anti-solenoid in the CLIC 3 TeV with L*= 6 m option, more detail in Section 4.1.3.

B.0.1 CLICdet Solenoid maps

In this section all the four different solenoid filed maps are reported. These are the input in the tracking code to evaluate the achievable luminosity for the dual CLIC BDS. In all the maps the solenoid field is on the beam axis so $B_r = B_x$.

B.0.1.1 Crossing Angle=16.5 mrad

```
x           y   z           Bx(Br)     By  Bz
0.000000000 0 0.000000000 4.9542e-12 0 3.9944
0.004124813 0 0.249965970 0.00003734 0 3.9899
0.008249626 0 0.499931939 0.00014962 0 3.9763
0.012374438 0 0.749897909 0.00033722 0 3.9536
0.016499251 0 0.999863878 0.00060048 0 3.9218
0.020624064 0 1.249829848 0.00093926 0 3.8808
```

```
0.024748877 0 1.499795817 0.00135240 0 3.8307
0.028873690 0 1.749761787 0.00183710 0 3.7716
0.032998503 0 1.999727756 0.00238950 0 3.7035
0.037123315 0 2.249693726 0.00300620 0 3.6268
0.041248128 0 2.499659695 0.00369110 0 3.5416
0.045372941 0 2.749625665 0.00447350 0 3.4477
0.049497754 0 2.999591634 0.00545890 0 3.3436
0.053622567 0 3.249557604 0.00697670 0 3.2246
0.057747380 0 3.499523573 0.01003700 0 3.0759
0.061872192 0 3.749489543 0.01754600 0 2.8558
0.065997005 0 3.999455512 0.03376300 0 2.4671
0.070121818 0 4.249421482 0.04460600 0 1.8632
0.074246631 0 4.499387451 0.03430700 0 1.3056
0.078371444 0 4.749353421 0.02622400 0 0.9161
0.082496257 0 4.999319390 0.02254900 0 0.61475
0.086621069 0 5.249285360 0.01962700 0 0.36543
0.090745882 0 5.499251329 0.01685600 0 0.15878
0.094870695 0 5.749217299 0.00961870 0 0.0083867
0.098995508 0 5.999183269 -0.0009377 0 -0.033668
0.103120321 0 6.249149238 -0.0050761 0 0.0019492
0.107245134 0 6.499115208 -0.0046123 0 0.050085
0.111369946 0 6.749081177 -0.0030002 0 0.08512
0.115494759 0 6.999047147 -0.0015478 0 0.10491
0.119619572 0 7.249013116 -0.0005083 0 0.11337
0.123744385 0 7.498979086 0.00016646 0 0.11456
0.127869198 0 7.748945055 0.00057463 0 0.11146
0.131994011 0 7.998911025 0.00080148 0 0.10607
0.136118823 0 8.248876994 0.00090990 0 0.099625
0.140243636 0 8.498842964 0.00094347 0 0.09288
0.144368449 0 8.748808933 0.00093157 0 0.086269
0.148493262 0 8.998774903 0.00089371 0 0.080024
0.152618075 0 9.248740872 0.00084295 0 0.07425
0.156742888 0 9.498706842 0.00078730 0 0.068978
0.160867700 0 9.748672811 0.00073129 0 0.064197
0.164992513 0 9.998638781 0.00068002 0 0.059867
```

B.0.1.2 Crossing Angle=20 mrad

```
x            y z            Bx(Br)     By   Bz
0.0000000000 0 0.0000000000 4.9542e-12 0 3.9944
0.0024999583 0 0.2499875001 0.00004526 0 3.9899
0.0049999167 0 0.4999750002 0.00018136 0 3.9763
0.0074998750 0 0.7499625003 0.00040874 0 3.9536
```

```
0.0099998333 0 0.9999500004 0.00072784 0 3.9218
0.0124997917 0 1.2499375005 0.00113850 0 3.8808
0.0149997500 0 1.4999250006 0.00163920 0 3.8307
0.0174997083 0 1.7499125007 0.00222670 0 3.7716
0.0199996667 0 1.9999000008 0.00289630 0 3.7036
0.0224996250 0 2.2498875009 0.00364380 0 3.6269
0.0249995833 0 2.4998750010 0.00447390 0 3.5417
0.0274995417 0 2.7498625011 0.00542220 0 3.4477
0.0299995000 0 2.9998500013 0.00661640 0 3.3437
0.0324994583 0 3.2498375014 0.00845520 0 3.2246
0.0349994167 0 3.4998250015 0.01216200 0 3.076
0.0374993750 0 3.7498125016 0.02125500 0 2.8561
0.0399993333 0 3.9998000017 0.04092500 0 2.4677
0.0424992917 0 4.2497875018 0.05411000 0 1.8632
0.0449992500 0 4.4997750019 0.04157700 0 1.3053
0.0474992083 0 4.7497625020 0.03178000 0 0.91597
0.0499991667 0 4.9997500021 0.02733200 0 0.61468
0.0524991250 0 5.2497375022 0.02378900 0 0.36535
0.0549990833 0 5.4997250023 0.02044300 0 0.15866
0.0574990417 0 5.7497125024 0.01167400 0 0.0079144
0.0599990000 0 5.9997000025 -0.0011570 0 -0.034034
0.0624989583 0 6.2496875026 -0.0061663 0 0.0018876
0.0649989167 0 6.4996750027 -0.0055941 0 0.050147
0.0674988750 0 6.7496625028 -0.0036362 0 0.085199
0.0699988333 0 6.9996500029 -0.0018748 0 0.10497
0.0724987917 0 7.2496375030 -0.0006148 0 0.11342
0.0749987500 0 7.4996250031 0.00020276 0 0.11459
0.0774987083 0 7.7496125032 0.00069727 0 0.11148
0.0799986667 0 7.9996000033 0.00097202 0 0.10608
0.0824986250 0 8.2495875034 0.00110330 0 0.099631
0.0849985833 0 8.4995750035 0.00114380 0 0.092882
0.0874985417 0 8.7495625036 0.00112930 0 0.086269
0.0899985000 0 8.9995500037 0.00108340 0 0.080022
0.0924984583 0 9.2495375039 0.00102180 0 0.074248
0.0949984167 0 9.4995250040 0.00095434 0 0.068975
0.0974983750 0 9.7495125041 0.00088639 0 0.064194
0.0999983333 0 9.9995000042 0.00082433 0 0.059864
```

B.0.1.3 Crossing Angle=25.5 mrad

```
x            y z            Bx(Br)     By   Bz
0            0 0            4.9542e-12 0 3.9944
0.0063743091 0 0.2499187232 0.00005771 0 3.9899
```

```
0.0127486183 0 0.4998374463 0.00023122 0 3.9763
0.0191229274 0 0.7497561695 0.00052112 0 3.9536
0.0254972365 0 0.9996748926 0.00092796 0 3.9218
0.0318715457 0 1.2495936158 0.00145150 0 3.8808
0.0382458548 0 1.4995123389 0.00208990 0 3.8307
0.0446201639 0 1.7494310621 0.00283900 0 3.7716
0.0509944731 0 1.9993497852 0.00369260 0 3.7036
0.0573687822 0 2.2492685084 0.00464570 0 3.6269
0.0637430913 0 2.4991872315 0.00570400 0 3.5417
0.0701174005 0 2.7491059547 0.00691280 0 3.4478
0.0764917096 0 2.9990246779 0.00843470 0 3.3438
0.0828660187 0 3.2489434010 0.01077700 0 3.2248
0.0892403278 0 3.4988621242 0.01549500 0 3.0763
0.0956146370 0 3.7487808473 0.02706900 0 2.8569
0.1019889461 0 3.9986995705 0.05218000 0 2.469
0.1083632552 0 4.2486182936 0.06909200 0 1.8632
0.1147375644 0 4.4985370168 0.05299100 0 1.3046
0.1211118735 0 4.7484557399 0.04050300 0 0.91571
0.1274861826 0 4.9983744631 0.03484800 0 0.61454
0.1338604918 0 5.2482931862 0.03032800 0 0.36521
0.1402348009 0 5.4982119094 0.02609200 0 0.15842
0.1466091100 0 5.7481306325 0.01492200 0 0.0069855
0.1529834192 0 5.9980493557 -0.0015272 0 -0.034755
0.1593577283 0 6.2479680789 -0.0078954 0 0.0017686
0.1657320374 0 6.4978868020 -0.0071411 0 0.05027
0.1721063466 0 6.7478055252 -0.0046351 0 0.085355
0.1784806557 0 6.9977242483 -0.0023871 0 0.1051
0.1848549648 0 7.2476429715 -0.0007807 0 0.11351
0.1912292740 0 7.4975616946 0.00026103 0 0.11465
0.1976035831 0 7.7474804178 0.00089088 0 0.11152
0.2039778922 0 7.9973991409 0.00124070 0 0.1061
0.2103522014 0 8.2473178641 0.00140760 0 0.099644
0.2167265105 0 8.4972365872 0.00145900 0 0.092888
0.2231008196 0 8.7471553104 0.00144050 0 0.086269
0.2294751287 0 8.9970740336 0.00138200 0 0.080019
0.2358494379 0 9.2469927567 0.00130290 0 0.074243
0.2422237470 0 9.4969114799 0.00121700 0 0.06897
0.2485980561 0 9.7468302030 0.00113010 0 0.064189
0.2549723653 0 9.9967489262 0.00105120 0 0.059858
```

B.0.1.4 Crossing Angle=26 mrad

```
x           y z           Bx(Br)      By Bz
```

```
0           0 0           4.9542e-12 0 3.9944
0.006499268 0 0.249915505 0.00005884 0 3.9899
0.012998535 0 0.499831010 0.00023575 0 3.9763
0.019497803 0 0.749746514 0.00053133 0 3.9536
0.025997071 0 0.999662019 0.00094615 0 3.9218
0.032496338 0 1.249577524 0.00147990 0 3.8808
0.038995606 0 1.499493029 0.00213090 0 3.8307
0.045494874 0 1.749408533 0.00289460 0 3.7716
0.051994142 0 1.999324038 0.00376500 0 3.7036
0.058493409 0 2.249239543 0.00473680 0 3.6269
0.064992677 0 2.499155048 0.00581580 0 3.5417
0.071491945 0 2.749070552 0.00704830 0 3.4478
0.077991212 0 2.998986057 0.00860000 0 3.3438
0.084490480 0 3.248901562 0.01098800 0 3.2248
0.090989748 0 3.498817067 0.01579800 0 3.0763
0.097489015 0 3.748732571 0.02759700 0 2.8569
0.103988283 0 3.998648076 0.05320300 0 2.4692
0.110487551 0 4.248563581 0.07045700 0 1.8632
0.116986818 0 4.498479086 0.05402800 0 1.3045
0.123486086 0 4.748394590 0.04129500 0 0.91568
0.129985354 0 4.998310095 0.03553200 0 0.61452
0.136484622 0 5.248225600 0.03092200 0 0.36519
0.142983889 0 5.498141105 0.02660700 0 0.15839
0.149483157 0 5.748056609 0.01521800 0 0.0068918
0.155982425 0 5.997972114 -0.0015626 0 -0.034829
0.162481692 0 6.247887619 -0.0080538 0 0.0017564
0.168980960 0 6.497803124 -0.0072820 0 0.050282
0.175480228 0 6.747718629 -0.0047259 0 0.085371
0.181979495 0 6.997634133 -0.0024336 0 0.10511
0.188478763 0 7.247549638 -0.0007958 0 0.11352
0.194978031 0 7.497465143 0.00026642 0 0.11466
0.201477298 0 7.747380648 0.00090854 0 0.11152
0.207976566 0 7.997296152 0.00126510 0 0.10611
0.214475834 0 8.247211657 0.00143540 0 0.099644
0.220975102 0 8.497127162 0.00148770 0 0.092887
0.227474369 0 8.747042667 0.00146890 0 0.086269
0.233973637 0 8.996958171 0.00140900 0 0.080019
0.240472905 0 9.246873676 0.00132840 0 0.074243
0.246972172 0 9.496789181 0.00124080 0 0.068969
0.253471440 0 9.746704686 0.00115220 0 0.064188
0.259970708 0 9.996620190 0.00107180 0 0.059858
```

B.0.2 SiD Solenoid Map

x	y	z	Bx(Br)	By	Bz
0.00000000e+00	0.0	0.00000000e+00	0.00000000e+00	0.0	3.97749299e+00
2.39999999e-03	0.0	2.39999999e-01	3.19999999e-05	0.0	3.97430100e+00
4.79999999e-03	0.0	4.79999999e-01	1.27999999e-04	0.0	3.96471600e+00
7.19999999e-03	0.0	7.19999999e-01	2.88000000e-04	0.0	3.94871499e+00
9.59999999e-03	0.0	9.59999999e-01	5.14000000e-04	0.0	3.92626799e+00
1.20000000e-02	0.0	1.19999999e+00	8.05000000e-04	0.0	3.89733399e+00
1.43999999e-02	0.0	1.43999999e+00	1.16299999e-03	0.0	3.86186400e+00
1.67999999e-02	0.0	1.67999999e+00	1.59000000e-03	0.0	3.81978099e+00
1.91999999e-02	0.0	1.91999999e+00	2.09200000e-03	0.0	3.77093800e+00
2.16000000e-02	0.0	2.16000000e+00	2.68499999e-03	0.0	3.71501100e+00
2.40000000e-02	0.0	2.39999999e+00	3.40699999e-03	0.0	3.65125199e+00
2.63999999e-02	0.0	2.64000000e+00	4.35199999e-03	0.0	3.57794599e+00
2.87999999e-02	0.0	2.87999999e+00	5.75699999e-03	0.0	3.49114600e+00
3.11999999e-02	0.0	3.12000000e+00	8.22400000e-03	0.0	3.38165499e+00
3.35999999e-02	0.0	3.35999999e+00	1.32770000e-02	0.0	3.22768699e+00
3.59999999e-02	0.0	3.60000000e+00	2.40579999e-02	0.0	2.98004500e+00
3.83999999e-02	0.0	3.83999999e+00	4.12640000e-02	0.0	2.56227399e+00
4.08000000e-02	0.0	4.08000000e+00	4.90109999e-02	0.0	1.99381399e+00
4.32000000e-02	0.0	4.32000000e+00	3.94120000e-02	0.0	1.47868899e+00
4.56000000e-02	0.0	4.55999999e+00	2.87740000e-02	0.0	1.11344400e+00
4.80000000e-02	0.0	4.79999999e+00	2.22940000e-02	0.0	8.54173999e-01
5.04000000e-02	0.0	5.04000000e+00	1.78210000e-02	0.0	6.59155999e-01
5.27999999e-02	0.0	5.28000000e+00	1.56189999e-02	0.0	5.07341999e-01
5.51999999e-02	0.0	5.51999999e+00	1.86319999e-02	0.0	3.57042000e-01
5.75999999e-02	0.0	5.75999999e+00	1.66369999e-02	0.0	1.99755999e-01
5.99999999e-02	0.0	6.00000000e+00	9.52800000e-03	0.0	9.23139999e-02
6.23999999e-02	0.0	6.24000000e+00	4.02200000e-03	0.0	4.09079999e-02
6.47999999e-02	0.0	6.48000000e+00	9.15000000e-04	0.0	2.36829999e-02
6.71999999e-02	0.0	6.71999999e+00	-1.14000000e-04	0.0	2.20540000e-02
6.95999999e-02	0.0	6.95999999e+00	1.56999999e-04	0.0	2.22830000e-02
7.19999999e-02	0.0	7.20000000e+00	5.73000000e-04	0.0	1.97449999e-02
7.43999999e-02	0.0	7.44000000e+00	8.55999999e-04	0.0	1.49840000e-02
7.67999999e-02	0.0	7.67999999e+00	1.03000000e-03	0.0	8.94499999e-03
7.92000000e-02	0.0	7.91999999e+00	1.12399999e-03	0.0	2.27699999e-03
8.16000000e-02	0.0	8.16000000e+00	-2.99999999e-04	0.0	0.00000000e+00

B.0.3 Tracking Code

The tracking code used is PLACET and then GUINEA-PIG has been used for the evaluation of the luminosity performance. For the dual CLIC BDS since you have four different

beamlines BDS1 e+ and e- and BDS2 e+ and e- you need to track it more than once with different layouts and different maps.

B.0.3.1 CLIC 380 GeV

```
set e_initial 190.0
set e0 $e_initial
set script_dir .

array set args {
    step 0.001
    n_slice 30
    n 2000
}

array set args $argv

# Step length in the IR tracking routine
set step $args(step)
# Number of slices
set n_slice $args(n_slice)
# Number of particles per slice
set n $args(n)

set synrad 0
set quad_synrad 1
set mult_synrad 1
set sbend_synrad 1
set scale 1.0

source $script_dir/clic_basic_single.tcl

proc save_beam {name} {

    BeamDump -file $name
}

#source bds_380_bend_0.5_coll.tcl
source bds_380_bend_0_coll.tcl
#source bds.coll.tcl
set name0 particles.out.coll
TclCall -script {save_beam $name0}
```

```
BeamlineSet -name test.coll

array set match {
    alpha_x 0
    alpha_y 0
    beta_x  33.07266007
    beta_y  8.962361942
}
##############################
# CHECK EMITTANCE BEFORE RUN #
##############################
#it was 6.8 and 4e9

set match(emitt_x) 9.5
set match(emitt_y) 0.300
set match(charge) 5.2e9
set charge $match(charge)
set match(sigma_z) 70.0
set match(phase) 0.0
set match(e_spread) -1.0

puts " generating the beam "

set n_total [expr $n_slice*$n]
source $script_dir/clic_beam.tcl

#make_beam_halo $e0 $match(e_spread) $n_total
make_beam_particles $e0 $match(e_spread) $n_total

make_beam_many beam0 $n_slice $n
BeamRead -file particles.in -beam beam0

FirstOrder 1
puts " start tracking in collimation section "
BeamlineUse -name test.coll
TestNoCorrection -beam beam0 -emitt_file emitt.dat -survey Zero
puts " end tracking in collimation section "
puts " puts bds ffs "

BeamlineNew
#source bds_380_bend_0.5.tcl
source bds_380_bend_0.tcl
```

```
set name1 particles.ffs.out
TclCall -script {save_beam $name1}
BeamlineSet -name test.ffs
# new beam
make_beam_many beam1 $n_slice $n
#make_beam_many beam1 1 1
BeamRead -file $name0 -beam beam1
BeamlineUse -name test.ffs
TestNoCorrection -beam beam1 -emitt_file emitt.dat -survey Zero

#set solmap map380GeVca26_v2.txt
set solmap map380GeVca16.5_v2.txt

if { $n_total == 1} { set writefirst 1 } else { set writefirst 0 }

# Track beam through without solenoids..
BeamlineNew
#source bds.ffs.last.tcl
#source bds_380_bend_0.5_last.tcl
source bds_380_bend_0_last.tcl
set name2 particles.ffs.last.out
TclCall -script {save_beam $name2}
BeamlineSet -name test.ffs.last

puts " TestIntRegion forwards.. "
make_beam_many beam2 $n_slice $n
BeamRead -file $name1 -beam beam2
BeamlineUse -name test.ffs.last
set t_0 [clock seconds]
# TestNoCorrection -beam beam2 -emitt_file emitt.dat -survey Zero
TestIntRegion -beam beam2 -emitt_file emitt.dat -survey Zero
-angle 0.01 -step $step -synrad 0 -writefirst $writefirst
if { $writefirst } { exec mv singtrk.dat singtrk.1.dat }
set name_ideal particle.dist.no_solenoid.out
exec mv $name2 $name_ideal

puts " TestIntRegion forwards.. "
make_beam_many beam5 $n_slice $n
BeamRead -file $name1 -beam beam5
set t_1 [clock seconds]
TestIntRegion -beam beam5 -emitt_file emitt.dat -survey Zero
-angle 0.01 -step $step -synrad 1 -writefirst $writefirst
```

```
if { $writefirst } { exec mv singtrk.dat singtrk.4.dat }
set name_synrad particle.dist.only_synrad.out
exec mv $name2 $name_synrad


puts " TestIntRegion forwards single track... "
make_beam_many beam6 1 1
exec echo "1496. 0. 0. 0. 0. 0." > beam.in
BeamRead -file beam.in -beam beam6
TestIntRegion -beam beam6 -emitt_file emitt.dat -survey Zero
-angle 0.01 -step $step -synrad 0 -filename $solmap -writefirst $writefirst
if { $writefirst } { exec mv singtrk.dat singtrk.5.dat }
set name_strk particle.dist.strk_ref.out
exec mv $name2 $name_strk

# prepare backward...
set avang 0
set strk [open particle.dist.strk_ref.out r]
gets $strk l
set avang [lindex $l 5]
puts "Vertical angle at IP: $avang"
close $strk
set name_ideal1 particle.dist.no_solenoid_syn.out
exec awk -v ang=$avang {{print $1,$2,$3,$4,$5,$6+ang}}
$name_ideal > $name_ideal1

# track positron beam backwards...
make_beam_many beam3 $n_slice $n
BeamRead -file $name_ideal1 -beam beam3

puts " TestIntRegion backwards.. "
set t_2 [clock seconds]
TestIntRegion -beam beam3 -emitt_file emitt.dat -survey Zero
-angle 0.01 -step $step -synrad 0 -filename
$solmap -writefirst $writefirst -backward 1
if { $writefirst } { exec mv singtrk.dat singtrk.2.dat }
set name_bef_ffs particle.dist.beforeffs.out
exec mv $name2 $name_bef_ffs


make_beam_many beam4 $n_slice $n
BeamRead -file $name_bef_ffs -beam beam4
```

```
puts " TestIntRegion forwards.. "
set t_3 [clock seconds]
TestIntRegion -beam beam4 -emitt_file emitt.dat -survey Zero
-angle 0.01 -step $step -synrad 1 -filename $solmap -writefirst $writefirst
if { $writefirst } { exec mv singtrk.dat singtrk.3.dat }
set name_final particle.dist.solenoid_and_synrad.out
set avang [expr -$avang]
exec awk -v ang=$avang {{print $1,$2,$3,$4,$5,$6+ang}}
$name2 > $name_final

puts " Final Reference Energy = $e0 "
set t_4 [clock seconds]

puts "\n--------------   TIME   --------------------"
puts "       First forward sim took [expr ($t_1-$t_0)/60.] minutes"
puts "      Second forward sim took [expr ($t_2-$t_1)/60.] minutes"
puts "            Backward sim took [expr ($t_3-$t_2)/60.] minutes"
puts "       Third forward sim took [expr ($t_4-$t_3)/60.] minutes"
puts "Total sim time for irtracking [expr ($t_4-$t_0)/60.] minutes"
puts "-----------------------------------------\n"

if { $n > 499 && $n_slice > 9 } { source guinea2.tcl }
```

GUINEA-PIG Code

```
set script_dir .

#array set match {
#    alpha_x 0.59971622
#    alpha_y -1.93937335
#    beta_x  18.382571
#    beta_y  64.450775
#}

array set match {
    alpha_x 0.00
    alpha_y 0.00
    beta_x 33.07266007
   beta_y 8.962361942

}
```

```
#emittances unit is e-7
set match(emitt_x)  9.5
set match(emitt_y)  0.3
set match(charge) 5.2e9
set charge $match(charge)
set match(sigma_z) 70.0
set match(phase) 0.0
set match(e_spread) -1.0
#set match(e_spread) 0.0

######################################################################
# GUINEA-PIG
######################################################################

array set gp_param "
    energy 190.0
    particles [expr $match(charge)*1e-10]
    sigmaz $match(sigma_z)
    cut_x 200.0
    cut_y 25.0
    n_x 64
    n_y 320
    do_coherent 1
    n_t 1
    charge_sign -1.0"


source $script_dir/clic_guinea.tcl
proc run_guinea {off angle} {
    global gp_param
    set res [exec grid]
    set yoff [expr -0.5*([lindex $res 2]+[lindex $res 3])]
    set xoff [expr -0.5*([lindex $res 0]+[lindex $res 1])]
    set tx $gp_param(cut_x)
    set ty $gp_param(cut_y)
    if {[lindex $res 1]-[lindex $res 0]>2.0*$tx} {
        set gp_param(cut_x) [expr 0.5*([lindex $res 1]-[lindex $res 0])]
       }
    if {[lindex $res 3]-[lindex $res 2]>2.0*$ty} {
        set gp_param(cut_y) [expr 0.5*([lindex $res 3]-[lindex $res 2])]
       }
```

```
    puts "yoff $yoff"
    puts "xoff $xoff"
    write_guinea_correct $xoff $yoff
    #exec guinea++ default default result.out
    #exec /afs/cern.ch/eng/sl/clic-code/lx64slc5/guinea-pig/bin/
    guinea-old default_clic default result.out
    exec guinea-old default default result.out
    set gp_param(cut_x) $tx
    set gp_param(cut_y) $ty
    return [get_results result.out]
}
#####################################################################


if { [file exists "electron.ini"] } {exec rm electron.ini positron.ini}
exec ln -s $name_ideal electron.ini
exec ln -s $name_ideal positron.ini
set res [run_guinea 0.0 0.0]
puts "With ideal: $res"

exec rm electron.ini positron.ini
exec ln -s $name_synrad electron.ini
exec ln -s $name_synrad positron.ini
set res [run_guinea 0.0 0.0]
puts "With synrad: $res"

exec rm electron.ini positron.ini
exec ln -s $name_final electron.ini
exec ln -s $name_final positron.ini
set res [run_guinea 0.0 0.0]
puts "With solenoid&synrad: $res"
```

B.0.3.2 CLIC 3 TeV

```
set e_initial 1500.0
set e0 $e_initial
set script_dir .

array set args {
    step 0.001
    n_slice 30
```

```
    n 2000
}

array set args $argv

# Step length in the IR tracking routine
set step $args(step)
# Number of slices
set n_slice $args(n_slice)
# Number of particles per slice
set n $args(n)

set synrad 0
set quad_synrad 0
set mult_synrad 0
set sbend_synrad 0
set scale 1.0

source $script_dir/clic_basic_single.tcl

proc save_beam {name} {

    BeamDump -file $name
}

source clic3TeV_design_coll.tcl
#source bds.coll.3tev.bend0.tcl
#source bds_0.1_coll.tcl
#source bds.coll.tcl
set name0 particles.out.coll
TclCall -script {save_beam $name0}
BeamlineSet -name test.coll

array set match {
    alpha_x 0
    alpha_y 0
    beta_x  66.14532014
    beta_y  17.92472388
}
##############################
# CHECK EMITTANCE BEFORE RUN #
##############################
```

```
#it was 6.8 and 4e9

set match(emitt_x) 6.600
set match(emitt_y) 0.200
set match(charge) 3.72e9
set charge $match(charge)
set match(sigma_z) 44.0
set match(phase) 0.0
set match(e_spread) -1.0

puts " generating the beam "

set n_total [expr $n_slice*$n]
source $script_dir/clic_beam.tcl

#make_beam_halo $e0 $match(e_spread) $n_total
make_beam_particles $e0 $match(e_spread) $n_total

make_beam_many beam0 $n_slice $n
BeamRead -file particles.in -beam beam0

FirstOrder 1
puts " start tracking in collimation section "
BeamlineUse -name test.coll
TestNoCorrection -beam beam0 -emitt_file emitt.dat -survey Zero
puts " end tracking in collimation section "
puts " puts bds ffs "

BeamlineNew
#source bds.ffs.tcl
#source bds_0.1_new_optimized.tcl
source clic3TeV_design.tcl
#source bds_3tev_bend_0.tcl
set name1 particles.ffs.out
TclCall -script {save_beam $name1}
BeamlineSet -name test.ffs
# new beam
make_beam_many beam1 $n_slice $n
#make_beam_many beam1 1 1
BeamRead -file $name0 -beam beam1
BeamlineUse -name test.ffs
TestNoCorrection -beam beam1 -emitt_file emitt.dat -survey Zero
```

```
#map for the SiD detector
#set solmap SiD_antisolenoid.txt

#map to get the c.a. of 25.5 mrad
#set solmap map3TeVca25.5.txt

# map to get the c.a. of 20 mrad
#set solmap map3TeVca10.txt

if { $n_total == 1} { set writefirst 1 } else { set writefirst 0 }

# Track beam through without solenoids..
BeamlineNew
#source bds.ffs.last.tcl
#source bds.ffs.3TeV.last.0bend.tcl
source clic3TeV_design_last.tcl
#source bds_0.1_last.tcl
set name2 particles.ffs.last.out
TclCall -script {save_beam $name2}
BeamlineSet -name test.ffs.last

puts " TestIntRegion forwards.. "
make_beam_many beam2 $n_slice $n
BeamRead -file $name1 -beam beam2
BeamlineUse -name test.ffs.last
set t_0 [clock seconds]
# TestNoCorrection -beam beam2 -emitt_file emitt.dat -survey Zero
TestIntRegion -beam beam2 -emitt_file emitt.dat -survey Zero
-angle 0.01 -step $step -synrad 0 -writefirst $writefirst
if { $writefirst } { exec mv singtrk.dat singtrk.1.dat }
set name_ideal particle.dist.no_solenoid.out
exec mv $name2 $name_ideal

puts " TestIntRegion forwards.. "
make_beam_many beam5 $n_slice $n
BeamRead -file $name1 -beam beam5
set t_1 [clock seconds]
TestIntRegion -beam beam5 -emitt_file emitt.dat -survey Zero
-angle 0.01 -step $step -synrad 1 -writefirst $writefirst
if { $writefirst } { exec mv singtrk.dat singtrk.4.dat }
set name_synrad particle.dist.only_synrad.out
```

```
exec mv $name2 $name_synrad


puts " TestIntRegion forwards single track... "
make_beam_many beam6 1 1
exec echo "1496. 0. 0. 0. 0. 0." > beam.in
BeamRead -file beam.in -beam beam6
TestIntRegion -beam beam6 -emitt_file emitt.dat -survey Zero
-angle 0.01 -step $step -synrad 0 -filename
$solmap -writefirst $writefirst
if { $writefirst } { exec mv singtrk.dat singtrk.5.dat }
set name_strk particle.dist.strk_ref.out
exec mv $name2 $name_strk

# prepare backward...
set avang 0
set strk [open particle.dist.strk_ref.out r]
gets $strk l
set avang [lindex $l 5]
puts "Vertical angle at IP: $avang"
close $strk
set name_ideal1 particle.dist.no_solenoid_syn.out
exec awk -v ang=$avang {{print $1,$2,$3,$4,$5,$6+ang}}
$name_ideal > $name_ideal1

# track positron beam backwards...
make_beam_many beam3 $n_slice $n
BeamRead -file $name_ideal1 -beam beam3

puts " TestIntRegion backwards.. "
set t_2 [clock seconds]
TestIntRegion -beam beam3 -emitt_file emitt.dat -survey Zero
-angle 0.01 -step $step -synrad 0 -filename
$solmap -writefirst $writefirst -backward 1
if { $writefirst } { exec mv singtrk.dat singtrk.2.dat }
set name_bef_ffs particle.dist.beforeffs.out
exec mv $name2 $name_bef_ffs


make_beam_many beam4 $n_slice $n
BeamRead -file $name_bef_ffs -beam beam4
puts " TestIntRegion forwards.. "
```

```
set t_3 [clock seconds]
TestIntRegion -beam beam4 -emitt_file emitt.dat -survey Zero
-angle 0.01 -step $step -synrad 1 -filename
$solmap -writefirst $writefirst
if { $writefirst } { exec mv singtrk.dat singtrk.3.dat }
set name_final particle.dist.solenoid_and_synrad.out
set avang [expr -$avang]
exec awk -v ang=$avang {{print $1,$2,$3,$4,$5,$6+ang}}
$name2 > $name_final

puts " Final Reference Energy = $e0 "
set t_4 [clock seconds]

puts "\n--------------   TIME   --------------------"
puts "       First forward sim took [expr ($t_1-$t_0)/60.] minutes"
puts "      Second forward sim took [expr ($t_2-$t_1)/60.] minutes"
puts "            Backward sim took [expr ($t_3-$t_2)/60.] minutes"
puts "       Third forward sim took [expr ($t_4-$t_3)/60.] minutes"
puts "Total sim time for irtracking [expr ($t_4-$t_0)/60.] minutes"
puts "-----------------------------------------\n"

if { $n > 499 && $n_slice > 9 } { source guinea.tcl }
```

GUINEA-PIG Code

```
set script_dir .

# When using energy spread distribution from Linac
#array set match {
#    alpha_x 0.59971622
#    alpha_y -1.93937335
#    beta_x  18.382571
#    beta_y  64.450775
#}

# 1% full width energy spread distrib
array set match {
    alpha_x 0.0
    alpha_y 0.0
    beta_x 66.14532014
    beta_y 17.92472388
```

```
}

#emittances unit is e-7
set match(emitt_x)  6.6
set match(emitt_y)  0.2
set match(charge) 3.72e9
set charge $match(charge)
set match(sigma_z) 44.0
set match(phase) 0.0
set match(e_spread) -1.0
#set match(e_spread) 0.0

######################################################################
# GUINEA-PIG
######################################################################

array set gp_param "
    energy 1500.0
    particles [expr $match(charge)*1e-10]
    sigmaz $match(sigma_z)
    cut_x 200.0
    cut_y 25.0
    n_x 64
    n_y 256
    do_coherent 1
    n_t 1
    charge_sign -1.0"



source $script_dir/clic_guinea.tcl
proc run_guinea {off angle} {
    global gp_param
    set res [exec grid]
    set yoff [expr -0.5*([lindex $res 2]+[lindex $res 3])]
    set xoff [expr -0.5*([lindex $res 0]+[lindex $res 1])]
    set tx $gp_param(cut_x)
    set ty $gp_param(cut_y)
    if {[lindex $res 1]-[lindex $res 0]>2.0*$tx} {
        set gp_param(cut_x) [expr 0.5*([lindex $res 1]-[lindex $res 0])]
       }
    if {[lindex $res 3]-[lindex $res 2]>2.0*$ty} {
```

```
        set gp_param(cut_y) [expr 0.5*([lindex $res 3]-[lindex $res 2])]
       }
    puts "yoff $yoff"
    puts "xoff $xoff"
    write_guinea_correct $xoff $yoff
    #exec guinea++ default default result.out
    #exec /afs/cern.ch/eng/sl/clic-code/lx64slc5/guinea-pig/bin/
    guinea-old default_clic default result.out
    exec guinea-old default default result.out
    set gp_param(cut_x) $tx
    set gp_param(cut_y) $ty
    return [get_results result.out]
}
#####################################################################


if { [file exists "electron.ini"] } {exec rm electron.ini positron.ini}
exec ln -s $name_ideal electron.ini
exec ln -s $name_ideal positron.ini
set res [run_guinea 0.0 0.0]
puts "With ideal: $res"

exec rm electron.ini positron.ini
exec ln -s $name_synrad electron.ini
exec ln -s $name_synrad positron.ini
set res [run_guinea 0.0 0.0]
puts "With synrad: $res"

exec rm electron.ini positron.ini
exec ln -s $name_final electron.ini
exec ln -s $name_final positron.ini
set res [run_guinea 0.0 0.0]
puts "With solenoid&synrad: $res"
```

APPENDIX C

Articles and publications

C.1 List of publications

- V. Cilento, R. Tomás, B. Cure, A. Faus-Golfe, B. Dalena, Y. Levinsen
  A Dual Beam Delivery System serving two Interaction Regions for the Compact Linear Collider, Phys. Rev. Accel. Beams **24**, 071001 - Published 29 July 2021 [99].

- V. Cilento, R. Tomás, A. Faus-Golfe
  A CLIC Dual Beam Delivery System for two Interaction Regions, Proceedings of IPAC2021, Campinas, Brazil TUPAB013 (2021) - Published 31 August 2021 [100].

- V. Cilento, A. Pastushenko, R. Yang, R. Tomás, A. Faus-Golfe, N. Terunuma, T. Okugi, and K. Kubo
  ATF2 Ultra-low β_y^* study report for March 2019 run, CERN-ACC-NOTE-2020-0006 - Published 17 January 2020 [101].

- R. Yang, A. Pastushenko, V. Cilento, K. Kubo, T. Naito, T. Okugi, N. Terunuma, and R. Tomás
  Momentum bandwidth of the KEK Accelerator Test Facility 2, Phys. Rev. Accel. Beams **24**, 051001 - Published 21 May 2021 [96].

- R. Yang, A. Pastushenko, A. Aryshev, M. Bergamaschi, V. Cilento, A. Faus-Golfe, M. Fukuda, P. Korysko, K. Kubo, S. Kuroda, T. Naito, T. Okugi, F. Plassard, N. Terunuma, and R. Tomás

Tuning the ultralow β_y optics at the KEK Accelerator Test Facility 2, Phys. Rev. Accel. Beams **23**, 071003 - Published 23 July 2020 [48].

- *ATF Report 2020*, CERN-ACC-2020-0029 - Published 13 October 2020 [102].

- *CLIC Project Implementation Plan*, CERN-2018-010-M - Published 20 December 2018 [16].

List of Figures

List of Tables

Bibliography

[1] O. Brüning et al. *LHC Design Report CERN-2004-003-V-1*. 2004.

[2] Fedor Bezrukov, Mikhail Yu Kalmykov, Bernd A. Kniehl, and Mikhail Shaposhnikov. "Higgs boson mass and new physics". In: *Journal of High Energy Physics* 2012.**10** (2012), pp. 1–35.

[3] Serguei Chatrchyan, Vardan Khachatryan, Albert M Sirunyan, Armen Tumasyan, Wolfgang Adam, Ernest Aguilo, Thomas Bergauer, M. Dragicevic, J. Erö, C. Fabjan, et al. "Observation of a new boson at a mass of 125 GeV with the CMS experiment at the LHC". In: *Physics Letters B* **716**.1 (2012), pp. 30–61.

[4] The European Strategy Group. *Deliberation document on the 2020 Update of the European Strategy for Particle Physics*. Tech. rep. Geneva, 2020. DOI: 10.17181/ESU2020Deliberation. URL: https://cds.cern.ch/record/2720131.

[5] *High-Luminosity Large Hadron Collider (HL-LHC): Technical Design Report V. 0.1*. CERN Yellow Reports: Monographs. Geneva: CERN, 2017. DOI: 10.23731/CYRM-2017-004. URL: https://cds.cern.ch/record/2284929.

[6] P.I.P. Kalmus. "Particle physics at the turn of the century". In: *Contemporary Physics* **41**.**3** (2000), pp. 129–142.

[7] Katsunobu Oide. "Synchrotron-Radiation Limit on the Focusing of Electron Beams". In: *Phys. Rev. Lett.* **61** (15 Oct. 1988), pp. 1713–1715. DOI: 10.1103/PhysRevLett.61.1713. URL: https://link.aps.org/doi/10.1103/PhysRevLett.61.1713.

[8] Matthew Sands. *Emittance growth from radiation fluctuations*. Tech. rep. Stanford Linear Accelerator Center, Menlo Park, CA (USA), 1985.

[9] D. Schulte. "Technical Overview and Challenges of Proposed Higgs Factories". In: *presentation at the CERN Council Open Symposium on the update of the European Strategy for Particle Physics* (13-16 May 2019, Granada, Spain).

[10] Michael Benedikt and Frank Zimmermann. "Towards future circular colliders". In: *Journal of the Korean Physical Society* **69**.**6** (2016), pp. 893–902.

[11] A. Abada, M. Abbrescia, Shehu S. AbdusSalam, I. Abdyukhanov, J. Abelleira Fernandez, A. Abramov, M. Aburaia, A.O. Acar, P.R. Adzic, P. Agrawal, et al. "FCC-ee: the lepton collider". In: *The European Physical Journal Special Topics* **228.2** (2019), pp. 261–623.

[12] FCC collaboration et al. "FCC-hh: The hadron collider: Future circular collider conceptual design report volume 3". In: *European Physical Journal: Special Topics* **228.4** (2019), pp. 755–1107.

[13] The CEPC Study Group. *CEPC Conceptual Design Report: Volume 1 - Accelerator*. 2018. arXiv: 1809.00285 [physics.acc-ph].

[14] *The International Linear Collider Technical Design Report*. Tech. rep. June 2013.

[15] M. Aicheler, P. Burrows, M. Draper, T. Garvey, P. Lebrun, K. Peach, N. Phinney, H. Schmickler, D. Schulte, and N. Toge. *A Multi-TeV Linear Collider Based on CLIC Technology: CLIC Conceptual Design Report*. CERN Yellow Reports: Monographs. Geneva: CERN, 2012. DOI: 10.5170/CERN-2012-007. URL: https://cds.cern.ch/record/1500095.

[16] M. Aicheler, P.N. Burrows, N. Catalan Lasheras, R. Corsini, M. Draper, J. Osborne, D. Schulte, S. Stapnes, and M.J. Stuart. *The Compact Linear Collider (CLIC) – Project Implementation Plan*. Ed. by M. Aicheler. CERN Yellow Reports: Monographs. 247 p. Geneva: CERN, Mar. 2019. DOI: 10.23731/CYRM-2018-004. URL: https://cds.cern.ch/record/2652600.

[17] Nuria Fuster Martinez. "Beam halo collimation and induced wakefield studies for future linear colliders: the ATF2 case". PhD thesis. Universitat de València, 2017.

[18] CERN Accelerator School. Intermediate Accelerator Physics. *CERN Accelerator School, Intermediate Accelerator Physics: Desy, Zeuthen, Germany, 15-26 September 2003: Proceedings*. CERN, 2006.

[19] Daniel Schulte. "Beam-beam effects in linear colliders". In: *CERN Yellow Reports: School Proceedings* **3** (2017), pp. 431–431.

[20] Fabien Plassard, Andrea Latina, Eduardo Marin, Rogelio Tomás, and Philip Bambade. "Quadrupole free detector optics design for the Compact Linear Collider final focus system at 3 TeV". In: *Phys. Rev. Accel. Beams* **21** (1 Jan. 2018), p. 011002. DOI: 10.1103/PhysRevAccelBeams.21.011002.

[21] Alexander Wu Chao, Karl Hubert Mess, et al. *Handbook of accelerator physics and engineering*. World scientific, 2013.

[22] Hector Garcia Morales. "Comparative study of Final Focus Systems for CLIC and other luminosity ehancement studies for future linear colliders". Presented 16 Jan 2015. 2014. URL: https://cds.cern.ch/record/1982827.

[23] E. Marin, M. Modena, T. Tauchi, N. Terunuma, R. Tomás, G.R. White, et al. *Specifications of the octupole magnets required for the ATF2 ultra-low ß* lattice*. Tech. rep. SLAC National Accelerator Laboratory (SLAC), 2014.

[24] V. Balakin et al. “Focusing of Submicron Beams for TeV-Scale e+ e- Linear Colliders”. In: *Physical review letters* **74** (Apr. 1995), pp. 2479–2482. DOI: 10.1103/PhysRevLett.74.2479.

[25] T. O. Raubenheimer and F. Zimmermann. “Final-focus systems in linear colliders”. In: *Rev. Mod. Phys.* **72** (1 Jan. 2000), pp. 95–107. DOI: 10.1103/RevModPhys.72.95. URL: https://link.aps.org/doi/10.1103/RevModPhys.72.95.

[26] H. Garcia, A. Latina, and R. Tomas. “Traditional Final Focus System for CLIC”. In: *Conf. Proc.* C1205201 (May 2012), TUPPR022. 3 p. URL: https://cds.cern.ch/record/1464102.

[27] R. Brinkmann. *Optimization of a final focus system for large momentum bandwidth*. Tech. rep. 1990.

[28] Fabien Plassard. “Optics optimization of longer L* Beam Delivery System designs for CLIC and tuning of the ATF2 final focus system at ultra-low β* using octupoles”. PhD thesis. 2018, CERN-THESIS-2018-223.

[29] Pantaleo Raimondi and Andrei Seryi. “Novel Final Focus Design for Future Linear Colliders”. In: *Phys. Rev. Lett.* **86** (17 Apr. 2001), pp. 3779–3782. DOI: 10.1103/PhysRevLett.86.3779. URL: https://link.aps.org/doi/10.1103/PhysRevLett.86.3779.

[30] G.R. White, R. Ainsworth, T. Akagi, J. Alabau-Gonzalvo, D. Angal-Kalinin, S. Araki, A. Aryshev, S. Bai, P. Bambade, D.R. Bett, et al. “Experimental validation of a novel compact focusing scheme for future energy-frontier linear lepton colliders”. In: *Physical review letters* **112.3** (2014), p. 034802.

[31] Katsunobu Oide. “Synchrotron-radiation limit on the focusing of electron beams”. In: *Physical review letters* **61.15** (1988), p. 1713.

[32] W. Singer et al. “Production of superconducting 1.3-GHz cavities for the European X-ray Free Electron Laser”. In: *Phys. Rev. Accel. Beams* **19** (9 Sept. 2016), p. 092001. DOI: 10.1103/PhysRevAccelBeams.19.092001. URL: https://link.aps.org/doi/10.1103/PhysRevAccelBeams.19.092001.

[33] P. Bambade, T. Barklow, T. Behnke, M. Berggren, J. Brau, P. Burrows, D. Denisov, A. Faus-Golfe, B. Foster, K. Fujii, et al. “The international linear collider: a global project”. In: *arXiv:1903.01629* (2019).

[34] Hao Zha and Alexej Grudiev. “Design and optimization of Compact Linear Collider main linac accelerating structure”. In: *Phys. Rev. Accel. Beams* **19** (11 Nov. 2016), p. 111003. DOI: 10.1103/PhysRevAccelBeams.19.111003. URL: https://link.aps.org/doi/10.1103/PhysRevAccelBeams.19.111003.

[35] D. Alesini et al. “Commissioning Status of the CTF3 Delay Loop”. In: (July 2006). revised version submitted on 2006-10-03 11:57:13. URL: https://cds.cern.ch/record/971857.

[36] M. J. Boland et al. *Updated baseline for a staged Compact Linear Collider*. CERN Yellow Reports: Monographs. Comments: 57 pages, 27 figures, 12 tables. Geneva: CERN, Aug. 2016. DOI: 10.5170/CERN-2016-004. URL: https://cds.cern.ch/record/2210892.

[37] Alasdair Winter. "Physics Potential of CLIC Operation at 380 GeV". In: (May 2017), pp. 189–192. 5. DOI: oai:cds.cern.ch:2263676. URL: https://cds.cern.ch/record/2263676.

[38] Y. Papaphilippou et al. "Conceptual Design of the CLIC Damping Rings". In: *Conf. Proc.* C1205201 (May 2012), TUPPC086. 3 p. URL: https://cds.cern.ch/record/1464093.

[39] Roberto Corsini. "Final Results From the Clic Test Facility (CTF3)". In: (2017), TUZB1. 6 p. DOI: 10.18429/JACoW-IPAC2017-TUZB1. URL: https://cds.cern.ch/record/2289699.

[40] F. Hinode et al. *ATF accelerator test facility design and study report no. 4*. KEK, Tsukuba, Japan 1995.

[41] K. Kubo, M. Akemoto, S. Anderson, T. Aoki, S. Araki, K. Bane, P. Blum, J. Corlett, K. Dobashi, P. Emma, et al. "Extremely low vertical-emittance beam in the Accelerator Test Facility at KEK". In: *Physical review letters* **88.19** (2002), p. 194801.

[42] Y. Honda, K. Kubo, S. Anderson, S. Araki, K. Bane, A. Brachmann, J. Frisch, M. Fukuda, K. Hasegawa, H. Hayano, et al. "Achievement of Ultralow Emittance Beam in the Accelerator Lest Facility Damping Ring". In: *Physical Review Letters* **92.5** (2004), pp. 548021–548025.

[43] E. Marin et al. "Design and high order optimization of the Accelerator Test Facility lattices". In: *Phys. Rev. ST Accel. Beams* **17** (2 Feb. 2014), p. 021002. DOI: 10.1103/PhysRevSTAB.17.021002. URL: https://link.aps.org/doi/10.1103/PhysRevSTAB.17.021002.

[44] H. H. Braun, A. Wolski, L. Jenner, D. Schulte, G. A. Blair, J. Gronberg, M. Kuriki, A. Reichold, C. Driouichi, et al. *ATF2 Proposal: v. 1*. Tech. rep. 2005.

[45] Andrei Seryi, Rogelio Tomas, Frank Zimmermann, Kiyoshi Kubo, Shigeru Kuroda, Toshiyuki Okugi, Toshiaki Tauchi, Nobuhiro Terunuma, Junji Urakawa, Glen White, et al. "Experimental and theoretical progress of linear collider final focus design and ATF2 facility". In: *Nuclear Instruments and Methods in Physics Research Section A: Accelerators, Spectrometers, Detectors and Associated Equipment* **740** (2014), pp. 2–5.

[46] Barbara Dalena, Javier Barranco, Andrea Latina, Eduardo Marin, Jurgen Pfingstner, Daniel Schulte, Jochem Snuverink, Rogelio Tomás, and Guillermo Zamudio. "Beam delivery system tuning and luminosity monitoring in the Compact Linear Collider". In: *Physical Review Special Topics-Accelerators and Beams* **15.5** (2012), p. 051006.

[47] J. Ögren, A. Latina, R. Tomás, and D. Schulte. "Tuning the Compact Linear Collider 380 GeV final-focus system using realistic beam-beam signals". In: *Physical Review Accelerators and Beams* **23.5** (2020), p. 051002.

[48] R. Yang et al. "Tuning the ultralow β^* optics at the KEK Accelerator Test Facility 2". In: *Phys. Rev. Accel. Beams* **23** (7 July 2020), p. 071003. DOI: 10.1103/PhysRevAccelBeams.23.071003. URL: https://link.aps.org/doi/10.1103/PhysRevAccelBeams.23.071003.

[49] M. Modena. "Update on 2 Octupoles Procurement for ATF2 Final Focus Systems". In: *18th ATF2 Project meeting*. 2015.

[50] D. Schulte. *Multi-bunch calculations in the CLIC main linac*. Tech. rep. 2009.

[51] R. Tomás. "Overview of the Compact Linear Collider". In: *Phys. Rev. ST Accel. Beams* **13** (1 Jan. 2010), p. 014801. DOI: 10.1103/PhysRevSTAB.13.014801.

[52] Ian Hinchliffe and Marco Battaglia. "The next Linear collider". In: *Physics today* **57**.LBNL-55642 (2004).

[53] Andrei Seryi. *Beam Delivery Layout For The Next Linear Collider*. Tech. rep. Stanford Linear Accelerator Center, Menlo Park, CA (US), 2004.

[54] Grahame A. Blair. *Beam Delivery System in ILC*. Tech. rep. 2006.

[55] V. I. Telnov. "The lay-out of the photon collider at the international linear collider". In: *Pramana* **69**.6 (Dec. 2007), pp. 1177–1179. ISSN: 0973-7111. DOI: 10.1007/s12043-007-0250-y. URL: http://dx.doi.org/10.1007/s12043-007-0250-y.

[56] H. Grote and F. Schmidt. "MAD-X-an upgrade from MAD8". In: *Proceedings of the 2003 Particle Accelerator Conference*. Vol. **5**. IEEE. 2003, pp. 3497–3499.

[57] P.J. Bryant. "Insertions". In: *CAS - CERN Accelerator School: 5th General Accelerator Physics Course, CERN Geneva* (1992), pp. 159–190.

[58] Toshinori Abe, Jason M. Abernathy, Halina Abramowicz, Marek Adamus, Bernardo Adeva, IGFAE Santiago de Compostela U., Konstantin Afanaciev, NCPHEP Minsk, Juan Antonio Aguilar-Saavedra, U. Granada, et al. *The international large detector: letter of intent*. Tech. rep. Fermi National Accelerator Lab.(FNAL), Batavia, IL (United States), 2010.

[59] H. Aihara, P. Burrows, and M. Oreglia. "SiD letter of intent". In: *arXiv:0911.0006* (2009).

[60] Frank Simon. "Detector systems at CLIC". In: *Physics Procedia* **37** (2012), pp. 63–71.

[61] R. Tomás and M. Jørgensen. *Optimizing the CLIC Beam Delivery System*. Tech. rep. 2008.

[62] Kurt Artoos, Ofelia Capatina, C. Collette, M. Guinchard, Claude Hauviller, M. Sylte, B. Bolzon, and A. Jérémie. "Ground vibration and coherence length measurements for the CLIC nano-stabilization studies". In: *Particle Accelerator Conference (PAC09)*. 2009, TH5RFP081.

[63] Lau Gatignon. "CLIC MDI Overview". In: *arXiv:1202.6511* (2012).

[64] Brett Parker and Andrei Seryi. "Compensation of the effects of a detector solenoid on the vertical beam orbit in a linear collider". In: *Physical Review Special Topics-Accelerators and Beams* **8.4** (2005), p. 041001.

[65] B. Dalena, D. Schulte, R. Tomás, and D. Angal-Kalinin. "Solenoid and Synchrotron Radiation effects in CLIC". In: *Proceedings of PAC'09, Vancouver, Canada* (2009).

[66] A. Seryi. "Near IR FF design including FD and longer L* issues". In: *CLIC08* (2008).

[67] R. Tomás, J.P. Baud, A.C. Dexter, J.L. Fernandez Hernando, D. Schulte, F. Peltier, A. Jeremie, R.M. Jones, P.K. Ambatu, B. Bolzon, et al. *Summary of the BDS and MDI CLIC08 working group*. Tech. rep. 2008.

[68] Guillermo Zamudio and Rogelio Tomas. *Optimization of the CLIC 500 GeV final focus system and design if a new 3 TeV final focus system with L*= 6.0 m*. Tech. rep. 2010.

[69] Niloufar Alipour Tehrani, Fernando Duarte Ramos, Benoit Cure, Andrea Gaddi, Jean-Jacques Blaising, Dominik Dannheim, Christian Grefe, Felix Sefkow, Lars Rickard Strom, Steven Green, et al. *CLICdet: The post-CDR CLIC detector model*. Tech. rep. 2017.

[70] Yuri Nosochkov and Andrei Seryi. "Compensation of detector solenoid effects on the beam size in a linear collider". In: *Physical Review Special Topics-Accelerators and Beams* **8.2** (2005), p. 021001.

[71] Sha Bai, Alexander Aryshev, Philip Bambade, Doug Mc Cormick, Benoit Bolzon, Jie Gao, Toshiaki Tauchi, and Feng Zhou. "First beam waist measurements in the final focus beam line at the KEK Accelerator Test Facility". In: *Physical Review Special Topics-Accelerators and Beams* **13.9** (2010), p. 092804.

[72] M. Bassetti, C. Biscari, and C. Milardi. "Solenoidal Compensation Scheme for an Interaction Region of an Electron-Positron Collider". In: *DAΦNE Machine Project* (1994), p. 30.

[73] Andrei Seryi, Takashi Maruyama, et al. *IR optimization, DID and anti-DID*. Tech. rep. Stanford Linear Accelerator Center (United States). Funding organisation: US, 2006.

[74] Y. Inntjore Levinsen, Barbara Dalena, Rogelio Tomás, and Daniel Schulte. "Impact of detector solenoid on the Compact Linear Collider luminosity performance". In: *Physical Review Special Topics-Accelerators and Beams* **17.5** (2014), p. 051002.

[75] D. Schulte, T.E. D'Amico, G. Guignard, and N. Leros. *Simulation Package based on PLACET*. Tech. rep. CERN-PS-2001-028-AE, 2001.

[76] Daniel Schulte. *Beam-beam simulations with GUINEA-PIG*. Tech. rep. CERN-PS-99-014-LP, 1999.

[77] Dominik Arominski, Andrea Latina, and Daniel Schulte. "Resistive wall effects in the CLIC Beam Delivery System". In: (June 2019), MOPGW071. 4. DOI: 10.18429/JACoW-IPAC2019-MOPGW071. URL: https://cds.cern.ch/record/2678469.

[78] Rogelio Tomás. *MAPCLASS: a code to optimize high order aberrations*. Tech. rep. CERN-AB-Note-017, 2006.

[79] Rogelio Tomás. "Nonlinear optimization of beam lines". In: *Physical Review Special Topics-Accelerators and Beams* **9.8** (2006), p. 081001.

[80] D. Martinez, A. Rosam, R. Tomás, and R. De Maria. *MAPCLASS2: a code to aid the optimisation of lattice design*. Tech. rep.

[81] E. Forest, F. Schmidt, and E. McIntosh. "Introduction to the polymorphic tracking code". In: *KEK report* **3** (2002), p. 2002.

[82] B. Cure. *Private Communications*.

[83] B. Dalena, D. Schulte, and R. Tomas. *Impact of the Experiment Solenoid on the CLIC Luminosity*. Tech. rep. CERN-ATS-2010-082, 2010.

[84] T. Okugi, S. Araki, P. Bambade, K. Kubo, S. Kurado, M. Masuzawa, E. Marin, T. Naito, T. Tauchi, N. Terunuma, et al. "Linear and second order optics corrections for the KEK Accelerator Test Facility final focus beam line". In: *Physical Review Special Topics-Accelerators and Beams* **17.2** (2014), p. 023501.

[85] M. Patecki, D. Bett, E. Marin, F. Plassard, R. Tomás, K. Kubo, S. Kuroda, T. Naito, T. Okugi, T. Tauchi, et al. "Probing half β_y^* optics in the Accelerator Test Facility 2". In: *Physical Review Accelerators and Beams* **19.10** (2016), p. 101001.

[86] Marcin Patecki. "Optimisation analysis and improvement of the effective beam sizes in Accelerator Test Facility 2". PhD thesis. Warsaw University of Technology (PL), 2016.

[87] J. Alabau-Gonzalvo, C. Blanch Gutierrez, A. Faus-Golfe, JJ. Garcia-Garrigos, J. Resta-Lopez, J. Cruz, D. McCormick, G. White, and M. Woodley. "The ATF2 Multi-OTR System: Studies and Design Improvements". In: *International Beam Instrumentation Conference*. 2012.

[88] Y.I. Kim, R. Ainsworth, A. Aryshev, S.T. Boogert, G. Boorman, J. Frisch, A. Heo, Y. Honda, W.H. Hwang, J.Y. Huang, et al. "Cavity beam position monitor system for the Accelerator Test Facility 2". In: *Physical Review Special Topics-Accelerators and Beams* **15**.**4** (2012), p. 042801.

[89] Marcin Patecki and Rogelio Tomás. "Effects of quadrupole fringe fields in final focus systems for linear colliders". In: *Physical Review Special Topics-Accelerators and Beams* **17**.**10** (2014), p. 101002.

[90] T. Shintake, D. Walz, A. Hayakawa, M. Ohashi, K. Yasuda, D. Burke, S. Wagner, Y. Ozaki, and H. Hayano. "Design of laser Compton spot size monitor". In: *Int. J. Mod. Phys. Proc. Suppl.* **1**.KEK-PREPRINT-92-65 (1992), pp. 215–218.

[91] Yan Jacqueline. "Precise Measurement of Nanometer Scale Electron Beam Sizes Using Laser Interference by Shintake Monitor". PhD thesis. University of Tokyo, 2015.

[92] J. Yan, M. Oroku, Y. Yamaguchi, T. Yamanaka, Y. Kamiya, T. Suehara, S. Komamiya, T. Okugi, N. Terunuma, T. Tauchi, et al. "Shintake Monitor Nanometer Beam Size Measurement and Beam Tuning". In: *Physics Procedia* **37** (2012), pp. 1989–1996.

[93] Yohei Yamaguchi, Sachio Komamiya, Masahiro Orouku, Taikan Suehara, Takashi Yamanaka, Toshiaki Tauchi, Nobuhiro Terunuma, and Junji Urakawa. "Evaluation of expected performance of shintake beam size monitor for atf2". In: *laser* **2**.**2** (2010), p. 1.

[94] Vera Cilento. "Optimization of the Beam Size at the Interaction Point of the Accelerator Test Facility 2". Presented 10 Oct 2018. Oct. 2018. URL: https://cds.cern.ch/record/2643785.

[95] G. White, A. Seryi, M. Woodley, E. Marin, Y. Kamiya, S. Bai, B. Bolzon, K. Kubo, S. Kuroda, T. Okugi, et al. "Operational Experiences Tuning the ATF2 Final Focus Optics Towards Obtaining a 37 nanometer Electron Beam IP Spot Size". In: *Proceedings of IPAC* **10** (2010), pp. 2383–2385.

[96] R. Yang, A. Pastushenko, V. Cilento, K. Kubo, T. Naito, T. Okugi, N. Terunuma, and R. Tomás. "Momentum bandwidth of the KEK Accelerator Test Facility 2". In: *Phys. Rev. Accel. Beams* **24** (5 May 2021), p. 051001. DOI: 10.1103/PhysRevAccelBeams.24.051001. URL: https://link.aps.org/doi/10.1103/PhysRevAccelBeams.24.051001.

[97] V.Cilento. *ATF2 Control Room*.

[98] URL: https://clicr.web.cern.ch/CLICr/MainBeam/.

[99] Vera Cilento, Rogelio Tomás, Benoit Cure, Angeles Faus-Golfe, Barbara Dalena, and Yngve Levinsen. "Dual beam delivery system serving two interaction regions for the Compact Linear Collider". In: *Phys. Rev. Accel. Beams* **24** (7 July 2021), p. 071001. DOI: 10.1103/PhysRevAccelBeams.24.071001. URL: https://link.aps.org/doi/10.1103/PhysRevAccelBeams.24.071001.

[100] V. Cilento, A. Faus-Golfe, and R. Tomás García. "A CLIC Dual Beam Delivery System for Two Interaction Regions". In: *Proc. IPAC'21* (Campinas, SP, Brazil). International Particle Accelerator Conference 12. https://doi.org/10.18429/JACoW-IPAC2021-TUPAB013. JACoW Publishing, Geneva, Switzerland, Aug. 2021, pp. 1364–1367. ISBN: 978-3-95450-214-1. DOI: 10.18429/JACoW-IPAC2021-TUPAB013. URL: https://jacow.org/ipac2021/papers/tupab013.pdf.

[101] Vera Cilento, Andrii Pastushenko, Renjun Yang, Rogelio Tomas Garcia, Angeles Faus-Golfe, Nobuhiro Terunuma, Toshiyuki Okugi, and Kiyoshi Kubo. "ATF2 Ultra-low β_y^* study report for March 2019 run". In: (Jan. 2020). URL: https://cds.cern.ch/record/2706505.

[102] Alexander Aryshev et al. *ATF report 2020*. Tech. rep. Geneva: CERN, Oct. 2020. URL: https://cds.cern.ch/record/2742899.